BALLISTIC PENETRATION OF HARDENED STEEL PLATES

A THESIS SUBMITTED TO
THE GRADUATE SCHOOL OF NATURAL AND APPLIED SCIENCES
OF
MIDDLE EAST TECHNICAL UNIVERSITY

BY

TANSEL DENİZ

IN PARTIAL FULFILLMENT OF THE REQUIREMENTS
FOR
THE DEGREE OF MASTER OF SCIENCE
IN
MECHANICAL ENGINEERING

AUGUST 2010

Approval of the thesis:

BALLISTIC PENETRATION OF HARDENED STEEL PLATES

submitted by **TANSEL DENİZ** in partial fulfillment of the requirements for the degree of **Master of Science in Mechanical Engineering Department, Middle East Technical University** by,

Prof. Dr. Canan Özgen
Dean, Graduate School of **Natural and Applied Sciences** _____

Prof. Dr. Süha Oral
Head of Department, **Mechanical Engineering** _____

Prof. Dr. R. Orhan Yıldırım
Supervisor, **Mechanical Engineering Department** _____

Examining Committee Members:

Prof. Dr. Metin Akkök
Mechanical Engineering Dept., METU _____

Prof. Dr. R. Orhan Yıldırım
Mechanical Engineering Dept., METU _____

Prof. Dr. Can Çoğun
Mechanical Engineering Dept., METU _____

Asst. Prof. Dr. Yiğit Yazıcıoğlu
Mechanical Engineering Dept., METU _____

Dr. Rıdvan Toroslu
Aselsan Elektronik Sanayi ve Ticaret A.Ş. _____

Date: _____

I hereby declare that all information in this document has been obtained and presented in accordance with academic rules and ethical conduct. I also declare that, as required by these rules and conduct, I have fully cited and referenced all material and results that are not original to this work.

Name, Last Name: TANSEL DENİZ

Signature :

ABSTRACT

BALLISTIC PENETRATION OF HARDENED STEEL PLATES

Deniz, Tansel
M.Sc., Department of Mechanical Engineering
Supervisor : Prof. Dr. R. Orhan Yıldırım

August 2010, 113 pages

Ballistic testing is a vital part of the armor design. However, it is impossible to test every condition and it is necessary to limit the number of tests to cut huge costs. With the introduction of hydrocodes and high performance computers; there is an increasing interest on simulation studies to cutoff these aforementioned costs. This study deals with the numerical modeling of ballistic impact phenomena, regarding the ballistic penetration of hardened steel plates by 7.62 mm AP (Armor Piercing) projectile. Penetration processes of AP projectiles are reviewed. Then, a survey on analytical models is given. After the introduction of fundamentals of numerical analysis, an intensive numerical study is conducted in 2D and 3D. Johnson Cook strength models for the four different heat treatments of AISI 4340 steel were constructed based on the dynamic material data taken from the literature. It was found that 2D numerical simulations gave plausible results in terms of residual projectile velocities, considering the literature review. Then, 3D numerical simulations were performed based on the material properties that were selected in 2D studies. Good agreement was obtained between the numerical and test results in terms of residual projectile velocities and ballistic limit thicknesses. It was seen that the ballistic protection efficiency of the armor plates increases with the increasing hardness, in the examined range.

This study is a part of Tübitak project 106M211 of MAG.

Keywords: ballistic penetration, simulation, 7.62 mm AP, hardened steel, AUTODYN

ÖZ

SERTLEŞTİRİLMİŞ ÇELİK PLAKALARIN BALİSTİK PENETRASYONU

Deniz, Tansel
Yüksek Lisans, Makina Mühendisliği Bölümü
Tez Yöneticisi : Prof. Dr. R. Orhan Yıldırım

Ağustos 2010, 113 sayfa

Balistik testler zırh tasarımının önemli bir parçasıdır. Fakat tasarım esnasında her türlü konfigürasyonu test etmek zaman ve maliyet açısından imkansız olduğu için analitik ve sayısal yaklaşımlar kullanarak öngörülerde bulunmak ve test sayısını en aza indirgemek gerekmektedir. Bu çalışmada, sertleştirilmiş çelik plakaların 7.62 mm zırh delici mermilerle delinmesi incelenmiştir. Zırh delici mermilerin delme prosesleri gözden geçirilmiştir. Daha sonra ise analitik modeller üzerine bir literatür taraması sunulmuştur. Sayısal benzetim yazılımının temelleri tanıtıldıktan sonra 2 ve 3 boyutlu olmak üzere geniş bir benzetim çalışması yapılmıştır. Literatürden alınan dinamik malzeme verileri ışığında AISI 4340 çeliği için Johnson-Cook dayanım modelleri oluşturulmuştur. Bu modeller ile yapılan sayısal benzetimler neticesinde 2 boyutlu sayısal benzetimlerin mermi artık hızları açısından gerçekçi sonuçlar verdiği görülmüştür. Başarılı olan malzeme modelleri 3 boyutlu sayısal benzetimlerde de koşturulmuştur. Yapılan değerlendirmede 3 boyutlu benzetim sonuçlarının test sonuçları ile mermi artık hızları ve balistik limit kalınlıkları açısından uyumlu oldukları görülmüştür. Yapılan çalışmalar neticesinde incelenen sertlik aralığında, artan plaka sertliğinin balistik koruma performansını arttırdığı görülmüştür.

Bu çalışma 106M211 nolu Tübitak MAG projesinin bir parçasıdır.

Anahtar Kelimeler: balistik delme, sayısal benzetim, 7.62 mm AP, sertleştirilmiş çelik, AUTODYN

to my family..

ACKNOWLEDGMENTS

The author wishes to express his deepest gratitude to his supervisor Prof. Dr. R. Orhan Yıldırım for his guidance, advice, criticism, encouragements and insight throughout the research.

The technical assistance and the fruitful discussions with Namık Kılıç, Atıl Erdik, Teyfik Demir and Gökhan Öztürk are also gratefully acknowledged. He would also like to thank Tuğba Kaya for her encouragements and support during the thesis work.

This thesis was a part of MAG funded project 106M211. The author would also like to thank TÜBİTAK BİDEB for their financial support during the graduate study. Also the cooperation of Silahsan A.Ş. was highly appreciated.

Finally, the author would like to express his best feelings to his family for their endless support during his whole life. This study would not exist without their guidance and great love.

TABLE OF CONTENTS

LIST OF TABLES

TABLES

LIST OF FIGURES

FIGURES

LIST OF ABBREVIATIONS

AFV Armored Fighting Vehicle

AP Armor Piercing

APDS Armor Piercing Discarding Sabot

APFSDS Armor Piercing Fin Stabilized Discarding Sabot

APM2 Armor Piercing M2 Round

BCC Body Centered Cubic

DHA Dual Hardness Armor

DOP Depth of Penetration

EFP Explosively Formed Projectile

HCP Hexagonal Close Packed

HEAT High Explosive Anti Tank

HHA High Hard Armor

HRC Rockwell C Hardness

J-C Johnson-Cook

KE Kinetic Energy

MTS Mechanical Threshold Stress Model

OFHC Oxygen-Free High Conductivity

RHA Rolled Homogenous Armor

SFF Self Forging Fragment

SPH Smoothed Particle Hydrodynamics

CHAPTER 1

INTRODUCTION

From the beginning of the human history, the battle of weapon and armor had continued. As new weapons are developed, corresponding armors are also developed in response. Today, development of lightweight armors against small caliber projectiles is getting important as mobility is considered. In this context, a study regarding the effect of heat treatment of steel plates on ballistic protection efficiency is performed. The interaction between the small caliber projectile and steel armor plate falls into the domain of ballistics science.

1.1 Terminal Ballistics

Ballistics is the science of mechanics that mainly deals with the acceleration of the projectile in the gun barrel, behavior of projectile at the muzzle and during the flight and its effects on the target. It is mainly separated into three branches which are interior, exterior and terminal ballistics. Current study is an interest of terminal ballistics.

The branch that studies the interaction between a projectile and a target is called *terminal ballistics* [1]. The parameters regarding the study of terminal ballistics includes strike velocity, strike angle and the type of the projectile and target. The following sections (1.2,1.3,1.4) introduce the projectile types, target configurations and target materials respectively.

1.2 Threats for Armors

Type of projectiles are generally separated into two main groups; namely kinetic energy projectiles and chemical energy weapons.

1.2.1 Kinetic Energy Threats

According to Hazell [2] kinetic energy rounds can be studied in two main groups as small-arms ammunition (<20 mm) and higher-caliber KE (Kinetic Energy) rounds including medium caliber (>20 mm). Following sections introduce these type of threats.

1.2.1.1 Small Caliber Armor Piercing Projectiles

In general; small caliber ammunition consists of a penetrating mass surrounded by a gilding jacket that acts as a layer which protects the penetrator core from the rifling of the barrel. The penetrator is manufactured in various kinds of shapes and sizes. For aerodynamic stability; simply most of the projectiles possess an ogival nose. A schematic view of 7.62 mm ball and AP projectile are given in Figure 1.1 [3]

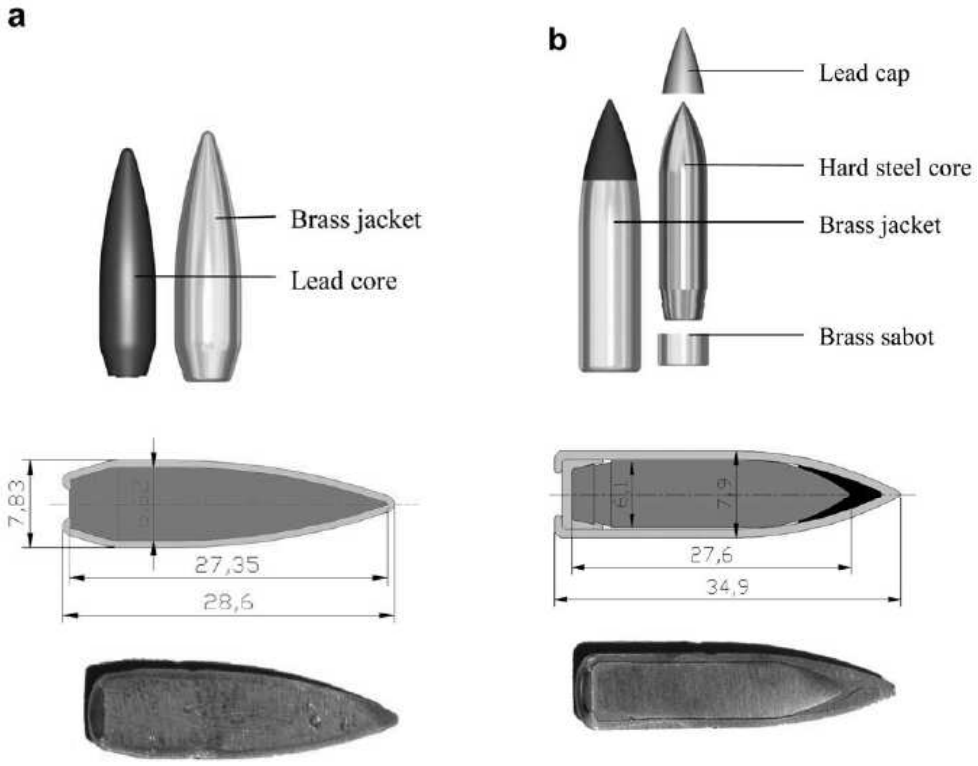

Figure 1.1: Schematic drawing, geometry and cross-section picture of (a) Ball projectile and (b) APM2 projectile [3]

These ammunition can be grouped into two such as the ones used for stopping a target (not necessarily killing) and the ones for penetrating a target [2]. The first group consists of rounds with high deforming core such as lead or soft steel, which are called *ball rounds*. The projec-

tiles of the second group are called *armor piercing rounds*, and consist of a fast non-deforming core such as tungsten carbide or hard steel.

AP projectiles typically have a length to diameter (L/D) ratio in the range 3:1 to 5:1 with muzzle velocities which can reach to 1000 m/s. These kind of projectiles tend to produce a total KE on the order of 10^3 – 10^4 J [4].

1.2.1.2 Long Rod Penetrators

Generally, there are two types of higher-caliber KE ammunition which are classified as the APDS (Armor Piercing Discarding Sabot) round and the APFSDS (Armor Piercing Fin Stabilized) round [2].

The APDS round usually consists of a dense core (mostly tungsten carbide) with L/D in the range 6 to 7. These kind of ammunition have been largely superseded by the APFSDS round. The APFSDS round consists of a steel, tungsten heavy alloy or depleted uranium alloy core. Its L/D ranges between 15 and 25 and muzzle velocities vary between 1400 and 1900 m/s [2]. These threats yield 10^6 J of KE during impact. A view of APFSDS round shortly after muzzle exit is given in Figure 1.2

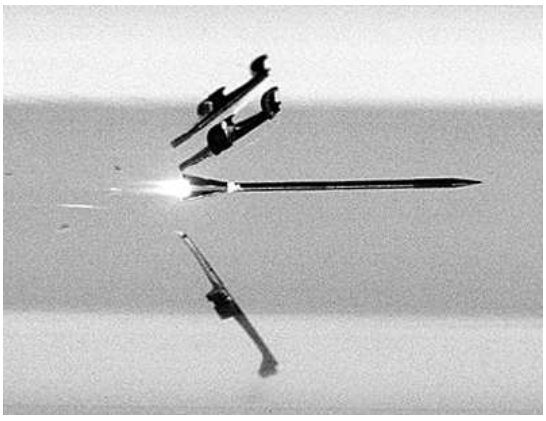

Figure 1.2: APFSDS at point of separation of sabot

1.2.2 Chemical Energy Threats

Unlike KE projectiles, chemical energy threats use the energy of an explosive to form a penetrator. These munitions can be classified into two groups as shaped charge devices and explosively formed projectiles.

1.2.2.1 Shaped Charges

Shaped charge warheads belong to HEAT (High Explosive Anti-Tank) threats. Upon impact, a very high velocity jet is formed by the collapse of the liner material (usually copper) which is a result of a high-compressive detonation wave from an explosive charge. The resulting jet possesses a tip velocity in the range $5-11$ km/s and a tail velocity typically around 2 km/s [5]. Flash X-ray image of a shaped charge jet is given in Figure 1.3

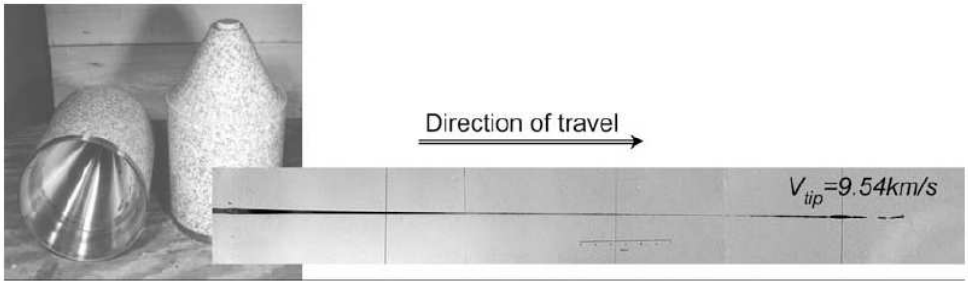

Figure 1.3: Copper liner and explosive on the left, flash X-ray of a jet in right [5]

1.2.2.2 Explosively Formed Projectiles

In the case of EFP (explosively formed projectile) or SFF (self forging fragment), the projectile is formed by the dynamic deformation of a metallic dish due to the detonation of an explosive charge located behind it. The mechanism of dish formation is very similar to that of a shaped charge warhead, however the fundamental difference is that, instead of a conical liner being deformed into a jet, a relatively shallow dish is formed into a slug or projectile. The dish is often made of a relatively soft material to ensure that it deforms into an appropriate projectile like shape. Relatively dense materials such as copper, iron, steel and more recently tantalum are used to ensure effective penetrative performance, especially in the lower part of the hydrodynamic regime ($2-3$ km/s) [2].

1.3 Armor Configurations

Armor configurations can be classified in three main groups according to the way they treat the threat. These groups are namely passive, reactive and active armors.

1.3.1 Passive Armors

Passive armors are designed to absorb the kinetic energy of a kinetic energy projectile or a shaped charge jet. Special combinations of high strength materials and geometrical designs are used to achieve desired mechanisms against aforementioned threats. From the experience of the author, known types of passive armors are listed below.

Sloped Armor These armors are placed obliquely rather than having a vertical surface. The thickness of the armor can be increased by this way. The second purpose is to ricochet or deflect incoming KE threats.

Spaced Armor Its commonly used to defeat shaped charge jets by increasing the distance the jet has to travel to penetrate the armor configuration. Moreover the internal layers can be designed to tumble and deflect incoming KE threats.

Slat Armor It works by holding off the shaped charge device from the skin of the vehicle, and increase the way the jet has to travel so that stand-off effect can occur.

Composite Armor These armors make use of special combinations of steels, ceramics and other materials to absorb and diffuse the damage caused by the threat .

1.3.2 Reactive Armors

Reactive armors make use of elements which are sandwiched between two metal plates. They react upon the impact of a threat and use special mechanisms to defeat the threat. These armors can be classified as follows:

Explosive Reactive Armor It consists of a sandwich with a front and a rear plate of identical or different thickness and of identical or different materials, with a layer of high explosive between generally arranged at an angle to the attack direction [6]. When a

projectile with enough kinetic energy hits, reactive element will be initiated and plates will be accelerated outward. An X-ray view of shaped charge jet defeat by explosive reactive armor is given in Figure 1.4 [7].

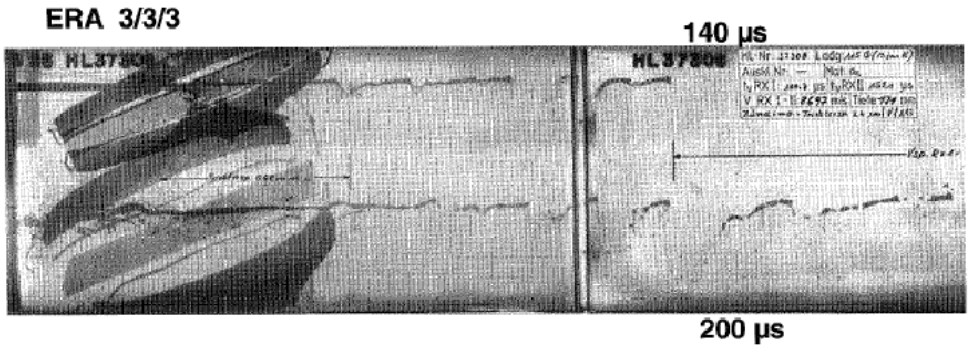

Figure 1.4: Flash X-ray image of explosive reactive armor - shaped charge jet interaction [7]

Non Explosive Reactive Armor It is very similar to explosive reactive armor but it includes an energetic material instead of a high explosive. This energetic material reacts in a lower order then detonation, therefore smaller pressures are generated.

Non Energetic Reactive Armor It uses non-energetic materials such as elastomers instead of energetic materials. These materials absorbs the impact energy and cause the bulging of steel plates.

Electromagnetic Reactive Armor It passes an electric current through the incoming projectile to disrupt and destroy it.

1.3.3 Active Armors

Active armors make use of sensors to detect incoming threats and are designed to respond to intercept, disrupt or deflect these threats. Held [8] classifies different active defense concepts according intercept ranges as:

a) Close range <2 m
b) Medium range 2 to 10 m
c) Long range >10 m

The working principles of these three classes are introduced below [8]

a) Sensors fire a small number of shaped charges to initiate the high explosive content of

an attacking shaped charge warhead. Such an initiation prevents good jet formation. Sensors trigger impactors to destroy or disrupt incoming penetrator such that its broken pieces will hit a larger area on the armor with having less penetrative capability.

b) Sensors discriminate the direction, velocity and distance of a threat and fire a suitable fragmenting charge from an array. The fragments hit the incoming projectile and destroy it.

c) Sensors launch a highly maneuverable mini missile with active or semi-active homing head.

1.4 Armor Materials

Armor materials can be classified into three main groups, namely metallic, ceramic and composite materials.

1.4.1 Metallic Armors

Metals are still the most widely used materials in armor design. The main advantage of these materials is that, they are capable of carrying structural and fatigue loads while offering efficient protection. They are less expensive compared to the other materials.

The most commonly used metallic material in armored fighting vehicles is steel. The main properties such as toughness, hardness, good fatigue strength, ease of fabrication and joining and relative low cost make it a popular material for armored vehicle hulls [2]. Steel armor can be studied in four main groups which are *Rolled Homogeneous Armor (RHA), High Hardness Armor (HHA), Variable Hardness Steels* and *Perforated Armor*.

Rolled homogeneous armor (RHA) is usually used in depth of penetration testing [2] as a benchmark material. Therefore it is used to describe and compare the performance of different armor systems or materials. The chemical composition [2] and classification of RHA according to UK Ministry of Defense Standard for Armor Plate [9] are given in Table 1.1 and Table 1.2.

Table 1.1: Composition of RHA [9]

C	Mn	Ni	Cr	Mo	S	P
0.18-0.32	0.60-1.50	0.05-0.95	0.00-0.90	0.30-0.60	0.015 (max)	0.015 (max)

Table 1.2: Classification of RHA [9]

Classification	Description	Hardness (BHN)	UTS (MPa)	Elongation (%) Min
Class 1	Readily weldable steel subjected to structural loads.	262-311	895-1,050	15
Class 2	Readily weldable steel to protect against AP ammunition.	255-341	895-955	14-16
Class 3	Readily weldable higher hardness steel manufactured in thin sections.	470-540	1,450-1,850	8
Class 3A	Readily weldable higher hardness steel manufactured in thin sections.	420-480	1,200-1,600	9
Class 4	Higher carbon and alloy content higher hardness armor for thick sections.	475-605	1,450-2,000	7
Class 5	High alloy content armor with very high hardness used for special applications such as perforated armor.	560-655	1,800-2,400	6

High hardness armor (HHA) on the other hand, is the name given to a class of homogeneous steel armor which have hardness values exceeding 430 BHN [2].

Variable hardness steel plates introduces some advantages with varying through-thickness properties. By surface hardening one side of a thick low-carbon steel plate, it is possible to incorporate both hard disruptive and tough absorbing properties in a single material [2]. The

main advantage is that, the more ductile backing layer is able to arrest crack propagation in the armor plate while the hard front layer is able deform or fracture the threat. The effectiveness of dual-hardness armor (DHA) is given by a comparison in Table 1.3 [10]. It can be seen that DHA is more efficient compared to HHA in defeating steel cored 7.62 AP bullet.

Table 1.3: Density, thickness and areal density values required to protect against 7.62 mm AP bullets at normal incidence [10]

Armour Steel	Density (kg/m^3)	Thickness [1] (mm)	Areal Density (kg/m^2)
RHA (380 BHN)	7830	14.6	114
HHA (550 BHN)	7850	12.5	98
DHA (600-440 BHN)	7850	8.1	64

In perforated armor, holes are introduced into the steel plates. These holes in high hardness steel plate has been shown to be an effective way of disrupting and fragmenting incoming projectiles. This mechanism can be regarded as *edge effect*. Chocron et al [11] has studied the impact of the 7.62 mm APM2 projectile against the edge of a metallic target and a photograph of a fractured core due to aforementioned edge effect is given in Figure 1.5.

Figure 1.5: Photograph of fractured core due to edge effect [11]

Aluminum alloys also provide a versatile choice for an armor design engineer. The main advantage is that, it has a relatively low density while the tensile strengths range from 60 – 600 MPa. It can be deduced that equal mass of aluminum armor will have a larger volume compared to steel, which leads to improvement in rigidity. Material properties of some commonly used aluminum alloys are given in Table 1.4 [2].

Table 1.4: Material properties of some aluminum alloys currently used in AFVs [2]

Alloy	Proof Strength (MPa)	UTS (MPa)	Elongation (%)	Hardness (HV)
Type 5083	(0.1 %) 278	386	6	~100
Type 7017	(0.2 %) 440	490	8	~160
Type 7039	(0.2 %) 420	475	10	~150

However, there are some disadvantages associated with aluminum alloys. The harder alloys that are suitable as armor are susceptible to stress corrosion cracking [2]. This type of failure occurs when the aluminum alloy is attacked by a corrodant while it is subjected to tensile stress. The magnitudes of stresses required to start a failure is lower than that of yield strength and the residual stresses induced during machining, assembly or welding can lead to failure.

These alloys also possess a lower spall strength than steel so that they are prone to scabbing. This makes it necessary to employ a spall liner behind the armor.

The ballistic grade form (Ti-6Al-4V) of titanium also provides a good alternative to steel. It possesses a relatively low density (4.45 g/cm^3) while it maintains high strength and hardness (UTS 900 – 1300 MPa, BHN 300 – 350). However, high cost related with titanium alloys is a prominent shortcoming.

1.4.2 Ceramic Armors

It can be anticipated that the resistance of a given material to penetration mainly depends on its compressive strength [12]. Ceramic materials, which possess high compressive strength and hardness values are good candidate materials as for the armor designer because of their relatively low densities [2]. High strength ceramics such as alumina, boron carbide and silicon carbide exhibit compressive strengths that are an order of magnitude higher than those of metals. Then, it seems plausible to make an assumption that ceramic faced targets will be efficient for armored protection [12].

The costs of ceramic tiles are taken into consideration besides its performance. A comparison of some ceramic materials with prices are given in Table 1.5 [13].

Table 1.5: Relative cost of ceramic materials for armor applications [13]

Ceramic	Bulk Density (kg/m^3)	Hardness (HV)	K_{IC}[a] ($MPa.m^{\frac{1}{2}}$)	Relative Cost
98(%) Al_2O_3	3,800	1,600	4.5	1.0
RB[b] SiC	3,100	1,200/2,200	~4.5	2.5
Sintered SiC	3,150	2,700	3.2	4.5
HP[c] SiC	3,220	2,200	5.0	9.0
HP B_4C	2,520	3,200	2.8	16.0

[a] Fracture Toughness
[b] Reaction Bonded
[c] Hot Pressed

1.4.3 Polymeric Armors

Polymeric composite materials possess high specific strength and specific stiffness and they are able to absorb significant part of kinetic energy induced by projectile impact. They also have relatively lower densities.

These materials consist of laminates of matrix bonded reinforcing fibers. The function of the matrix is to provide a medium for the diffusion of load to the stronger and stiffer fibers. Typical fiber materials are S-glass, E-glass, aramid, carbon and boron. Some properties of these materials are presented in Table 1.6 [14].

Table 1.6: Properties of some fiber materials [14]

Fiber	Bulk Density (kg/m^3)	Tensile Strength (MPa)	Young's Modulus (GPa)	Failure Strain (%)
Aramid (low modulus)	1,440	2,900	60	3.6
Polyethylene (high modulus)	970	3,200	99	3.7
E-glass	2,600	3,500	72	4.8
S-glass	2,500	4,600	86	5.2
Carbon (high strength)	1,780	3,400	240	1.4

1.5 Aim of the Thesis

The process of armor design necessitates extensive test trials which possess the significant cost of the study. The aim of these tests are sometimes to isolate some material or geometric effects. However, it is, in reality, very hard to conduct experiments to optimize every design parameter.

Hydrocodes (hydrocode is a computational analysis tool for modelling large deformations and fluid flow), with the introduction of high performance computers, became as a candidate of a very versatile tool for the armor design engineer. It is very obvious that, when the physics regarding the high velocity impact is well understood together with the material behavior at these regimes, it is possible to conduct numerical simulations that matches the reality to some extent. Of course, procedures regarding the numerical modeling issues should be well understood too.

The aim of this thesis is to represent numerical modeling issues related to impact of 7.62 mm AP projectile to hardened steels. The 7.62 mm AP projectile consists of a hard steel (R_C = 60) ogive-nosed core, followed by a lead plug and is surrounded by a brass jacket. The ogive-nosed projectile has a maximum diameter of 7.62 mm and is 32.95 mm long. It weighs 9.75 grams. The impact velocity was measured as 782 m/s. Some properties of the projectile are given in Table 1.7 [15]. The target material was chosen as AISI 4340 steel. The target materials were heat treated to four different hardness. The main purpose was to establish a relation between the ballistic performance of the steels with respect to their hardness values.

Table 1.7: Some properties of the 7.62 mm AP ammunition [15]

Length of the cartridge	71.12±0.76 mm
Weight of the cartridge	25.47±1.75 g
Casing material	7.62x51 mm Brass (CuZn30)
Core material	DIN 100Cr6 (61 – 62 HRC)
Projectile weight	9.75±0.7 g
Length of the projectile	32.95 mm
Nose type	Conical (half cone angle, $\alpha = 17^o$)

ANSYS Autodyn® software was used for the numerical simulation studies. The modeling alternatives provided by the hydrocode were experienced for the impact studies. The well

known Johnson-Cook strength model was chosen to represent the behavior of the core of the projectile and the heat treated steels. Prediction capabilities of several modeling alternatives and the effect of material model parameters were emphasized. The lessons gained from the review of penetration mechanics were taken into account to interpret numerical analysis results.

Finally, numerical simulation results were compared with the experimental and analytical results. A detailed discussion was made about the advantages and shortcomings of the numerical simulation methodology.

CHAPTER 2

LITERATURE SURVEY ON BALLISTIC PENETRATION OF STEEL PLATES

This part of the thesis contains work on literature survey about the penetration phenomena. First, dynamic mechanisms which yield penetration and perforation of metallic targets by armor piercing projectiles were reviewed. This study lead to a better understanding of the subject, and was necessary for the validation of numerical simulations. Then, previous work on experimental and numerical studies were reviewed.

2.1 Impact Regimes

Dynamic events fall into the regions of interest for many disciplines. Although sources of the impulsive loading may differ, response of the structures to this kind of loading is similar. Material behavior is characterized by the physical properties of materials and the duration of the loading which termed by strain rate. Dynamic events such as crash and impact are characterized by transient response in terms of stress and strain states. The duration of the event plays a significant role in this processes. As the duration of the event gets smaller (ie. increasing strain rate), response of the material diverge from the quasi-static behavior. Also the inertial forces become significant. These regimes are summarized in Figure 2.1 [16].

Typical duration of impact is in the order of 0.1 seconds for car crash events whereas milliseconds for ballistic impacts and microseconds for shaped charge jet impacts. With the increasing impact velocity the response of the structure becomes strongly strain rate dependent. With the higher strain rates, the propagation of shock waves comes into play. After this point, liquid-like (hydrodynamic) behavior is seen in solid.

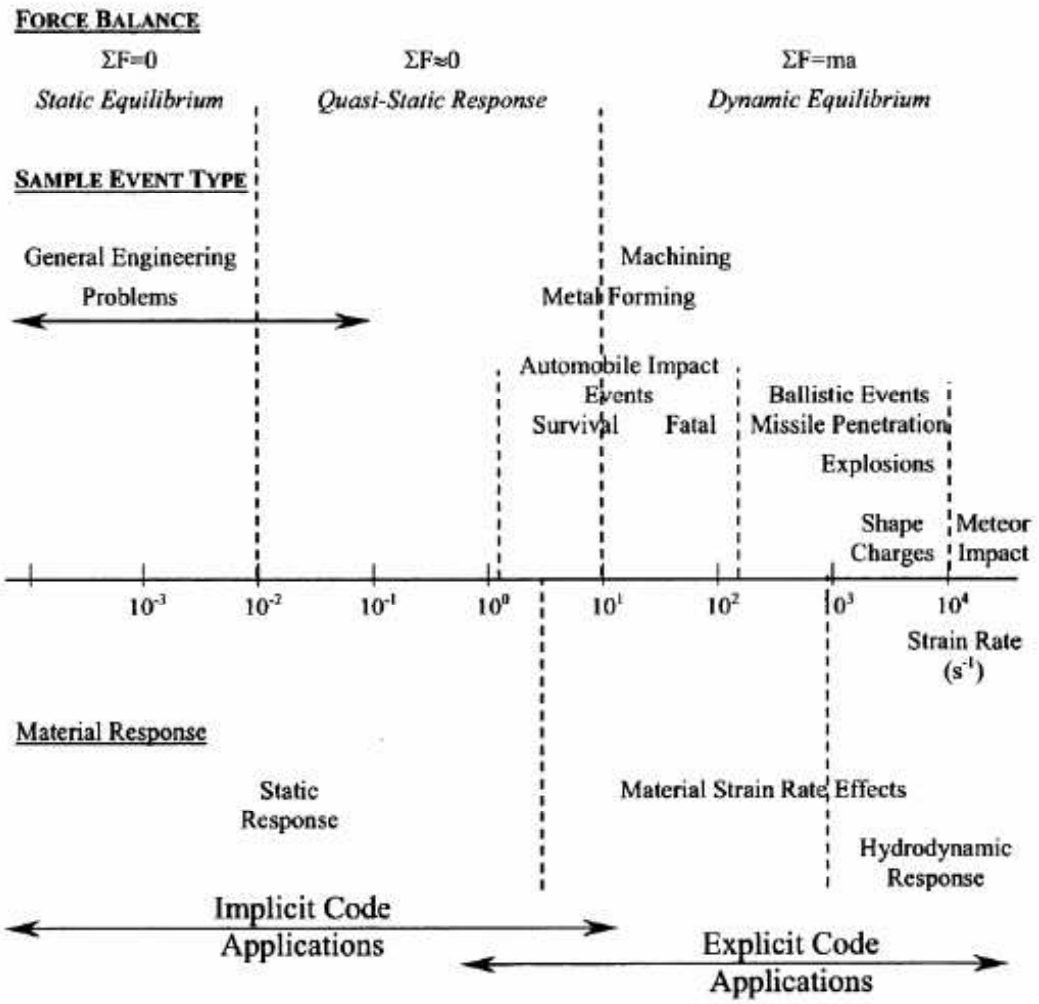

Figure 2.1: Change of the behavior of materials with increasing strain rate and related treatment method [16]

Dynamic material behavior is different from that of quasi-static response. With the decreased duration of event, the material does not have enough time to deform. This results in both higher deformation stresses and local deformations as shown in Figure 2.2 [17] and Figure 2.3 [18].

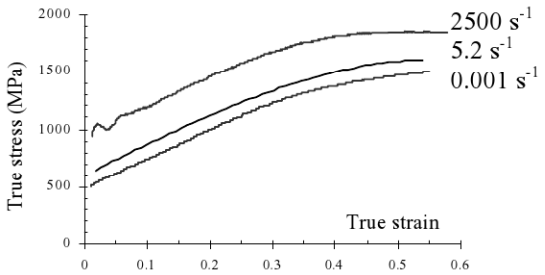

Figure 2.2: Stress-strain curves of Uranus B66 at room temperature for different strain rates [17]

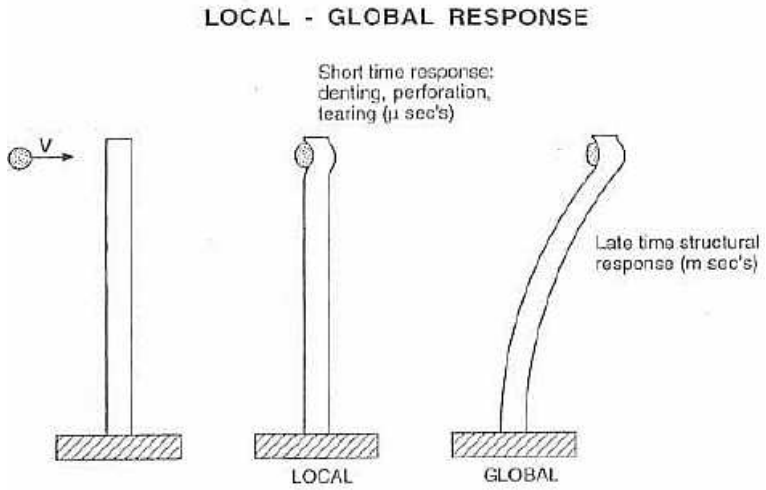

Figure 2.3: Global to local transition of response of a bar impacted by a high speed projectile [18]

The kinetic energy density delivered by the projectile is significant for the determination of target response to an impact. This is defined as the kinetic energy of the projectile divided by its cross-sectional area [19]. When the kinetic energy density at the impact site is low, the shear stress generated in the target may be of the same order of magnitude as the shear strength of the target. Penetration process is governed by the conventional strength materials such as strength, stiffness, hardness and toughness. This is known as the *sub-hydrodynamic* regime of penetration. The kinetic energy density increases for longer, smaller cross-section and higher

density projectiles. The shear stresses generated on impact may be many orders of magnitude greater than the shear strength of both the target and the penetrator. This time the impact process can be characterized as a fluid-fluid interaction where the strengths of the materials are negligible. This is known as the *hydrodynamic* regime of penetration. Below 1000 m/s all impacts are sub-hydrodynamic whereas above 3000 m/s all are hydrodynamic [16]. Thus the transition zone is quite wide. In this zone, although the process is governed by fluid flow, strength still proves to be an important parameter. Therefore, small-arms and AP bullet impacts with impact velocities below 1000 m/s are at sub-hydrodynamic regime, long rod penetrators, with impact velocities in the region of 1600 m/s are clearly in transition zone whereas for shaped-charge impact, with jet tip velocities in excess of 8000 m/s is purely in hydrodynamic zone.

2.2 Review on Penetration Mechanics

The study of plate penetration and perforation covers a diverse range of problems and applications. The interest of current study is to understand and emphasize the effects of impact of armor piercing projectiles into metallic plates.

Penetration is a general term that refers to the impact case in which the projectile enters the target. *Perforation* refers to a penetration case in which the projectile passes completely through the target. *Embedment* refers to a penetration case in which the projectile does not pass through the target, and remains attached to the target after the impact event is over [16].

First, it is necessary to identify different ballistic impact concepts. The ballistic limit velocity, V_{BL}, is the velocity below which the projectile will fail to penetrate the target completely. Figure 2.4 presents different approaches on ballistic limit concepts [20]. The essential difference between those concepts are in the criterion applied to define a perforation. The actual assessment of ballistic limit is usually based upon a statistical performing of large number of tests. The resulting velocity is expressed as V_{50}, which is a 50 % probability that a projectile will perforate a target. A typical V_{50} data is shown for a bullet impacting on a target in Figure 2.5 [21].

Segwick [22] identified possible failure modes in a target plate after ballistic penetration. These modes are represented in Figure 2.6. The following definitions are taken from his

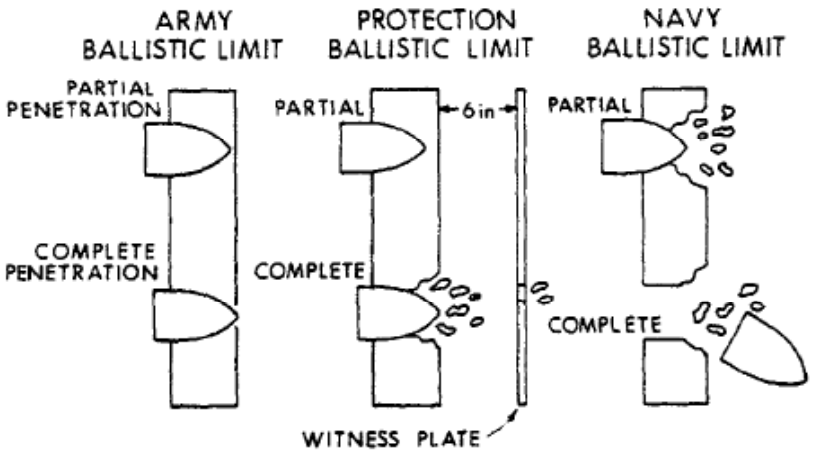

Figure 2.4: Definitions for ballistic limit [20]

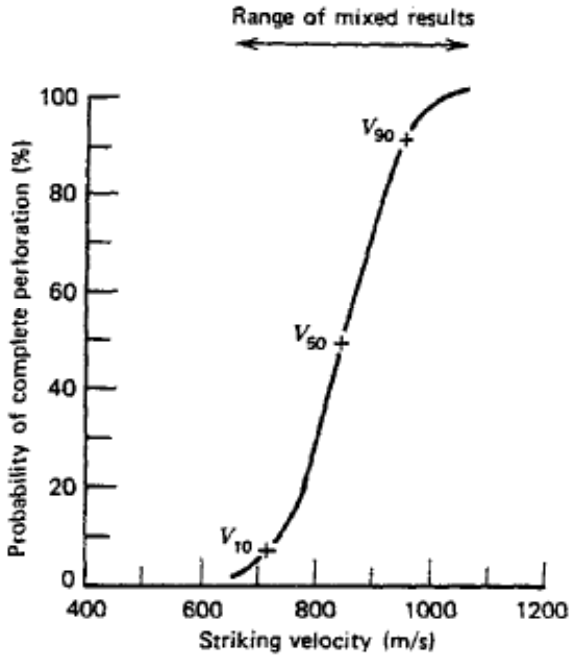

Figure 2.5: Penetration probability curve [21]

discussions.

Fracture due to inertial stress wave Compressive waves propagate into the plate upon impact. If the stress magnitude of this wave exceeds the dynamic yield strength of the target, failure may occur in an unconfined region of the target plate. For a plate target, failure or fracture would occur near the rear target surface. The probability of this type of failure decreases with an increase in target density, hardness or compressive yield or ultimate strength.

Radial fracture behind initial wave front Tensile radial stresses are built up as the compressive wave propagates away from the impact sight. If the target material behavior is tensile and the magnitude of the built up stresses are higher than the ultimate dynamic tensile strength, radial and/or circumferential cracks may occur. The hoop or circumferential stresses will be tensile because of the Poisson's effect, as the compressive wave propagates outward. Radial cracks are caused by this circumferential tensile stress.

Spallation The compressive waves reflect from the rear surface as tensile waves. First, the tensile wave cancels the compressive wave. As the compressive wave propagates to the back of the plate, the amplitude of the compressive wave decays, than the net tensile stress may exceed the ultimate dynamic tensile strength of the target material. In this case, a tensile fracture will occur.

Plugging This type of failure occurs when the projectile pushes a plate plug through the rear surface of the plate. This plug has approximately an equal radius to that of the deformed projectile.

As the hardness of the plate is increased (related to the yield strength or the hardness number), the tendency for plugging increases. The reason is that, it becomes harder for the plate material to be pushed radially outward by the projectile. Thus a narrow shear zone builds up in front of the projectile in the periphery region and the plastic flow is confined to this region. Other parameters that effect the formation of plugging are the relative plate thickness and projectile nose shape. Plugging occurs more easily in thinner plates such that even softer plates may fail in this in case that the impact velocity is not sufficiently close to the ballistic limit so that radial momentum transfer causes severe plate bending. In a similar way, for the impact of a blunt projectile, the chance of this failure increases The cylindrical projectile

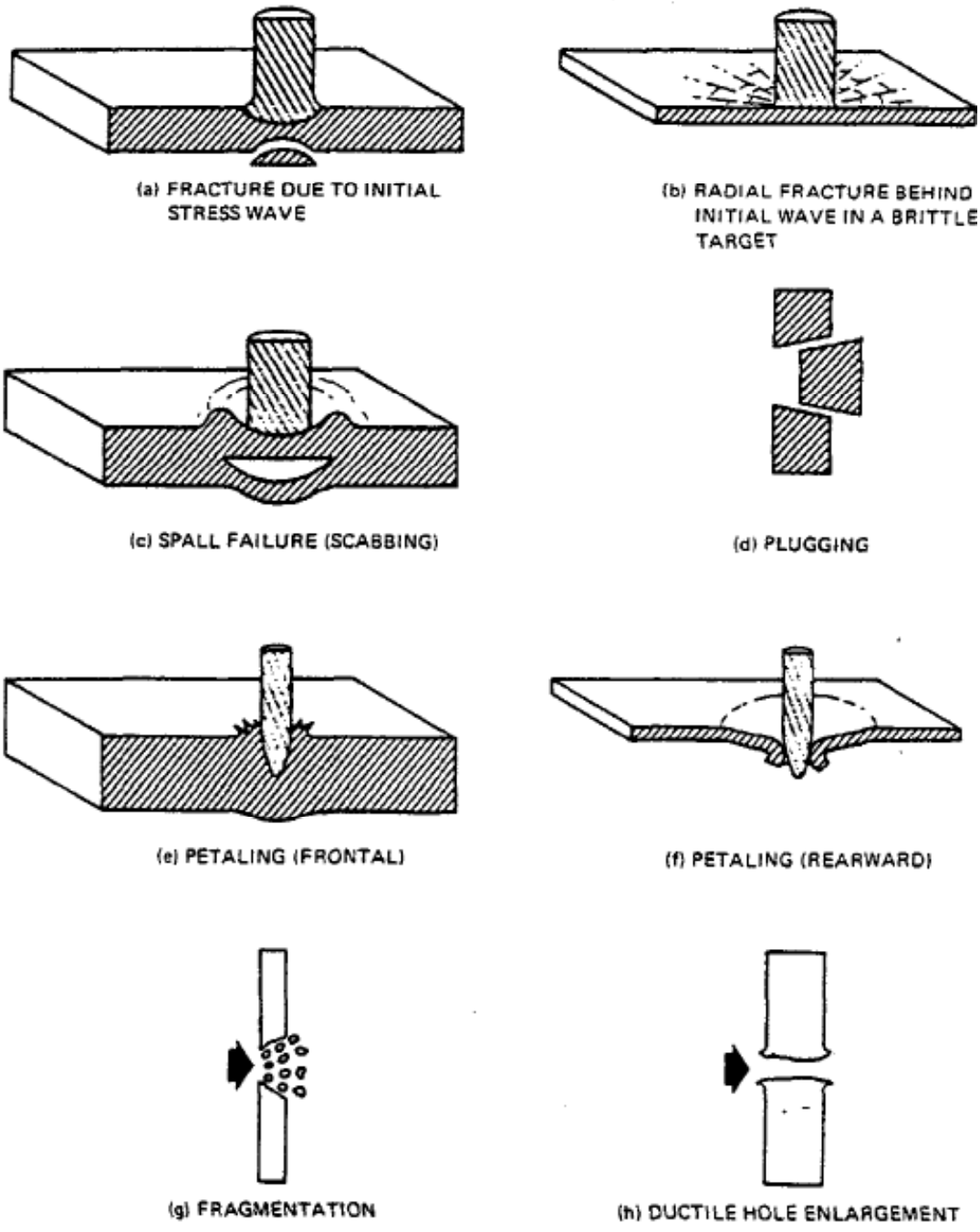

Figure 2.6: Failure modes in plates [22]

would establish a much higher shear stress gradient at its well defined periphery than would a conical or ogive shaped projectile.

The process of plug formation is governed by the shearing failure of the target material. The accompanying rise in temperature due to the plastic flow lowers the resistance of material to shear and thus shearing process becomes more easy.

The shape of the plug depends on the orientation of the maximum shear planes. If there is pure shear at the projectile periphery, the plug will be cylindrical. If tensile or compressive stresses are superimposed in the vicinity of maximum shear, in the case of small amounts of plate bending or the influence of supports; the shape will be a truncated cone, inverted truncated cone, barrel, inverted barrel as well as cylindrical as observed.

Zukas [21] noted that separation of the plug from the target may occur by a conventional fracture mode which is void formation and growth in shear, or by a mechanism known as adiabatic shearing which is characterized by the formation of narrow bands of intense shear. It is believed that the adiabatic shear instability develops at a site of stress concentrations in an otherwise uniformly straining solid. Because of the localized high deformation rates, the work by plastic deformation which is converted almost entirely into heat is unable to dissipate away from the vicinity of plastic deformation zone. Moss [23] claims that shear strain rates within adiabatic shear bands may reach to $10^7\ s^{-1}$ and temperature within the band will be about $10^5\ ^oC$. As a result, rising temperature in the zone enables further local plastic flow and concentrates the local plastic strain more. This process continues up to the propagation of a narrow band of intense plastic strain through the material along planes of maximum shear stress or minimum strength until unloading occurs or the material fractures.

Further discussion regarding the adiabatic shear failure phenomena is addressed in the Section 2.3.

Petalling This type of failure occurs in relatively thin plates. Large circumferential stresses occur trough the thickness of the plate as the compressive wave propagates outward. The stress pattern is formed by the extensive radial flow or significant plate bending. Plates of a relatively ductile material subjected to impact by hard conical or ogive projectiles are likely to exhibit petalling. Also thin plates which bend significantly exhibit this type of failure due to large bending stresses imposed near the free surface of the

plate. The chance of occurring petalling is increased at impact velocities very near the ballistic limit since at these relatively low velocities the momentum transfer is not restricted merely to the region beneath the deforming projectile.

Fragmentation Large amounts of energy are deposited in a short time at higher impact velocities which results in high local stresses. For relatively thin plates, the local material under the projectile nose will fracture, causing fragmentation of the plate.

Ductile hole enlargement For ductile materials, the tip of the conical or ogive projectile concentrates stresses in its vicinity and this results in intense deformations along the axis of the crater [24]. These extensive plastic deformations results in fractures on the axis. The projectile forms a hole in the target along the projectile axis and this hole is enlarged as the perforation proceeds. This type of perforation is characteristic of extremely ductile materials.

Zukas [16] listed a brief summary of the effects observed in both striker and target in the penetration/perforation processes (See Table 2.1). Moreover, some indication of the magnitudes of pressure, strain, strain rate, and temperature encountered in many impact events is given in Table 2.2.

Table 2.1: Physical phenomena occurring in striker and target during perforation [16]

	Phenomena Observed in the Target		Phenomena Observed in the Projectile
1.	Wave propagation (elastic, plastic, hydrodynamic), normal, bending, shear stresses, hydrostatic pressure	1.	Wave propagation
2.	Plate deformation (elastic, plastic)	2.	Permanent deformation
3.	Cracks (initiation,propagation, arrest)	3.	Fracturing
4.	Petalling	4.	Fragmentation
5.	Plugging and spalling	5.	Heating
6.	Frictional effects		
7.	Fragmentation, vaporization, phase changes		

2.3 Thermoplastic Shear Instabilities

Dynamic plastic behavior of materials is influenced by internally generated temperature gradients. These gradients are a function of thermophysical properties as well as strain rate

Table 2.2: Range of physical parameters for target impact response [16]

Impact Event	Pressure (GPa)	Homologous Temperature	Strain	Strain Rate (s^{-1})
Gun launched, 0.5-1.5 km/s	Peak~20-40 Average~3-5	Peak~0.2-0.3 Average~0.1	Peak>1 Average~0.2-0.3	Peak~ 10^6 – 10^7 Average~ 10^4 – 10^5
Self-forged fragment, 1.5-3 km/s	Peak~70 Average~10	Peak~0.4-0.5 Average~0.2	Peak~1 Average~0.2-0.3	Peak~ 10^6 Average~ 10^4 – 10^5
Shaped-charge jet, 3-10 km/s	Peak~100-200 Average~10-20	Peak>1 Average~0.2-0.5	Peak$\gg$ 1 Average~0.1-0.5	Peak~ 10^6 – 10^7 Average~ 10^4 – 10^5

and shear strength. Criteria are presented for the prediction of catastrophic shear in materials. Catastrophic shear occurs when the local rate of change of temperature has a negative effect on strength which is equal to or greater than the positive effect of strain hardening. Catastrophic slip is an influential deformation mechanism during high speed machining and ballistic impact. Structural failure may occur during dynamic loading of components which are designed without regarding to the specific sensitivity of certain materials to catastrophic shear. [25].

Ductile materials possess strain hardening as they are slowly deformed plastically. If the deformation rate is low, the process is isothermal. First, plastic shear strain is restricted to a few weak shear zones within the material [25]. As the weak material in these zones is strengthened by strain hardening the strain is distributed throughout the material. However, the deformation would remain localized if strain hardening did not occur.

For high strain rates, the heat generated by plastic deformation creates local temperature gradients. The highest temperature exists at points of maximum heat generation. If the rate of increase in strength by strain hardening and strain rate hardening is equal to or lower than the rate of decrease in strength by temperature softening which is caused by the local increase of temperature, the deformation process will proceed locally [25]. This instability causes a catastrophic condition which is termed as *adiabatic slip* or *adiabatic shear band* [26].

Recht [25] suggested a relation for the onset of these instabilities. The governing differential equation for shear strength as a function of strain and temperature is given in Eq. 2.1.

$$\frac{d\tau}{d\epsilon} = \frac{\partial\tau}{\partial\epsilon} + \frac{\partial\tau}{\partial T}\frac{dT}{d\epsilon} \tag{2.1}$$

When the slope of the true stress-strain curve becomes zero, catastrophic shear instability will occur at a plastically deforming location. Thus, the left side of Eq. 2.1 can be set as zero to obtain the relationship Eq. 2.2.

$$\frac{\partial\tau}{\partial\epsilon} = -\frac{\partial\tau}{\partial T}\frac{dT}{d\epsilon} \tag{2.2}$$

Then the criteria for catastrophic slip can be expressed by Eq. 2.3.

$$0 \leqq \frac{\frac{\partial \tau}{\partial \epsilon}}{-\frac{\partial \tau}{\partial T}\frac{dT}{d\epsilon}} \leqq 1.0 \tag{2.3}$$

If the ratio given in Eq. 2.3 is unity,it means that the catastrophic slip will happen soon. If the ratio has values between 0 and 1.0, the catastrophic shear failure will happen immediately. High positive values above unity indicate that the strain and strain rate hardening effect is predominant and the shear deformation will be distributed throughout the material. Negative values of the ratio indicate that the increasing temperature hardens the material and the shear deformation will be distributed [25].

The temperature increase by plastic deformation is given by the relation Eq. 2.4 [27]. Relation from Eq. 2.3 can be used together with Eq. 2.4 in the Johnson-Cook strength equation to locate a critical strain value for the onset of instabilities. The author had presented a paper about this subject using the aforementioned method [28]. A shortcoming of the used method was that the critical strain value was independent of strain rate.

$$dT = \frac{\beta}{\rho C_V}\int_0^{\gamma} \tau d\tau \tag{2.4}$$

The relation Eq. 2.4 assumes that C_V is independent of temperature in the regime investigated; β is the fraction of mechanical work that is converted into heat which is experimentally found to be 0.9-1.0.

The process of adiabatic shear failure can be described by three steps which are the instability strain, localization strain and failure strain.To visualize these concepts, shear stress-nominal shear strain curves from torsional Kolsky bar tests by Marchand and Duffy [29] is given in Figure 2.7.

The test depicted in Figure 2.7 was performed at room temperature at a shear strain rate of 1600 s^{-1}. On the curve, the maximum shear stress is obtained about a strain value of 0.27 which corresponds to the instability strain value. Then, the localization strain is located where the shear stress begins to decrease significantly, which means that the stress distribution is very low and the stresses are extremely localized, at a strain value of about 0.38. After the localization strain, catastrophic failure will be expected very immediately at a failure strain of about 0.57.

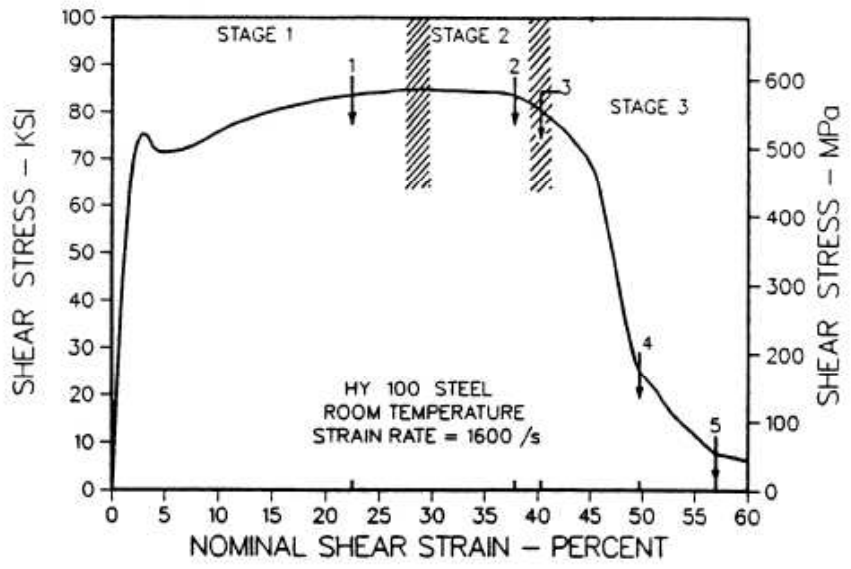

Figure 2.7: Torsional stress-strain curve of HY-100 steel [29]

The model of Raftenberg [30] was included in the Epic finite element code and improvement was observed in hole size predictions for the penetration calculations.

Daridon et al [31] compared the influence of several material constitutive models on the adiabatic shear band spacing. The discussed models were MTS (Mechanical Threshold Stress Model), power law and Johnson-Cook strength models. It was stated that the MTS model seems to be in a better agreement with the experimental results than the other models because of the fact that this model describes the evolution of flow stress based on dislocation concepts. The concept of adiabatic shear band spacing becomes significant when fragmentation of target plate or penetrator is seen.

Lindholm [32] claims that the failure in steel will be adiabatic if the strain rate exceeds $100 s^{-1}$ corresponding shear loading.

2.4 Experimental Studies

In this section, experimental studies from the literature on ballistic penetration of steel and hardened steel plates are presented to support the theories presented in Section 2.2 and 2.3.

Dikshit [33] stated that for the ballistic penetration of metallic plates at ordnance velocities,

literature work can be grouped into two by assuming thin plates which have a $T/D < 1$ (T = plate thickness; D = projectile diameter) and thick plates which have $T/D \geq 1$.

Wingrove [34] and Manganello [35] studied the hardness effect on ballistic performance. It was stated that as the hardness of the plate is increased, the ballistic performance increases up to a certain hardness level. Than, increasing hardness, the performance decreases due to shear plugging induced by the formation and propagation of adiabatic shear bands. For a further increase of the ratio of the hardness of target material to the hardness of the projectile, the ballistic performance improves again due to projectile shutter and deformation.

The work by Dikshit [36] identified that the penetration process under plane strain and plane stress conditions are governed by different characteristics. It was stated that the transition from plane strain to plane stress conditions occurs when the plastic zone in front of the penetrator just impinges on the back face surface of the target plate. It was further noted that all of the penetration of thin plates (for which $T/D \ll 1$) occur under plane stress conditions. For thick steel plates ($T/D \gg 1$), it is all plane strain. The terms plane strain and plane stress were defined to imply constrained/confined or unconstrained/unconfined plastic flow respectively.

Later study of Dikshit et al [33] was concerned about the ballistic penetration of hardened thick steel plates. They used RHA plates with varying hardness in the range HV295-HV520 and of thickness 20 and 80 mm. The penetrator used had a 20 mm diameter, ogive nose shape and velocity of 300-800 m/s. The variation of strength and ductility properties of the target materials is presented in Figure 2.8. The experimental results for 20 mm thick plates were identified for their mechanisms of ballistic penetration is given in Figure 2.9, where the solid and dashed line mark the regions while the circles represent an experimental data point. Filled circles indicate plugging whereas unfilled circles correspond to bulging.

It was concluded that, for plane strain conditions (80 mm thick target plates), increasing the hardness of the plate increases the ballistic performance. The increased performance was attributed to the increased energy dissipated in the plastic zone formed in the plate around the penetrator with increasing hardness (therefore its strength). Moreover the extent of the deformation of the penetrator with increasing hardness of the plate is a major reason.

Reijer [37] conducted an experimental study with ceramic faced armors. He used steel rod projectiles with appropriate geometry and material composition to represent the penetration

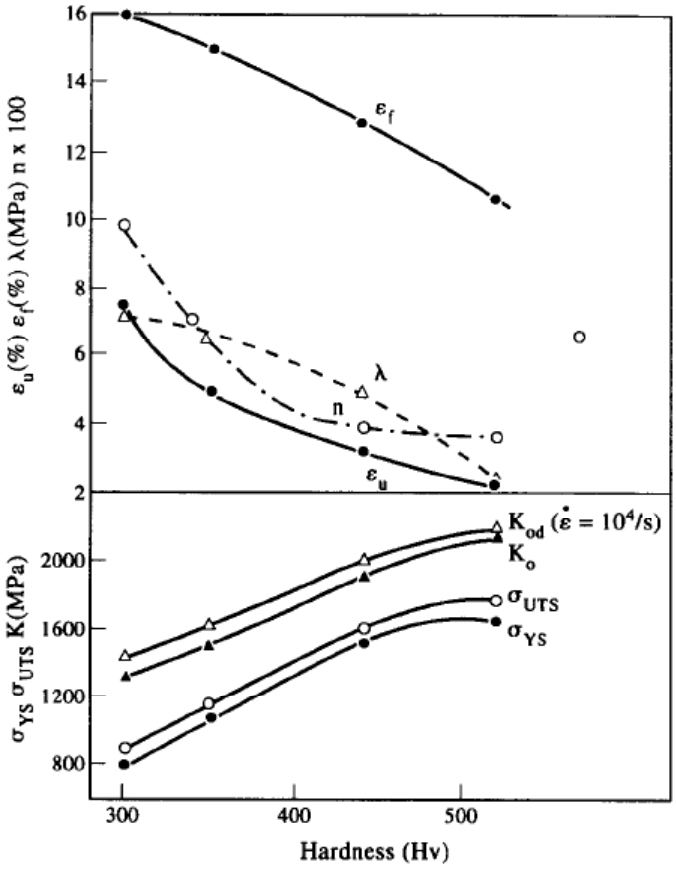

Figure 2.8: The variation of both the strength and ductility parameters as a function of target hardness [33] (K_o : fracture toughness at quasi-static strain rate, K_{od} : dynamic fracture toughness, n : strain hardening exponent, λ : strain rate sensitivity parameter)

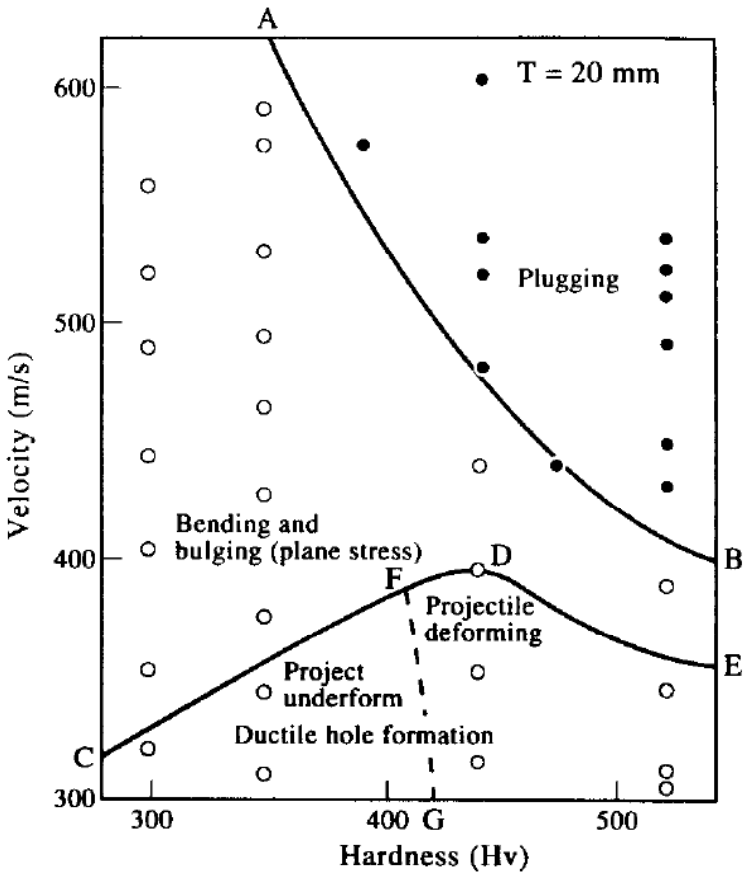

Figure 2.9: A velocity-target hardness space showing dominance of various penetration mechanisms [33]

capability of the 7.62 mm AP projectile. For instance, he used flash X-ray technique to understand the projectile/armor interaction process and the important mechanisms by which these armors and projectiles are defeated.

The rod selected for the study weighted 7.0 grams, had a 6.0 mm diameter and was 31.5 mm long (L/D = 5.3). It was manufactured from steel (ETG-100 von Moos Stahl AG Luzern; R_C = 28). A comparison of the rod and the 7.62 mm AP projectile is given in Figure 2.10 .

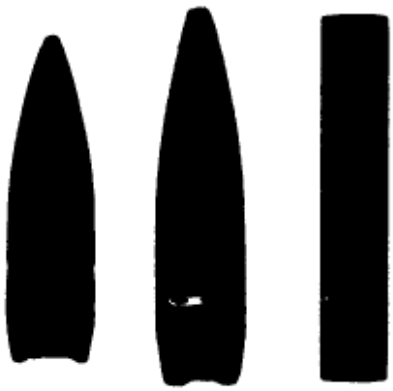

Figure 2.10: 7.62 mm AP projectile core, 7.62 mm AP projectile and steel rod [37]

The ceramic faced armor test panels were composed of 8.1 mm thick Morgan Matroc Hilox 973 alumina and aluminum 6061-T6. The lateral dimensions of the armor panel was set at 155 mm. The thicknesses of four back-up plate configurations were 4.0, 6.0, 3.0+3.0 (unbonded) and 8.0 mm respectively.

It was suggested that, a high tensile strength and a high shear strength are important for ceramic materials apart from a group of static properties as hardness, sound velocity, Young's modulus, Poisson's ratio and porosity [38] in order to distribute the load effectively. Rosenberg [39] confirm that ceramic materials exhibiting a lower (after shock) shear strength are easier to penetrate with blunt projectiles.

The comparisons performed by Reijer [37] showed that a high bending stiffness for the backing plate results in better support of the ceramics fracture conoid as the deformation transient and accumulation of strains are reduced. At later times of impact (>30 us), the back plate's ability to dissipate the kinetic energy of the eroded projectile, ceramic particles and the back plate itself becomes important.

It was shown that when the armors were defeated by the rods when the impact velocity was increased. It was claimed that the increased impact velocity results in a higher impact load, which is accordingly distributed through the ceramic conoid over a section of the supporting back plate. As a result of the increased loading, local shear deformation of the back plate results in high tensile and shear stresses near the edges of the ceramic fracture conoid base at a certain back plate radius. These stresses cause failure of the ceramic conoid and reduce the area over which the impact load is spread. Then the high impact load is distributed to even smaller area, which causes more shear deformation and more conoid base reduction. By this way, load distribution becomes smaller as the area of the projectile in a fast concentration of the impact load.

It was stated that back plate properties such as tensile strength, shear strength, strain to failure and bending stiffness strongly influence a ceramic faced armor's performance. Increasing the back plate's tensile strength, shear strength and strain to failure will enhance the armor's ballistic performance. It was claimed that good tensile load carrying capability reduces the growth of tensile strains in case when deformations grow larger. Also high shear load carrying capacity was found important relying on experiments in which too high shear load on the back-up plate, early in the impact process causes catastrophic back-up plate failure. Moreover a high strain to failure allows the back-up plate to absorb more energy before failing. It was shown that a higher bending stiffness reduces the deformation transient and helps the confinement of the ceramic fracture conoid to its original volume. The lateral extent of the deformation field was found increasing with bending stiffness as a result decreasing the tensile strains in the back plate.

It was claimed that in the case when the back plate fails by tensile strains, the increase of bending stiffness will improve ballistic performance as it prevents the back plate deformation and accumulation of strain. However when back plate failure by shear plugging is considered, decreasing bending stiffness might be better. This decrease supports the response of back plate material surrounding the plug, thus increasing the time necessary for plug separation. As a result, the projectile and plug is decelerated for a longer period, dissipating much more kinetic energy.

Projectile behavior during impact was investigated with the help of flash X-ray photography. From the beginning of the impact, the projectile material was seen being ejected in radial

direction from the impact point. This behavior is depicted in Figure 2.11. The reason of this behavior was attributed to the high circumferential stresses and the grain texture of the projectile material which is in the form of long stretched grains in the axial direction. This behavior was compared with that of a water jet impact on a rigid wall.

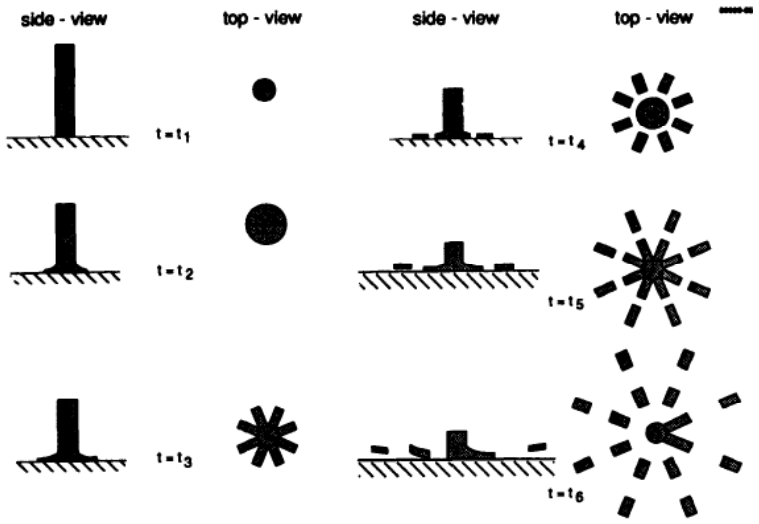

Figure 2.11: A schematic view of the projectile behavior during impact [37]

It was found that plastic deformation of the projectile was limited to a small area adjacent to the projectile-ceramic interface. The radial fracturing process was claimed to be continuing.

Tyrone et al [40] compared the ballistic performance of magnesium alloy AZ31B with RHA and aluminum alloy AA5083-H131 against 7.62 mm APM2 bullet. Their results are depicted in Table 2.3.

Table 2.3: A comparison of the ballistic performance of AZ31B with RHA and AA5083-H131 [40]

Alloy-Temper	Areal Density [kg/m^2]	Plate Thickness [mm]	V50 [m/s]
Steel (RHA)		7.11	524
AA5083-H131	˜55.7	21.03	506
AZ31B-O		31.5	511
Steel (RHA)		17.22	914
AA5083-H131	˜135.2	50.93	853
AZ31B-H24		76.48	863

Borvik et al [41] studied the ballistic penetration of Weldox 460E steel plates by blunt-nosed cylindrical projectiles in the lower ordnance velocity regime. Projectiles were machined from

Arne tool steel, with a nominal mass, diameter and length of 197 g, 20 mm and 80 mm respectively. The projectile material had a hardness value of RC 53 and a yield strength of 1850 MPa. Target plates had a thickness of 12 mm. Graphical representation of test results are depicted in Figure 2.12.

In Figure2.12a, the ballistic limit velocity can be identified by a plot of initial projectile velocity versus residual projectile velocity plot by examining the point where the residual velocity starts to increase from zero. In Figure2.12b, the work/initial kinetic energy is plotted against initial kinetic energy, where the percentage is decreasing with increasing impact energy. At the highest projectile velocities, the absorption of energy is approaching to asymptote, which means that no more energy can be absorbed by the impact process. At the ballistic limit, this percentage was found 35 % less than the amount absorbed under quasi-static plugging conditions. The impact of velocity on the target response was depicted in Figure2.12c, where it is seen that the response is a combination of localized bulging and global dishing. The deformations become localized as the projectile velocity is increased until it reaches a maximum at the ballistic limit. Figure2.12d shows the measured geometrical values as a function of incident projectile velocity. It is seen that target deformation decreases with increasing projectile velocity up to the ballistic limit. The initial and final plug thicknesses were compared and the plug thinning was seen to increase with increasing projectile velocity, while the plug mass stayed almost constant. As the projectile is deformed plastically, the projectile length is decreased and the projectile nose diameter is increased with increasing projectile velocity.

Pickup et al [42] examined the effects of parameters which induce damage to the 7.62 mm AP projectile. These parameters are target impedance, impact stress pulse length, impact velocity and target geometry. It was stated that the extent of damage to the AP round and the morphology of this damage is affected by the dynamic deviatoric strength of the target layers. There is a threshold value of the target hardness beyond which damage is initiated on the projectile on the target interface which fractures and erodes the penetrator. The effects of characteristics of impact stress pulse were found minimal. The effect of dynamic deviatoric strength of target layers was found dependent on the layer thicknesses, as the damage which originates from the back surface of the layer releases constraining pressure which occurs earlier for thinner layers.

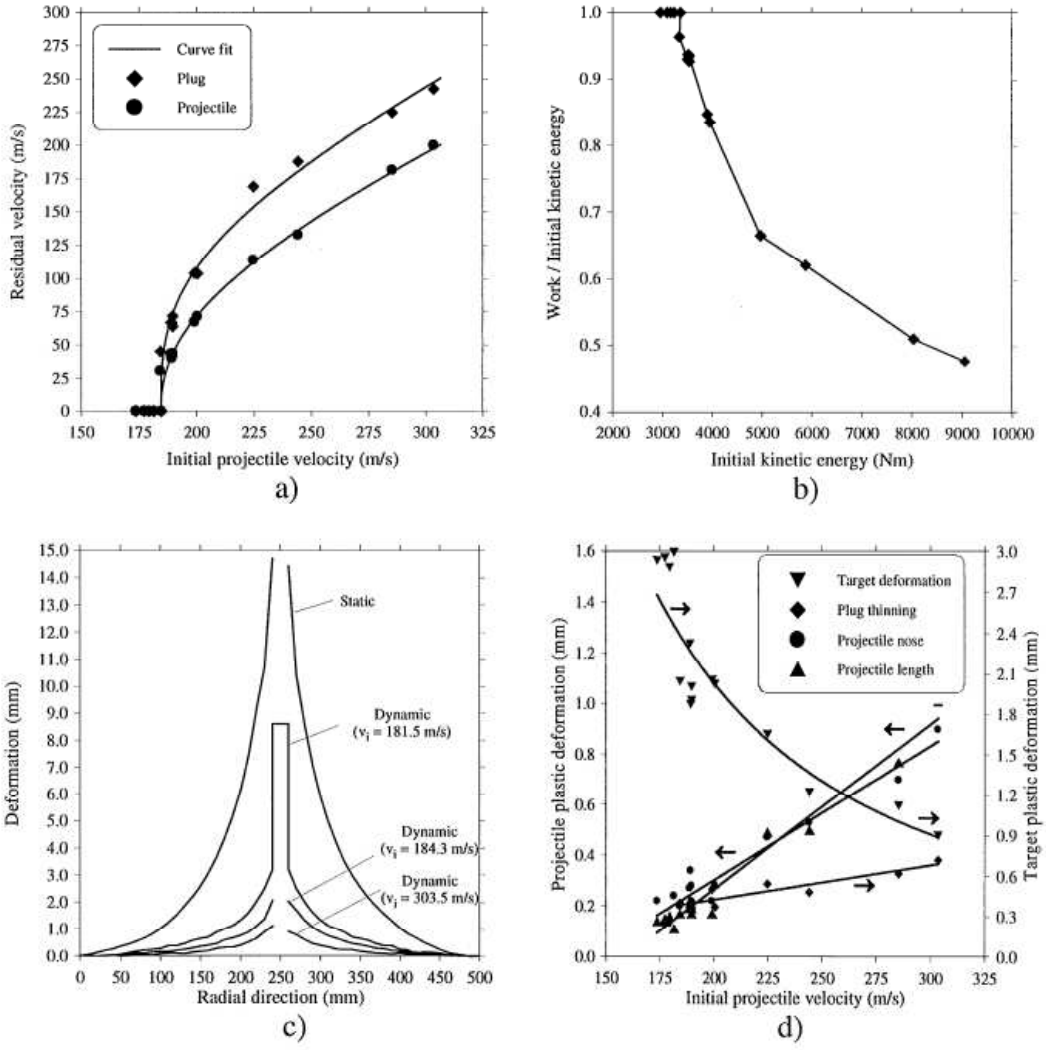

Figure 2.12: Graphical representation of ballistic response of Weldox 460E [41]

2.5 Numerical Studies

This section is devoted to the literature survey on modeling and simulation of the ballistic impact phenomena. There are numerous studies that deals with the modeling issues such as numerical schemes, material modeling and numerical parameters such as mesh intensity.

Schwer [43] compared the Lagrangian scheme with non-Lagrangian numerical schemes such as Eulerian and smooth particle hydrodynamics (SPH). It was concluded that the Eulerian and SPH methods can be an alternative to the Lagrangian method which need an ad hoc erosion criteria for the simulation of ballistic impact. However, applying those methods was found to require a considerable amount of effort.

Vahedi et al [44] conducted a numerical study concerning the ballistic penetration of ceramic faced semi-infinite metal backing. They used LS-Dyna for the analysis. The material behavior of ceramic and metal backing are represented with Elastic-Plastic Hydrodynamic model with pressure cutoff and failure strain. The penetrator material was modeled with Johnson-Cook strength and failure model and Mie-Gruneisen equation of state. The impact velocity of the projectile was taken in the range 750-1350 m/s. The numerical results were found quite in agreement with the test results in terms penetration depth into backing material.

Vignjevic et al [45–49] studied the three different Lagrangian methods that are commonly used for the simulation of impact processes that possesses large deformations. The aim of the study was to apply the element erosion, discrete element and SPH techniques in high velocity impacts and to compare these methods in effectiveness for the determination of post penetration fragmentation characteristics and material failure behavior. In the numerical simulations, an 11 mm diameter sphere projectile was impacted on a 3.2 mm thick plate, and both parts were made of Al2024-T3 material. The impact velocities were taken as 500 m/s and 817 m/s to observe different failure modes in the target. Screenshots regarding the simulations for 817 m/s impact velocity are given in Figure 2.13, 2.14 and 2.15.

All of the three methods were found to be in good agreement with experimental results. It was stated that the element erosion technique made identification of the material failure mode difficult. The SPH method was found to suffer from tensile instability which can influence debris cloud. However, it was claimed that the main advantage of this method was its robustness and it needs fewer assumptions in model development such as the failure forces or strains.

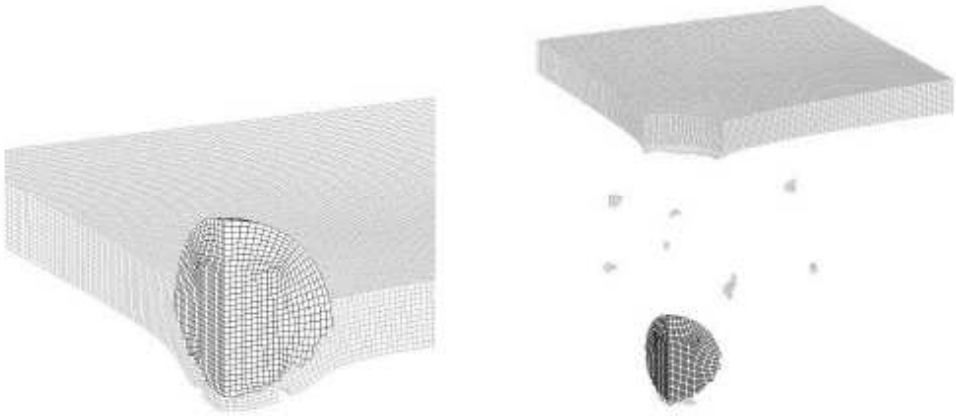

Figure 2.13: Screenshots for the element erosion model at 17μs and 50μs respectively [45]

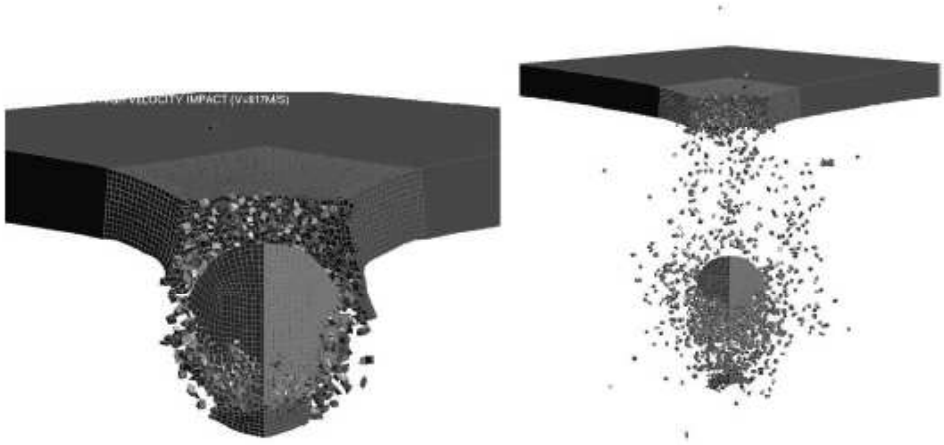

Figure 2.14: Screenshots for the discrete element model at 22μs and 50μs respectively [46]

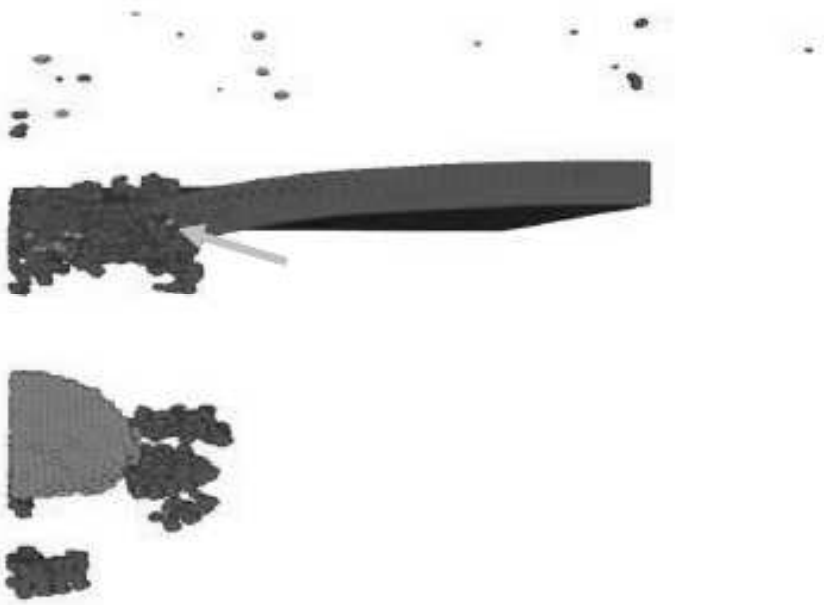

Figure 2.15: Screenshot at the SPH model for $50\mu s$ [47]

The results obtained with the discrete element method was found to represent a potential in the simulation of the material failure mode despite of its necessitating several assumptions during modeling.

Banerjee et al [50] presented a method for the simulation of impact and fragmentation. Regarding this methodology, failed particles are converted into a new material with a different velocity field. The results showed that this method can be used as an alternative method for the numerical modeling of high strain rate, large deformation and penetration phenomena. A comparison with a simulation without using this methodology is presented in Figure 2.16. This methodology was found to produce results that are in good qualitative agreement with experiments.

Resnyansky [51] worked on a split-element algorithm for the numerical simulation of impact problems. This algorithm was implemented in LS-Dyna for modeling of fracture effects. The main promise of this implementation is that it preserves the Lagrangian approach for a clear resolution of fragmentation and it conserves mass compared to the element erosion technique. Furthermore it enables features of continuum damage model and allows embedded cracks. The method was found effective in demonstrating the crack localization zones.

Figure 2.16: Screenshot for two simulations with stresses of the failed particles set to zero and failed particles converted respectively [50]

Park et al [52] presented an optimization procedure with numerical simulation for multi layer plates under ballistic impact. As a part of the work, the effect of mesh size on the solution was stressed. The impact of mesh size on run time and average temperature is depicted in Figure 2.17- 2.18. From these figures, it can be concluded that the run time increases with the increasing the number of elements, however the results seem to converge to a value after some increase in the number of elements.

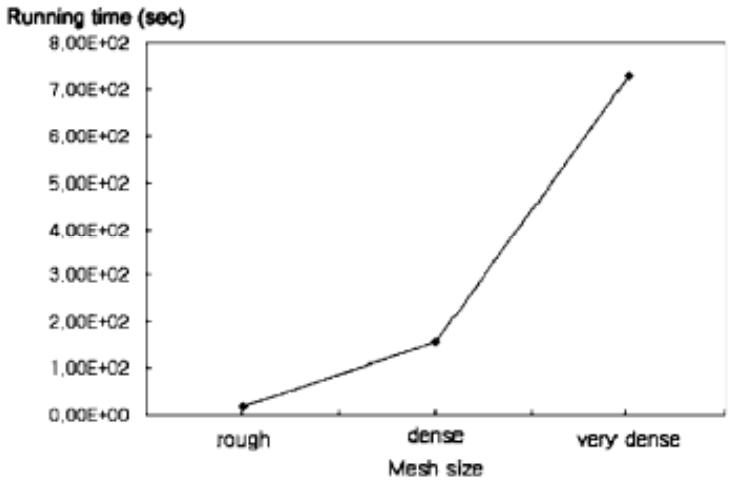

Figure 2.17: Relation of run time with the changing mesh size [52]

Teng et al [53] investigated six fracture models in high velocity perforation. These models were the Wilkins, the Johnson-Cook , the maximum shear stress, the modified Cockcroft-

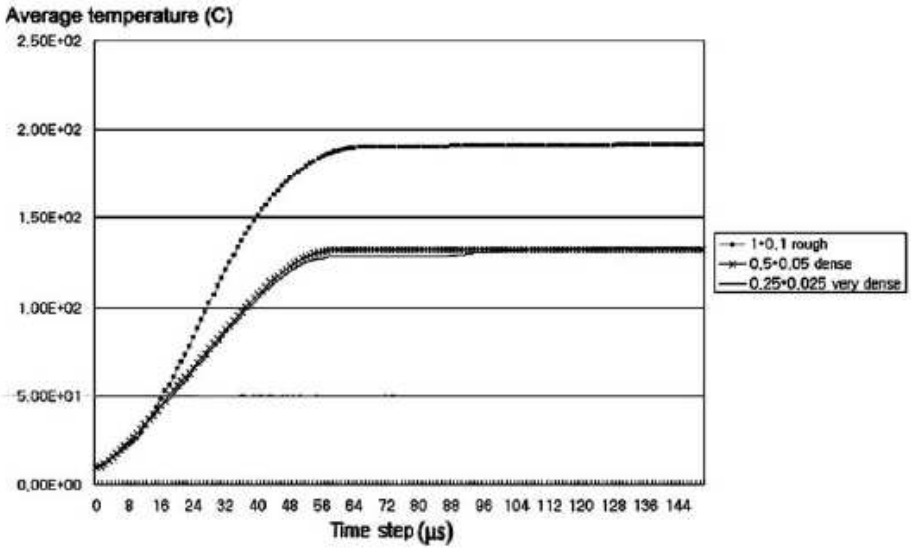

Figure 2.18: Mesh dependency of average temperature [52]

Latham, the constant fracture strain and the Bao-Wierzbicki models and they were implemented to the Abaqus/Explicit by a user subroutine for the modeling of failure processes of a steel and an aluminum target impacted by a projectile. It was found that the Wilkins model predicts spallation of the impact zone beneath the projectile, which is stressed to its power law form of the pressure term. The maximum shear stress model failed to capture the shear plugging feature. It was further stated that the constant failure strain and the modified Cockcroft-Latham models cannot fully characterize the material fracture properties. The Johnson-Cook and the Bao-Wierzbicki models were found to be in good agreement with experimental results in terms of residual velocities and fracture patterns as they account for the stress triaxiality dependence of failure strains.

Chocron et al [11] studied the impact of 7.62 mm APM2 projectile against the edge of a metallic target. The conditions that fracture the core of the projectile were investigated by analytical, numerical and experimental methods. The 3-D numerical model was used to investigate the effects of constitutive modeling, target properties and magnitude of projectile bending strains. It was found that the erosion strain for the jacket material is a critical parameter in accurate numerical modeling of jacketed projectile impact.

The properties of the projectile are examined. A schematic of the projectile and stress-strain graph of the projectile core material are depicted in Figure 2.19 and 2.20 respectively. It was

stated that hard steel core (RC=62) fails at approximately 2% strain at a stress of 2.3 GPa.

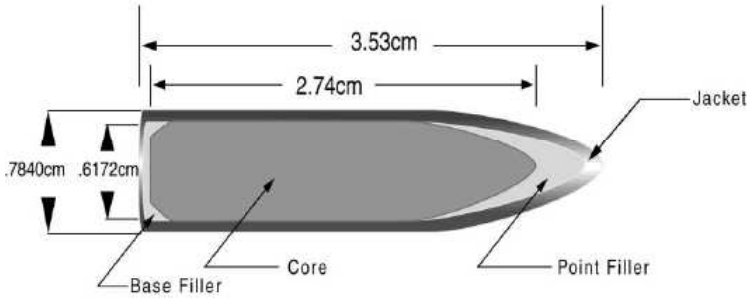

Figure 2.19: A schematic of the 7.62 mm APM2 projectile [11]

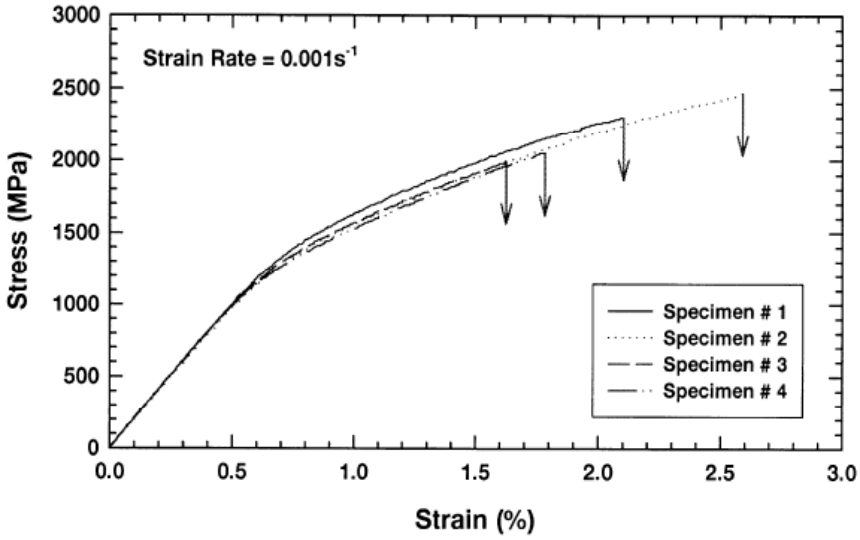

Figure 2.20: Stress-strain response of the projectile core material [11]

The 3-D model of the full projectile is presented in Figure 2.21. A 10% erosion strain was applied for the lead and jacket materials instead of normal 100-150% values to represent better core interactions [11].

Borvik et al [54] conducted a numerical simulation study of plugging failure in LS-Dyna. Blunt projectiles were impacted on Weldox 460 E steel plates. They found that the choice of element size is crucial for adiabatic shear band localization. Agreement with experimental results could be achieved with smaller element sizes. Furthermore, strain rate, temperature and stress state were found to be important parameters for the model. It was further stated that adaptive meshing may become necessary in case of ductile hole enlargement using cone

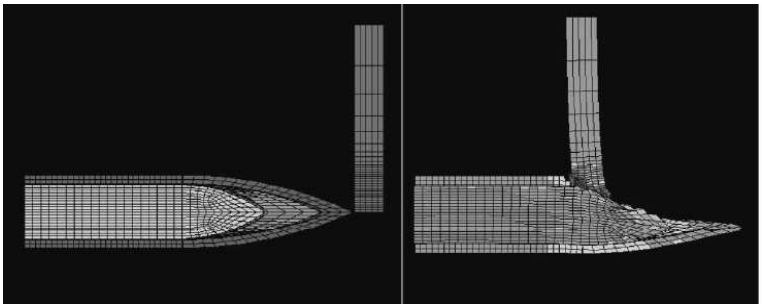

Figure 2.21: 3-D model for the APM2 projectile at initial configuration and at 24μs [10]

projectiles.

Dey et al [55] compared a modified version of the Johnson-Cook strength model with the bcc (body centered cubic) and hcp (hexagonal close packed) version of the Zerilli-Armstrong strength model and combined both with the Johnson-Cook failure model. It was stated that both models were able to represent the physical phenomena qualitatively. Some differences were seen in qualitative results. For practical purposes, it was stated that the Johnson-Cook strength model coupled with the Johnson-Cook failure model would be a good choice in modeling projectile impact of steel plates.

Cockcroft-Latham and the Johnson-Cook failure models were compared by Dey et al [56] in case of projectile impact on steel plates. It was seen that the Cockcroft-Latham model which uses only one parameter gave similar results with the Johnson-Cook failure model. It was further stated that the ballistic limit can be quantitatively estimated independent of the chosen fracture criterion, despite some differences seen during the perforation process.

Hoperstad and Borvik [57, 58] investigated the combined effect of stress triaxiality and strain rate on dynamic behavior of steel. They used an experimental and a numerical approach and found that the strength of the material increases with increasing strain rate. The ductility was found to depend on triaxiality whereas it is independent of the strain rate.

Lenselink [59] used MSC-Dytran for the numerical simulation of oblique penetration of ductile steel plates. The penetrator was modeled by Lagrangian elements whereas the target plate was modeled by Eulerian elements and both processors were coupled. The simulation results were found in agreement with the reported test results.

Kaufmann et al [60] conducted a numerical simulation study for the projectile impact on

aluminum target using LS-Dyna. The influence of mesh intensity on depth of penetration (DOP) results was discussed. It was stated that, there exists an optimum mesh density for which further refinement did not significantly improve the predicted DOP. Moreover the effect of the erosion strain of target was examined and it was found that optimum values lie in the range 1.2 to 1.4 for more accurate DOP predictions.

Borvik et al [61] studied the nose shape effect of the projectile on ballistic perforation of steel plates by conducting numerical simulation in LS-Dyna. Hemispherical, flat and conical nose shapes were studied. Ballistic limit and the residual velocity curve of blunt and hemispherical projectiles from numerical simulations were in agreement with the experimental results for fixed element mesh. However, using fixed element mesh for the conical nose projectiles imparted some problems into the numerical simulation. It was stated that severe hydrostatic compression in the vicinity of the nose tip delayed the element erosion process and caused errors that terminated the simulation. Reducing the material properties of those elements enabled a solution. These results were quantitatively in agreement with the test results despite of some qualitative differences. Therefore it was found that adaptive meshing would be necessary for the simulations including conical nose shapes.

Schwer [62] presented a good review of using the SPH method in ballistic impact problems. He used LS-Dyna for the numerical simulations and modeled the impact region of target plate with SPH particles. He stated that the SPH formulation works better at projectile velocities greater than the ballistic limit. However, the results become suspect when there is significant bending and membrane stretching of the target plate. This situation was stressed to the tensile instabilities of the SPH formulation and it was stated that the target plate appears to have less ballistic resistance with regard to test results.

Borvik et al [3] investigated the ballistic performance of five different steel plates against 7.62 soft core and armor piercing projectiles. The steel plates were represented with the Johnson-Cook strength model combined with the Cockcroft-Latham failure model. It was stated that using the 2-D Lagrangian processor of LS-Dyna was difficult to represent soft core projectile impact. From the impact tests, it was found a linear dependence of the ballistic performance between the target yield strength. The importance of ductility with regard to material strength was found very low. Moreover, the effect of the brass jacket and the lead cap of the armor piercing projectile was stressed. It was found that only using the core part of the projectile

decreases the ballistic limit by 3-5%.

Wisnievski [63] conducted a numerical simulation study of AP projectile impact on RHA plates. It was found that the time spent during the penetration process increases with the increasing yield stress of the projectile material.

Nsiampa [64] presented a numerical and an experimental study regarding the impact of 7.62 mm AP projectile into aluminum 5083 plates. The numerical simulations were found in good agreement with the experimental results. The influence of the jacket and the lead core material in the penetration and perforation mechanisms have been stressed. It was decided that the contribution of the lead core to the DOP results is greater than the contribution of the brass jacket even though the initial kinetic energy of the brass jacket is twice of the one of the lead core.

CHAPTER 3

ENGINEERING MODELS ON BALLISTIC PENETRATION OF STEEL PLATES

Literature survey showed that, analytical approaches seek solution for the residual velocity of the projectile or the minimum thickness of target for ballistic protection, considering the conservation of energy and momentum [65]. Another approach was to classify damage properties. Woodward [66] initiated studies for both approaches. Most of the models in literature were built on these foundations. For instance, Madhu and Gupta [67, 68], studied residual velocity of the projectile and minimum ballistic thickness, based on Woodward's model and taking into account stress effects.

3.1 Thor Equations

The most widely accepted curve fits to test results that are used to determine the ballistic resistance of armor materials to penetration by fragments are the THOR equations. Three equations are provided for the residual velocity of a fragment after penetrating, the striking velocity just to penetrate and the residual mass of a fragment which remains after penetrating.

These equations were a result of work performed under *Project THOR*. Briefly this project consisted of test firing compact steel fragments (with $l/d \approx 1$ and in the shape of short cylinders and cubes) against several types of metallic and non-metallic materials [69, 70]. The experimental cases in which the fragment perforated the target were singled out for the analysis and log-linear fits were performed on the data for each target material, which relates fragment residual velocity and mass to the various impact parameters (Eqns 3.1, 3.2 and 3.3).

$$V_r = V_s - 10^c (hA)^\alpha (m_s)^\beta (\sec\theta)^\gamma V_s^\lambda \tag{3.1}$$

$$V_0 = 10^{c_1} (hA)^{\alpha_1} (m_s)^{\beta_1} (\sec\theta)^{\gamma_1} \tag{3.2}$$

$$m_s - m_r = 10^c (hA)^\alpha (m_s)^\beta (\sec\theta)^\gamma V_s{}^\lambda \tag{3.3}$$

The parameters of the Eqns 3.1, 3.2 and 3.3 are presented on Table 3.1. The list of the coefficients or constants developed in Project THOR for ten metallic materials are presented in Tables 3.2, 3.3 and 3.4.

Table 3.1: Definitions of the parameters in THOR equations

V_r	=	the fragment residual velocity in fps
V_s	=	the fragment striking velocity in fps
V_0	=	the fragment striking velocity just to penetrate
h	=	the target material thickness in inches
A	=	the average impact area of the fragment in square inches
m_s	=	the weight of the original fragment in grains
m_r	=	residual mass of a fragment which remains after penetrating
θ	=	the angle between the trajectory of the fragment and the normal to the target material
c,α,β,γ,λ		are constants or coefficients for the THOR equations determined separately for each material

Table 3.2: Constants for the estimating equations for residual velocity (no particular fragment shape)[69,70]

Form of Equation: $V_r = V_s - 10^c (hA)^\alpha m_s{}^\beta (\sec\theta)^\gamma V_s{}^\lambda$

Target Material	c	α	β	γ	λ	N	σ
Magnesium	6.904	1.092	-1.170	1.050	-0.087	85	600
Aluminum Alloy 2024T-3	7.047	1.029	-1.072	1.251	-0.139	189	400
Titanium Alloy	6.292	1.103	-1.095	1.369	0.167	51	703
Cast Iron	4.840	1.042	-1.051	1.028	0.523	28	195
Face-Hardened Steel	4.356	0.674	-0.791	0.989	0.434	55	546
Mild Homogeneous Steel	6.399	0.889	-0.945	1.262	0.019	117	516
Hard Homogeneous Steel	6.475	0.889	-0.945	1.262	0.019		
Copper	2.785	0.678	-0.730	0.846	0.802	49	562
Lead	1.999	0.499	-0.502	0.655	0.818	71	700
Tuballoy	2.537	0.583	-0.603	0.865	0.828	92	291

Table 3.3: Constants for the estimating equation for the striking velocity just to penetrate (no particular fragment shape)[69,70]

Form of Equation: $V_o = 10^{c_1} (hA)^{\alpha_1} m_s^{\beta_1} (\sec\theta)^{\gamma_1}$

Target Material	c_1	α_1	β_1	γ_1
Magnesium	6.349	1.004	-1.076	0.966
Aluminum Alloy 2024T-3	6.185	0.903	-0.941	1.098
Titanium Alloy	7.552	1.325	-1.314	1.643
Cast Iron	10.153	2.186	-2.204	2.156
Face-Hardened Steel	7.694	1.191	-1.397	1.747
Mild Homogeneous Steel	6.523	0.906	-0.963	1.286
Hard Homogeneous Steel	6.601	0.906	-0.963	1.286
Copper	14.065	3.476	-3.687	4.270
Lead	10.955	2.735	-2.753	3.590
Tuballoy	14.773	3.393	-3.510	5.037

Table 3.4: Constants for the estimating equation for residual mass (no particular fragment shape)[69,70]

Form of Equation: $m_r = m_s - 10^{c} (hA)^{\alpha} m_s^{\beta} (\sec\theta)^{\gamma} V_s^{\lambda}$

Target Material	c	α	β	γ	λ	N*	σ*
Magnesium	-5.945	0.285	0.803	-0.172	1.519	105	11
Aluminum Alloy 2024T-3	-6.663	0.227	0.694	-0.361	1.901	172	22
Titanium Alloy	2.318	1.086	-0.748	1.327	0.459	107	16
Cast Iron	-9.703	0.162	0.673	2.091	2.710	29	13
Face-Hardened Steel	1.195	0.234	0.744	0.469	0.483	54	28
Mild Homogeneous Steel	-2.507	0.138	0.835	0.143	0.761	31	20
Hard Homogeneous Steel	-2.264	0.346	0.629	0.327	0.880	27	29
Copper	-5.489	0.340	0.568	1.422	1.650	70	25
Lead	-1.856	0.506	0.350	0.777	0.934	54	26
Tuballoy	-3.379	0.560	0.447	0.640	1.381	148	30

The THOR equations have been used to determine whether a candidate armor system design will defeat a given fragment threat without having to perform actual test firings on the armor system.

There are several shortcomings of these equations. First, there is a limitation to the fragment shape that can be used with confidence. For instance, predictions from these equations for extrapolations to projectiles with l/d ratios approximately equal to three, show good agreement with experimental results; however, for fragments with larger l/d than three, the accuracy of the predictions is not clear. Second, since it was not possible to test all materials, one must extrapolate the results to other materials. The standard extrapolation method is to select the closest THOR material, then modify the thickness by the ratio of the densities of the desired material to the THOR material. Third, only steel fragments which did not deform or break up

were used as projectiles.

3.2 Recht & Ipson's Model

Recht & Ipson [71] proposed a model for the impact of a plate whose thickness was on the order of the projectile diameter. The schematic of their model is given in Figure 3.1. This model combined conservation of momentum and conservation of energy. For the case of normal impact, the target is assumed to plug, and projectile and plug are assumed to continue forward in contact. From conservation of momentum, the velocity of the projectile and the plug, V_{pp} at the instant of plugging is given by Eq. 3.4.

$$V_{pp} = \left(\frac{m_p}{m_p + m_{tp}}\right) V_0 \tag{3.4}$$

In Eq. 3.4, m_{tp} is the target plug mass. An inherent assumption is that, no momentum is transferred to any portion of the target except the plug mass. Therefore the energy lost during inelastic impact of the projectile and a free plug of mass m_{tp} is given in Eq. 3.5.

$$E_{lost} = \frac{1}{2} m_p V_0^2 \left(\frac{m_{tp}}{m_p + m_{tp}}\right) \tag{3.5}$$

Recht and Ipson accounted for the accompanying energy loss, W, due to the shear stresses between the plug and the target plate in deriving the overall energy equation Eq. 3.6.

$$\frac{1}{2} m_p V_0^2 = E_{lost} + W + \frac{1}{2}(m_p + m_{tp}) V_r^2 \tag{3.6}$$

In Eq. 3.6, V_r is the residual velocity of the projectile and plug after the plug is completely separated from the plate.

Now, they considered that the residual velocity is zero at the ballistic limit to obtain the relation Eq. 3.7 for the shear energy loss at the ballistic limit, which is W_b.

$$W_b = \frac{1}{2} m_p V_{bl}^2 \left(\frac{m_p}{m_p + m_{tp}}\right) \tag{3.7}$$

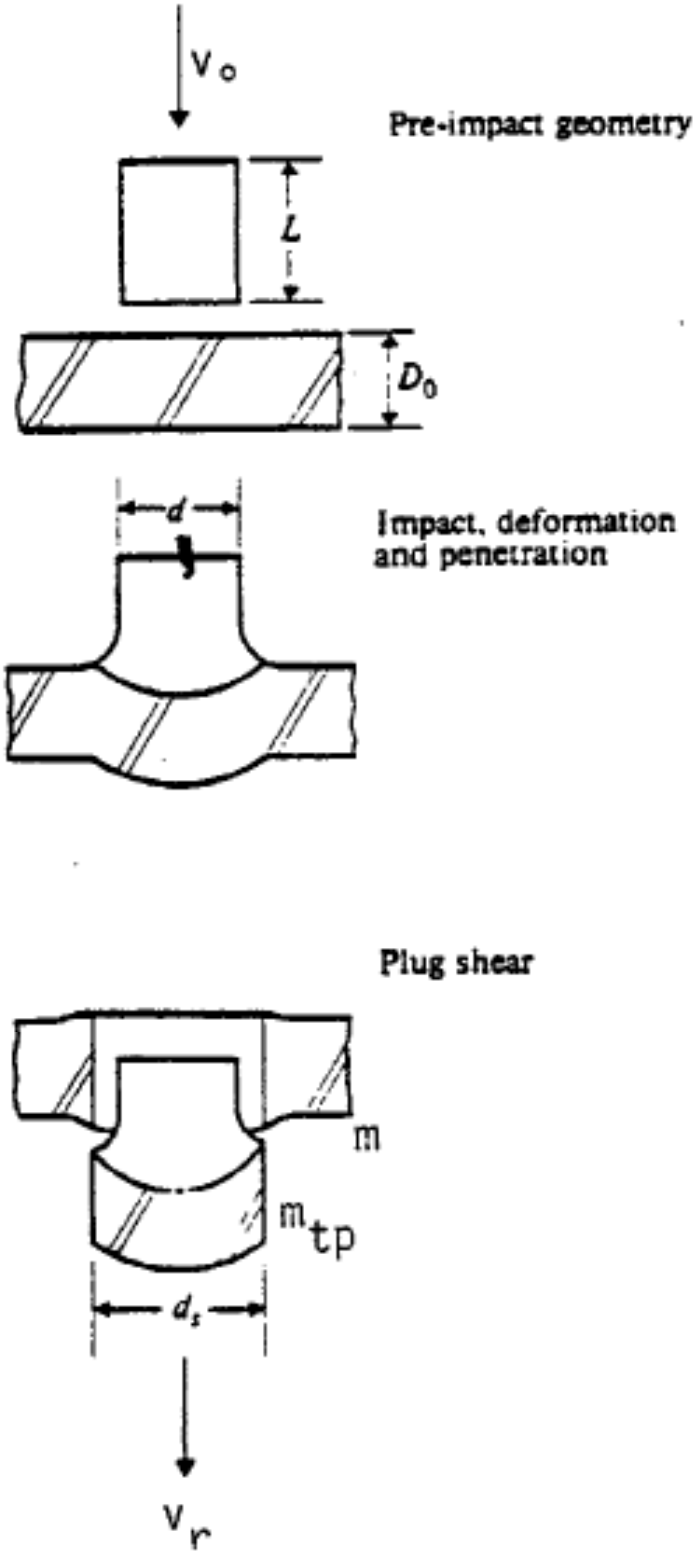

Figure 3.1: Schematic of plate plugging due to the normal impact of deforming projectile [71]

In Eq. 3.7, V_{bl} is the ballistic limit velocity for the projectile and target combination. By assuming that the shear energy W is independent of velocity, then $W = W_b$, and the Eq. 3.8 is given for the residual velocity.

$$V_r = \left(\frac{m_p}{m_p + m_{tp}}\right)\left(V_0^2 - V_{bl}^2\right)^{\frac{1}{2}} \tag{3.8}$$

3.3 Lambert's Model

Lambert [72, 73], proposed Eq. 3.9 and Eq. 3.10 for the residual velocity of the projectile;

$$V_r = 0 \qquad 0 \le V_0 \le V_{BL} \tag{3.9a}$$

$$V_r = \alpha(V_i^p - V_{BL}^p)^{1/p} \qquad V_i > V_{BL} \tag{3.9b}$$

$$\alpha = \frac{m_p}{m_p + M'/3} \tag{3.10a}$$

$$p = 2 + z/3 \tag{3.10b}$$

$$z = (t/D)\sec^{0.75}\theta \tag{3.10c}$$

where V_r, V_θ and V_{BL} are residual, impact and ballistic limit velocities of the projectile, m_p and M' are projectile and target mass, t is thickness of target, D is projectile diameter and θ is obliquity angle in radians.

3.4 Stone's Model

Stone [74] proposed Eq. 3.11 for the depth of penetration of hard projectiles into structurally hard materials.

$$P = (m_p V_0^2/2\pi R^2)2/\rho_t c_t \tag{3.11}$$

In Eq. 3.11; c_t is dependent on the material characteristics in the plastic regime and is dependent on the projectile shape. R is the radius of the projectile.

He compared experimental data for the penetration of armor piercing projectiles into several armor plates made of different materials. Figure 3.2 and 3.3 presents experimental penetration capability of several armor piercing projectiles as a function of areal kinetic energy of the projectile.

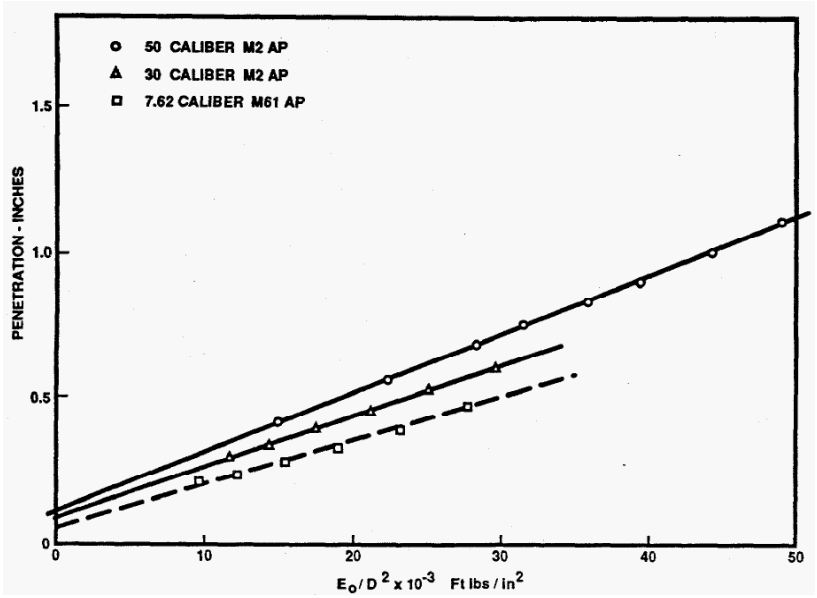

Figure 3.2: The experimental penetration capability of various armor piercing projectiles against Rolled Homogeneous Armor as a function of the areal kinetic energy of the total projectile [74]

3.5 Wijk's Model

Wijk et al [75] proposed a model for rigid projectile penetration and perforation into hard steel and metallic targets. They assumed target material resistance to be constant during penetration, until the front end of the projectile is sufficiently close to the rear surface, where the remaining volume of target material in front of the projectile is crushed and forms secondary fragments. Energy balance was used in the calculations. A simplest model yields depth of penetration in Eq. 3.12.

$$P = \frac{2m_p V_0^2}{\pi d_p^2 \beta Y_T} \tag{3.12}$$

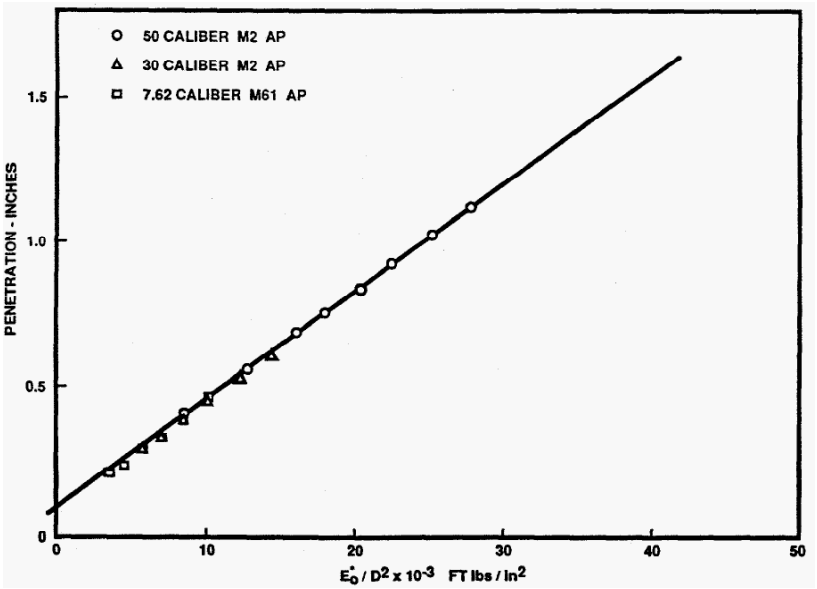

Figure 3.3: The experimental penetration capability of various armor piercing projectiles against Rolled Homogeneous Armor as a function of the areal kinetic energy of only the hardened projectile core [74]

In Eq. 3.12; d_p is the hole diameter, Y_T is the yield strength of the target material and β is a target penetration resistance parameter. It was stated that, $\beta = 5$ was assumed during the calculations.

As it was assumed that the material in front of the projectile is fragmented during the penetration, the perforation phase would start when the front of the projectile is at some distance t^* from the rear surface of the target. The minimum perforation energy W_p for a plate of hard metallic material is given by Eq. 3.13.

$$W_p = \frac{\pi}{8} d_p t(\pi t + \gamma d_p) Y_T \qquad t < t^* \qquad (3.13a)$$

$$W_p = \frac{\pi}{4}(t - t^*) d_p^2 \beta Y_T + \frac{\pi}{8} d_p t^*(\pi t^* + \gamma d_p) Y_T \qquad otherwise \qquad (3.13b)$$

In Eq. 3.13; γ is an empirically determined parameter describing target perforation resistance and is taken as 1 for 7.62 mm AP projectiles. Thickness t^* can be determined by Eq. 3.14.

$$t^* = \frac{d_p}{2\pi}(2\beta - \gamma) \qquad (3.14)$$

The mass m_T of fragments can be estimated by Eq. 3.15 where t_T is smaller of t and t^*.

$$m_T \approx \frac{\pi}{4} d_p^2 t_T \rho_T \tag{3.15}$$

Finally, residual velocity of the projectile (and secondary fragments) is given by Eq. 3.16.

$$V_r = \sqrt{\frac{m_p^2 V_0^2 - 2W_p}{m_p + m_T}} \tag{3.16}$$

3.6 Woodward's Model

Woodward [66] postulated Eq. 3.17 where he used energy balance.

$$(1/2) m_p V_0^2 = \pi D^2 \sigma_0 t/2 \tag{3.17}$$

where σ_0 is yield strength of target material. Woodward's model was found effective for ductile materials whereas it was unsuccessful for brittle materials.

3.7 Thompson's Model

Thompson [76] proposed Eq. 3.18 based on Woodward's model.

$$V_r^2 = V_0^2 - \frac{4\pi r_p^2 h_0}{m_p} \left(\sigma_y/2 + V_0^2/3\right) \tag{3.18}$$

The energy required for penetration defined by Eq. 3.19.

$$E_c = \pi r_p^2 t \left(0.5\sigma_y + A\rho \left(\frac{V_0 r_p}{L_n}\right)^2\right) \tag{3.19}$$

where A is a constant for projectile shape. It is taken as 1 and 1.86 for conical and spherical shapes and L_n is length of the projectile.

3.8 Übeyli & Demir Model

Thompson's model ignored percent elongation properties of materials which is an indicator for toughness and ductility. Based on Thompson's model Demir and Übeyli [77] suggested a model for ballistic thickness prediction. The model uses ultimate strength instead of yield strength. Then corrections were made for ballistic thickness values taking into account percent elongation values. Eq. 3.20 states ballistic thickness of the target material, h_0 as;

$$h_0 = ((100 - \varepsilon u)/100)\, T \tag{3.20a}$$

$$T = \frac{\left(\frac{1}{2} m_p V_0^2\right)/36}{\pi r_p^2 \left(0.5\sigma_{UTS} + A\rho\left(\frac{V_o r_p}{L_n}\right)^2\right)} \tag{3.20b}$$

where ε stands for percent elongation and u is a calibration constant which is taken as 2 for elongations higher than 13 % and 3 for smaller values.

3.9 Pol's Model

Pol et al [78] suggested a model for perforation of ogive-nose projectiles into thin metallic plates. They assumed asymmetry petalling failure in the target plate and analysis was done by using energy balance and work done. The ballistic limit velocity V_b is a function of total work done and represented by Eq. 3.21.

$$V_b = \left(\frac{2W}{m_p}\right)^{\frac{1}{2}} \tag{3.21}$$

Total work done (W) is sum of plastic deformation W_p, work done is transferring material to new position W_d and work for bending of petals W_b. Eq. 3.22 represents these aforementioned work values.

$$W_p = \frac{\pi}{2} b^2 Y t \tag{3.22a}$$

$$W_d = \frac{2\pi\rho_t V_0^2 b^4 t^2}{3L^2} \tag{3.22b}$$

$$W_b = \frac{\pi^2 b t^2 Y}{4} \tag{3.22c}$$

In Eq. 3.22, Y is the yield strength of target material, b is radius of hole and L is the nose length of the projectile.

CHAPTER 4

FUNDAMENTALS OF EXPLICIT NUMERICAL ANALYSIS OF BALLISTIC PENETRATION

This chapter covers the fundamentals of numerical analysis by giving a brief introduction to the hydrocode used in the current study which is ANSYS Autodyn®.

Autodyn is a general purpose numerical analysis tool for the simulation of nonlinear dynamic events. It employs a coupled finite difference/finite volume approach and an explicit time integration algorithm. It includes the following numerical processors [79]:

- Lagrange processor for solid continua and structures
- Euler processor for modeling fluids, gases and large distortion
- ALE (Arbitrary Lagrange Euler) processor for specialized flow models
- Shell processor for modeling thin structural elements
- SPH (Smooth Particle Hydrodynamics), an alternative meshless approach

It is crucial to emphasize the advantages and disadvantages of these aforementioned processors to determine the processor that is used in numerical studies.

In the Lagrangian processor, the elements move with material flow velocity. Material remains within its initial elemental definition with no transport of material from cell to cell. It is the most popular numerical scheme in ballistic penetration modeling. A typical example is illustrated in Figure 4.1. Several advantages and disadvantages regarding this processor due to its nature are itemized below.

- As there are less computations per cycle, a fast solution is performed
- It is easier to follow material interfaces, free surfaces and history dependent material behavior
- Mass conservation is automatically satisfied with this processor
- It possible to apply various boundary conditions
- Damage and plasticity is handled easily
- If excessive material movement occurs, the numerical mesh may become highly distorted leading to an inaccurate and inefficient solution or even termination
- In case of large material deformation, it is necessary to handle techniques such as element erosion (which has physically no meaning), mesh rezoning or remeshing

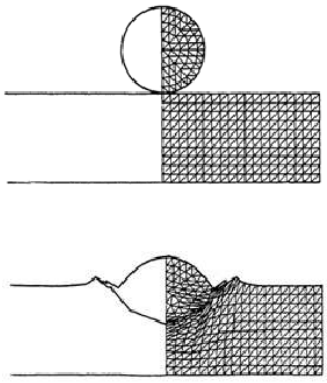

Figure 4.1: An example of Lagrangian modeling [21]

The Eulerian processor employs a control volume method to solve equation that governs conservation of mass, momentum and energy. Thus, the elements stay still in the Eulerian space and material flow occurs between elements. A typical illustration is given in Figure 4.2. Several advantages and disadvantages regarding this processor due to its nature are itemized below.

- With this processor, it is possible to handle extreme deformations
- It is suitable for modeling of fluid flow

- It is difficult to track free surfaces, material interfaces and history dependent material behavior
- Care must be given to limit the numerical diffusion associated with the material convection from cell to cell
- As it employs more computations per cycle regarding the Lagrangian processor, the numerical solution takes more time
- It is necessary to model the empty space with elements which means a larger solution domain
- It is necessary to employ smaller elements regarding the Lagrangian processor so that the solution is less efficient
- It is difficult to model damage and plasticity
- Contact treatment is more tedious

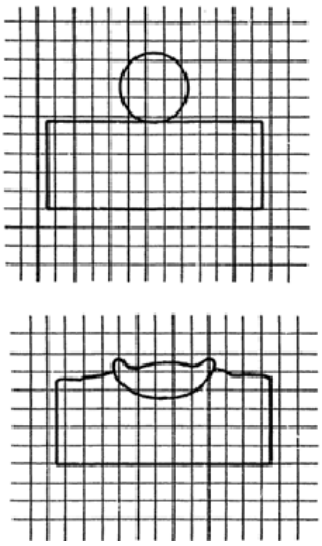

Figure 4.2: An example of Eulerian modeling [21]

The ALE processor is an extension of the Lagrangian method. An additional computational step is employed to move the grid and remap the solution onto the new grid. It is still under development and generally slower than both methods described above.

SPH is a relatively new numerical method for simulating ballistic impact problems. Although it is still under development, it has a big advantage since no grid tangling occurs because it is

a gridless technique. As it is a Lagrangian method [80], it is very flexible for incorporating sophisticated material models. Moreover it is very suitable for excessive deformation. However, there are several shortcomings. There is an instability problem in tension. As there is no topology defined over the particles, it is harder to assign boundary conditions. The calculations are time consuming since the processor employs neighbor searching (since there is no topology).

Considering the advantages and disadvantages of aforementioned methods; it was decided to use the Lagrangian processor in the numerical simulation studies. Moreover it was concluded that the SPH solver can be a serious alternative to the Lagrangian processor in case of brittle material behavior.

4.1 Computational Scheme

The Lagrangian processor expresses the partial differential equations of conservation of mass, momentum and energy in Lagrangian coordinates. Together with the material model and a set of initial and boundary conditions, the complete solution of a problem is defined. The Lagrangian grid is deformed with the associated material, thus the conservation of mass is automatically satisfied. The density is calculated from current volume of grid element and the initial mass by Eq. 4.1.

$$\rho = \frac{\rho_0 V_0}{V} = \frac{m}{V} \tag{4.1}$$

Acceleration is related to the stress tensor σ_{ij} by the partial differential equations of conservation of momentum (see Eq. 4.2).

$$\begin{aligned} \rho\ddot{x} &= \frac{\partial \sigma_{xx}}{\partial x} + \frac{\partial \sigma_{xy}}{\partial y} + \frac{\partial \sigma_{xz}}{\partial z} \\ \rho\ddot{y} &= \frac{\partial \sigma_{yx}}{\partial x} + \frac{\partial \sigma_{yy}}{\partial y} + \frac{\partial \sigma_{yz}}{\partial z} \\ \rho\ddot{z} &= \frac{\partial \sigma_{zx}}{\partial x} + \frac{\partial \sigma_{zy}}{\partial y} + \frac{\partial \sigma_{zz}}{\partial z} \end{aligned} \tag{4.2}$$

Then the stress tensor is separated into a hydrostatic component p and a deviatoric component

s (see Eq. 4.3). The hydrostatic pressure is augmented by a pseudo-viscous force q. This process is illustrated in Figure 4.3.

$$\begin{aligned}
\sigma_{xx} &= -(p+q) + s_{xx} \\
\sigma_{yy} &= -(p+q) + s_{yy} \\
\sigma_{zz} &= -(p+q) + s_{zz} \\
\sigma_{xy} &= s_{xy} \\
\sigma_{yz} &= s_{yz} \\
\sigma_{zx} &= s_{zx}
\end{aligned} \tag{4.3}$$

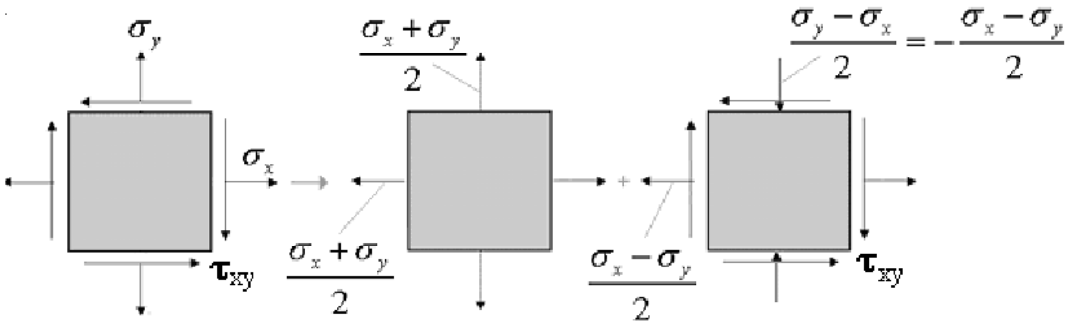

Figure 4.3: Resolution of stress tensor (2D for simplification) into hydrostatic (change in volume, EOS) and deviatoric terms (change in shape, strength)

In Eq. 4.3, the hydrostatic pressure has a negative sign since the usual notation assumes positive stress in tension and negative in compression. The strain tensor ε_{ij} is determined from the relation between strain rates and nodal velocities (see Eq. 4.4).

$$
\begin{aligned}
\dot{\varepsilon_{xx}} &= \frac{\partial \dot{x}}{\partial x} \\
\dot{\varepsilon_{yy}} &= \frac{\partial \dot{y}}{\partial y} \\
\dot{\varepsilon_{zz}} &= \frac{\partial \dot{z}}{\partial z} \\
\dot{\varepsilon_{xy}} &= \frac{1}{2}\left(\frac{\partial \dot{x}}{\partial y} + \frac{\partial \dot{y}}{\partial x}\right) \\
\dot{\varepsilon_{yz}} &= \frac{1}{2}\left(\frac{\partial \dot{y}}{\partial z} + \frac{\partial \dot{z}}{\partial y}\right) \\
\dot{\varepsilon_{zx}} &= \frac{1}{2}\left(\frac{\partial \dot{z}}{\partial x} + \frac{\partial \dot{x}}{\partial z}\right)
\end{aligned}
\tag{4.4}
$$

The strain rates from Eq. 4.4 are related to the rate of change of volume by Eq. 4.5.

$$
\frac{\dot{V}}{V} = \dot{\varepsilon_{xx}} + \dot{\varepsilon_{yy}} + \dot{\varepsilon_{zz}} \tag{4.5}
$$

The deviatoric part of the stress rate tensor is dealed by Hooke's Law and Eq. 4.5 in the elastic region (see Eq. 4.6.

$$
\begin{aligned}
\dot{s_{xx}} &= 2G\left(\dot{\varepsilon_{xx}} - \frac{1}{3}\frac{\dot{V}}{V}\right) \\
\dot{s_{yy}} &= 2G\left(\dot{\varepsilon_{yy}} - \frac{1}{3}\frac{\dot{V}}{V}\right) \\
\dot{s_{zz}} &= 2G\left(\dot{\varepsilon_{zz}} - \frac{1}{3}\frac{\dot{V}}{V}\right) \\
\dot{s_{xy}} &= 2G\dot{\varepsilon xy} \\
\dot{s_{yz}} &= 2G\dot{\varepsilon yz} \\
\dot{s_{zx}} &= 2G\dot{\varepsilon zx}
\end{aligned}
\tag{4.6}
$$

Further effects of deviatoric stresses when in presence of plastic flow are discussed in Section 4.2.

The equation of state relates pressure p to the density ρ and specific internal energy e in generalized form as shown in Eq. 4.7, which is solved simultaneously with conservation of energy (see 4.8).

$$p = f(\rho, e) \tag{4.7}$$

$$\dot{e} = (1/\rho)\left(\sigma_{xx}\dot{\varepsilon_{xx}} + \sigma_{yy}\dot{\varepsilon_{yy}} + \sigma_{zz}\dot{\varepsilon_{zz}} + 2\sigma_{xy}\dot{\varepsilon_{xy}} + 2\sigma_{yz}\dot{\varepsilon_{yz}} + 2\sigma_{zx}\dot{\varepsilon_{zx}}\right) \tag{4.8}$$

The computational cycle is summarized in Figure 4.4. The steps are itemized below.

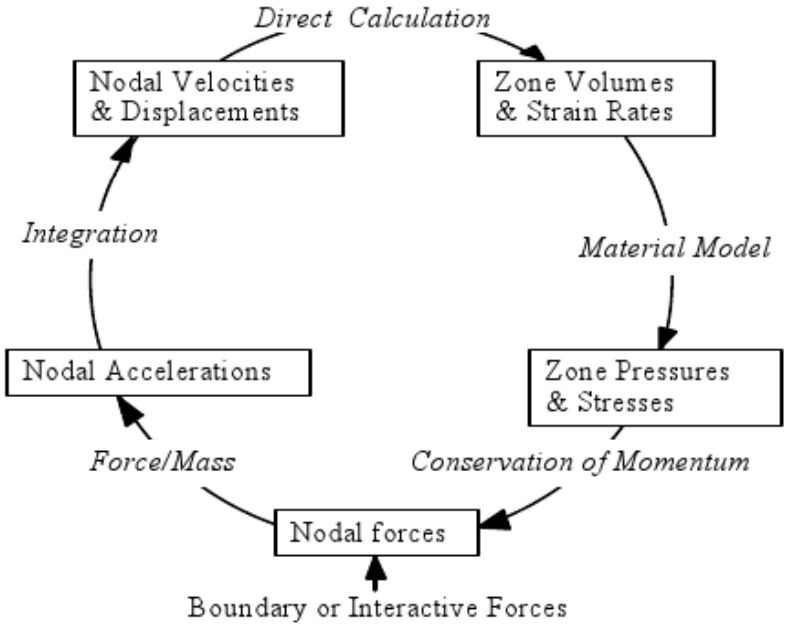

Figure 4.4: Lagrangian computation cycle [79]

- At the beginning of the cycle, the new locations of each node are calculated from nodal velocities with time integration over timestep.
- From new node locations, new element densities and element strain rates are calculated.
- Stresses are calculated from strain rates.
- Element deformation is separated into two components (illustrated in Figure 4.3).
- Changes in volume create hydrostatic stresses, which is called pressure.
- Changes in shape create deviatoric stress field.

- Pressure is controlled by equation of state.
- Deviatoric stresses are dealed by the Hooke's Law in the elastic region and strength model in the plastic region.
- With the integration of failure model, material modeling is complete.
- Nodal forces are computed from internal stresses in the element.
- Boundary conditions and contact forces are applied on nodes if exist.
- Nodal acceleration are calculated from nodal forces.
- Time integration of nodal acceleration over timestep gives nodal velocities.
- Computations defined for a single cycle are repeated until a predetermined time or cycle limit.

4.2 Material Modeling

In addition to the governing differential equations governing dynamic material motion, it is necessary to define further relation between the flow variables. This is accomplished by the material model which relates stress to deformation and internal energy. As depicted in Figure 4.3, the stress tensor is separated into a hydrostatic pressure and a deviatoric stress tensor, which is associated with the resistance of material to shear distortion. The relation between the hydrostatic pressure, the local density and local specific energy is called an equation of state (EOS).

4.2.1 Equation of State

Two kinds of equation of state were used in the simulation studies, which are discussed in the following subsections.

4.2.1.1 Linear Equation of State

In many cases, it can be assumed that the effects of changes in entropy is negligible so that pressure p may be considered solely as a function of density [79]. The approach used in the

hydrocode was to express initial elastic behavior by an approximation to Hooke's Law which is denoted in Eq. 4.9, where $\mu = (\rho/\rho_0) - 1$, and K is the material bulk modulus.

$$p = K\mu \tag{4.9}$$

It was noted that [79], this equation of state can be used for fairly small compressions and must be avoided in case of large compressions and shock loading.

4.2.1.2 Shock Equation of State

This equation of state is necessary in case of shock loading and large compressions.

The Rankine-Hugoniot equations for the shock jump conditions can be regarded as defining a relation between any pair of the variables ρ (density), p (pressure), e, u_p (particle speed) and U (wave speed). In many dynamic experiments making measurements of u_p and U, it has been found that for most solids and many liquids over a wide range of pressure there is an empirical linear relationship between these two variables [79] in the form Eq. 4.10.

$$U = c_0 + su_p \tag{4.10}$$

Based on the shock hugoniot, a Mie Gruneisen form of equation of state is established by Eq. 4.11.

$$p = p_H + \Gamma\rho(e - e_H) \tag{4.11}$$

where Γ is the Gruneisen Gamma for which it is assumed that $\Gamma\rho = \Gamma_0\rho_0 = constant$ and

$$p_H = \frac{\rho_0 c_0^2 \mu(1+\mu)}{[1-(s-1)\mu]^2} \tag{4.12}$$

$$e_H = (1/2)\frac{p_H}{\rho_0}\left(\frac{\mu}{1+\mu}\right) \tag{4.13}$$

4.2.2 Strength Model

If the material is a solid and has a finite shear strength, it is necessary further to define a strength model to relate shear stress and strain. It is also required to define transition between elastic and plastic strain, for both compression and tension.

The well known Johnson-Cook [81] model was used to define strength of the materials. This constitutive model aims to model the strength behavior of materials subjected to large strains, high strain rates and high temperatures. Such behavior might arise in problems of intense impulsive loading due to high velocity impact and explosive detonation. The model defines the yield stress Y as an explicit function of strain hardening, strain rate hardening and temperature softening in the form Eq. 4.14.

$$Y = \left[A + B\varepsilon_p^n\right]\left[1 + C\log\varepsilon_p^*\right]\left[1 - T_H^m\right] \tag{4.14}$$

where

ε_p = effective plastic strain

ε_p^* = normalized effective plastic strain rate

T_H = homologous temperature = $(T - T_{room})/(T_{melt} - T_{room})$

The five material constants are A, B, C, n and m. The first set of brackets in Eq. 4.14 gives the stress as a function of strain, which can be found by quasi-static tensile testing ($\varepsilon_p^* = 1.0 sec^{-1}$ and $T_H = 0$). A is the basic yield stress at low strains whereas B and n define strain hardening. The second and third set of brackets represent the effects of strain rate hardening and temperature softening. With the thermal softening, the yield strength drops to zero at the melting temperature T_{melt}. The material constants can be obtained empirically via dynamic Split Hopkinson Bar tensile tests over a range of temperatures and strain rates. The obtained model constants were checked by calculations of Taylor tests of impacting metal cylinders on rigid metal targets which provided strain rates in excess of $10^5 sec^{-1}$ and strains in excess of 2.0 [81].

4.2.3 Failure Model

The well known Johnson-Cook failure model [82] was used to model dynamic material failure. With a similar form of the strength model; the fracture strain, which is a material property, is expressed to be an explicit function of strain rate, temperature, and pressure in Eq. 4.15.

$$\varepsilon^f = (D_1 + D_2 \exp D_3\sigma^*)(1 + D_4 \ln \dot{\varepsilon^*})(1 + D_5 T^H) \tag{4.15}$$

The dimensionless pressure-stress ratio (or the stress triaxiality ratio) is defined as $\sigma^* = \sigma_m/\bar{\sigma}$, where σ_m is the main stress, $(\sigma_1 + \sigma_2 + \sigma_3)/3$, and $\bar{\sigma}$ is the effective stress (or the von Mises equivalent stress ($\sqrt{3J_2}$), where J_2 is the second invariant of the stress devaitor). The dimensionless strain rate $\dot{\varepsilon^*}$ is equal to $\dot{\varepsilon}/\dot{\varepsilon_0}$, where $\dot{\varepsilon_0}$ is a unity strain rate. T^H is termed as the homologous temperature. The temperature may be due to the externally applied thermal loads or due to internal heating from plastic work, as covered in Section 2.3. D_1, D_2, D_3, D_4 and D_5 are the fracture model parameters. The model parameters can be determined from conventional laboratory experiments.

The Johnson-Cook model uses a linear summation concept to account for changes during the loading history. It computes both changes in the failure strain with stress state, strain rate and temperature as well as the accumulation of some type of damage during the loading process. However, the model does not account for any damage degradation of material strength and/or stiffness. Stresses and pressure are abruptly set to zero when damage reaches a critical value. Therefore, it is classified as an instantaneous failure model. Damage is calculated as a cumulative value in Eq. 4.16, and failure is set to occur at a critical value (usually 1).

$$D = \Sigma \frac{\Delta\varepsilon}{\varepsilon^f} \tag{4.16}$$

where $\Delta\varepsilon$ is the increment of equivalent plastic strain which occurs during the tensile loading history and ε^f is the equivalent strain to fracture corresponding to the instantaneous conditions when that increment of strain is accumulated.

4.2.4 Element Erosion

It was stated in the beginning of Chapter 4 that the Lagrangian processor has some limitations. Although it is very capable of modeling dynamic solid behavior, including plastic flow and failure; large deformations lead to grid distortions and tangling. These distortions can seriously impair the progress of the calculations by leading very small timesteps, mesh tangling or even termination. Therefore Autodyn provides a solution method by removing those problematic cells by several criteria. These criteria are itemized as follows.

- Instantaneous geometric strain
- Incremental geometric strain
- Effective plastic strain
- Timestep limit
- Material failure

It possible to choose either to remove or to keep the mass of an eroded cell by a single option. By keeping the eroded mass, the mass within the cell is distributed to the corner nodes of the cell. If the mass is retained by this way, conservation of inertia and spatial continuity of inertia are maintained [79]. However the compressive strength and internal energy are lost for both options.

If the cells around a particular node are eroded, the node becomes a free node (for the retain of inertia option). These nodes are still included to impact-slide logic in the solver and thus interact with both sides on the boundary. To the experiences of the author, these free nodes become problematic for 2-D axisymmetric and 3-D plane symmetric simulations by gathering around the symmetry axis or plane.

It must be noted that this erosion procedure does not represent any physical phenomena. Therefore care must be given when setting erosion criteria. The methodology used by the author assumes that the erosion parameter should be set in a range where it should not affect the results of the simulation. The only purpose for using erosion should be to increase the efficiency of the computation.

It was chosen to use instantaneous geometric strain in the simulations from the past experiences of the author. Westering [83] presented a study for the possibles problems that may arise from using this criterion. It was demonstrated that, when a unit cell is strained to its double length in one direction and slightly compressed in the perpendicular direction, it had almost zero instantaneous geometric strain due to the nature of the computations. Therefore it was decided to employ timestep erosion in the simulations where necessary in this study.

CHAPTER 5

MODELING AND SIMULATION OF BALLISTIC PENETRATION OF HARDENED STEEL PLATES

In this chapter, modeling and simulation studies are conducted based on the fundamentals given in Chapter 2 and 4. The study is mainly composed of two parts which deal with 2D and 3D simulations. The first assessment of material models are made by 2D simulations as it is a faster tool to get results compared to 3D simulations. Then the final assessment is made by 3D computations which can handle the physics of the process thoroughly.

5.1 2D Simulation Study

This part is dedicated to build material models for each hardness of the target material. An erosion parameter study and a mesh sensitivity analysis are conducted for the target and projectile. Then, sensitivity of J-C strength model results to model parameters is examined. Finally, the last part is dedicated to building strength models for each hardness and assessment of ballistic performances. For simplicity, only the hard steel core of the projectile is modeled for the erosion and mesh sensitivity studies. The assumption that only the hard core gives similar penetration results to the full projectile is also supported by Borvik et al [3]. Material model for the hard steel core is taken from the work by Bilici [84]. The equation of state and J-C strength model constants are given in Table 5.1.

Table 5.1: Material model parameters for 100Cr6

ρ [g/cm^3)	K [GPa]	T_R [K]	C_P [J/kg.K]	G [GPa]	T_M [K]
7.83	169	300	477	80	1793
A [MPa]	B [MPa]	n	C	m	ε_0 [s^{-1}]
2033	895	0.3	0.0095	1.03	1
K : Bulk Modulus, T_R : Reference Temperature, C_P : Specific Heat Capacity, G : Shear Modulus and T_M : Melting Temperature					

Erosion parameter study is conducted to verify a range of instantaneous geometrical strain value to make sure that the results are not affected by selected erosion parameters. Than a mesh convergence study is done to eliminate the mesh size effects. Target material model is chosen as the standard 4340 steel from the hydrocode's material library. Both of the parts are modeled with Lagrangian elements. A representative mesh is given in Figure5.1.

The target thickness is chosen as 10 mm to observe penetration. Diameter of the target is chosen as 150 mm to eliminate the edge effects. Velocity of the projectile is 782 m/s.

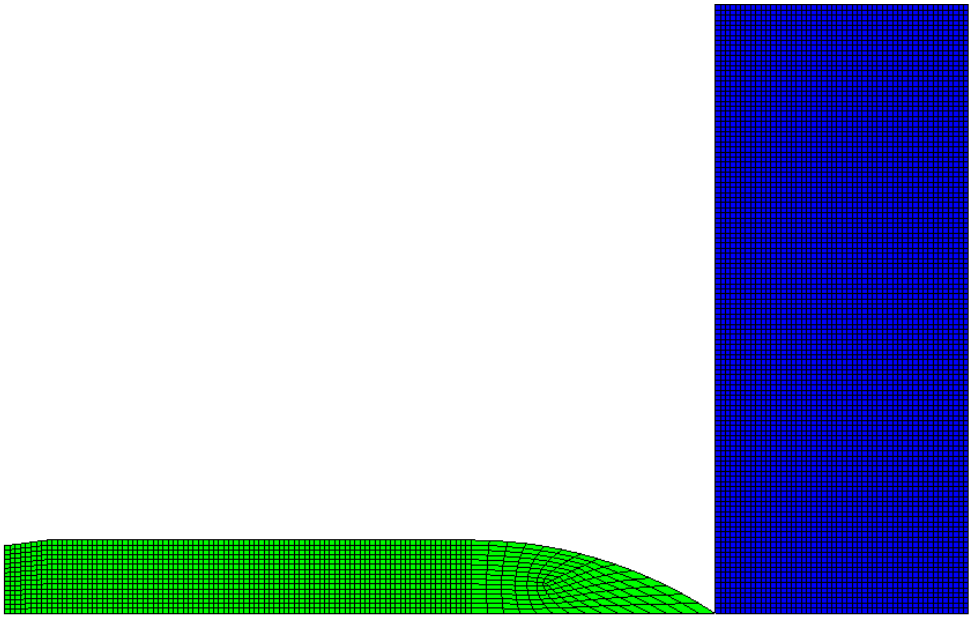

Figure 5.1: A representative mesh model for 2D axis-symmetric calculations (0.200 mm)

5.1.1 Erosion Parameter Study

Erosion studies are carried for three different mesh configurations. Selected mesh sizes are 0.500, 0.250 and 0.125 mm respectively. Residual velocity of the projectile after penetration is taken as the identifying parameter in this study. The simulation results are given in Table 5.2-5.4. Note that the residual velocities are in m/s.

Table 5.2: Residual velocity [m/s] for different erosion combinations for 0.500 mm mesh size

PE\TE*	0	1	2	2.5	3	4	6	8	10	15	20	30	50	100	200
0	err														
1		256													
2			512						494						
2.5				494					494						
3					494										
4						494									
6							494								
8								494							
10			512	494					494						
15										494					
20											494				
30												494			
50													494		
100														494	
200															494
* : PE = projectile erosion, TE : target erosion															

Table 5.3: Residual velocity [m/s] for different erosion combinations for 0.250 mm mesh size

PE\TE*	0	1	2	2,5	3	4	6	8	10
0	err								
1		574							
2			537						532
2,5				532					532
3					532				
4						532			
6							532		
8								532	
10			537	532					532
* : PE = projectile erosion, TE : target erosion									

Table 5.4: Residual velocity [m/s] for different erosion combinations for 0.125 mm mesh size

PE\TE*	0	1	2	2,5	3	4	6	8	10
0	err								
1									
2			550						
2,5				543					
3					536				
4						532			
6									
8									
10									532
* : PE = projectile erosion, TE : target erosion									

From the results depicted in Table 2-4; it is deduced that taking values greater or equal to 4.0 as instantaneous geometrical strain limit will be in the safe range regardless of the mesh size.

5.1.2 Mesh Convergence Study

Mesh convergence studies are carried out for 6 different mesh resolutions for the target and the projectile. Residual velocity results for refined (all uniform) mesh are given in Table 5.5.

Table 5.5: Residual velocities [m/s] for different mesh sizes

Mesh size [mm]	V_r [m/s]
0.100	524
0.125	532
0.200	535
0.250	532
0.400	510
0.500	494

It was seen that, as the mesh size for both parts is refined from 0.500 mm to 0.200 mm, the residual velocity is approaching to an asymptotical value. Further refinements beyond that mesh size gave smaller residual velocities, which was an unexpected result. It was evaluated that the iterative nature of the explicit nonlinear solution leads to accumulating round-off errors. As the mesh size is decreased, the number of cycles to complete the solution increases due to the decreased timestep value which is a function of the element size. Since the number of cycles increases, this accumulating errors due to the iterative nature of the solution

increases and starts to affect the solution significantly. Thus, 0.200 mm mesh size was found as the practical smallest mesh size that could be achieved. Hence, it is plausible to assume that 0.200 mm mesh size is the closest value to the asymptotic limit. Then it was decided to choose **0.250** mesh size with considerable savings in runtime in spite of a minute relative difference to the 0.200 mm mesh size.

It was further tried to optimize the mesh configuration for lower run times, for which, different mesh configurations for target are tried. The target mesh size was enlarged through the radius. The target mesh configurations which were called R1, R2, R3 and R4 are summarized in Figure 5.2.

It was seen that R1, R2 and R3 gave the same residual velocity results with the uniform mesh configuration. Therefore it was fruitful to use target mesh configuration R4 in terms of smaller run time.

Further, the effect of using different mesh sizes for the projectile and the target were studied. As the aim of the study is to examine the target behavior, using smaller mesh size for target and larger mesh size for the projectile would be better. The residual velocities were compared with the uniform mesh configurations. The results are given in Table 5.6.

Table 5.6: Results of different mesh sizes for the projectile and target

Projectile mesh	Target mesh	Target configuration	V_r [m/s]	Uniform Mesh [m/s]
0.250	0.100	R3	538	524
0.250	0.125	R3	540	532
0.250	0.200	R3	536	535
0.250	0.200	R4	535	535
0.250	0.250	R2	532	532

It was seen that the optimum mesh size ratio of projectile mesh size to the target mesh size would be **1.25** mm; beyond which will give different results from the uniform mesh configuration.

5.1.3 J-C Model Sensitivity Studies

This part is based on the study presented by the author [28].

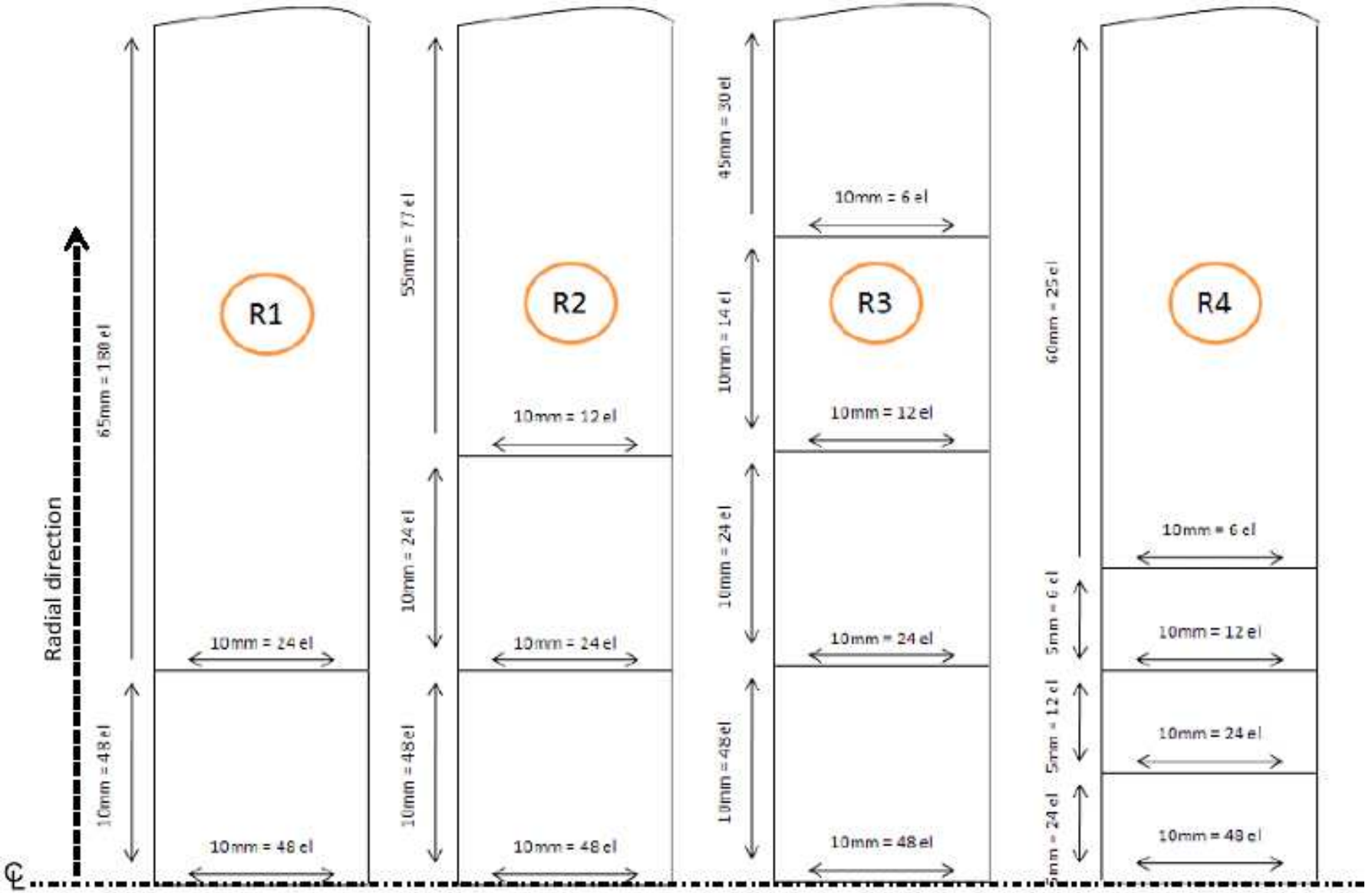

Figure 5.2: R1-R4 representation for 0.200 mm target mesh size (0.200-r_x). Total thickness of target is 10 mm

Material model selection is important in solving ballistic penetration problems with the help of numerical simulations. It was evaluated that it is necessary to analyze the influence of material model constants to the strength model results to have an insight in to the material model and ballistic penetration phenomena. In this study, J-C strength model parameters derived from SHPB (Split Hopkinson Pressure Bar) tests are taken as basis and the effects of changing this parameters on material model results are discussed. The sensitivity of material model results to material model constants were examined.

As it was mentioned in Thermal Instabilities (Section 2.3), adiabatic heating occurs in material as a result of high strain rates. There is no time for heat transfer. Therefore, the strength of the material decreases due to heating. The amount of temperature rise can be found by Eq. 5.1 [27].

$$dT = \beta \frac{1}{\rho C_P} \sigma(\varepsilon) d\varepsilon \tag{5.1}$$

Here, β denotes the ratio of mechanical work that is converted to heat; which usually has a value between 0.9-1.0.

In simulations, the material model gives similar results with the real tests up to instability strain values. Beyond this strain, special care must be given to compare the simulations with test result as there may occur instabilities. The instability strain is defined by Eq. 5.2.

$$d\sigma/d\varepsilon = 0 \tag{5.2}$$

It was seen from the previous simulations that the strain rates in target material ranges from 1000 to 10000 s^{-1} and most of the deforming region possessed strain rates about 1000 s^{-1}. Stress - strain graph of the target (HRC39.5, for which material constants will be given in next section) and projectile material for strain rate of 1000 s^{-1} and adiabatic heating conditions is given in Figure 5.3. It was found that due to adiabatic heating, the target and projectile material reached 479 and 597 K, respectively.

The instability strains for the different tempers of the target material are plotted in Figure 5.4.

It was seen from Figure 5.4 that the instability strain decreases with the increasing hardness.

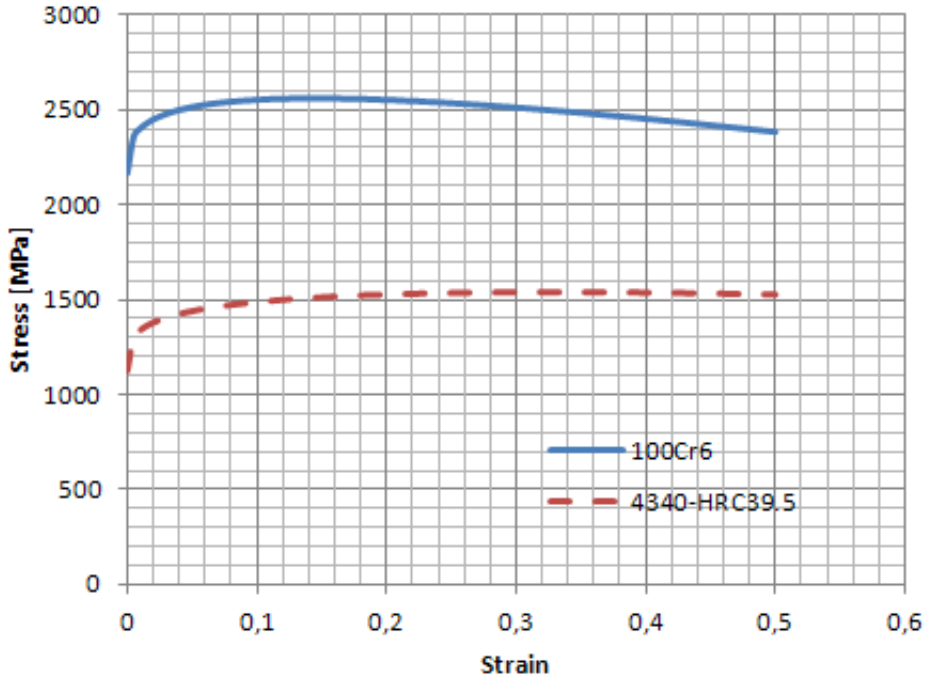

Figure 5.3: Adiabatic stress - strain graph of target and projectile material for $1000s^{-1}$

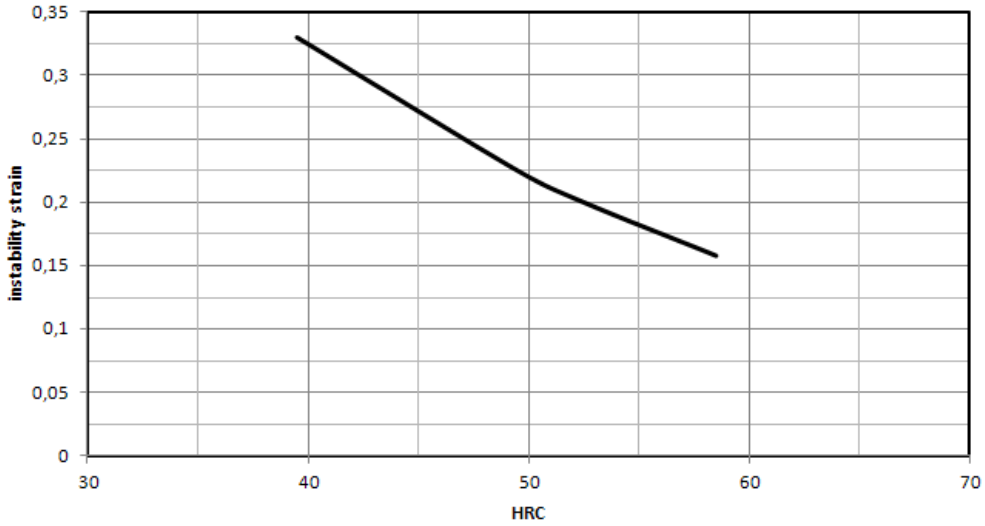

Figure 5.4: Influence of temper on instability strain

The first multiplier of the J-C strength model defines the quasi-static stress - strain response of the material. The material constant A is the yield strength of the material in zero strain and it is easy to determine this constant by a tensile test. B is the strain hardening constant and an increase of this constant results in an upper shift of the curves given in Figure 5.3, and it is also easy to determine this material constant.

The last material constant for strain hardening is the strain hardening exponent n, which defines the shape of the strain hardening curve. The resulting strain hardening curves of different values of n in the range 0.2-0.6 for the target material are depicted in Figure 5.5.

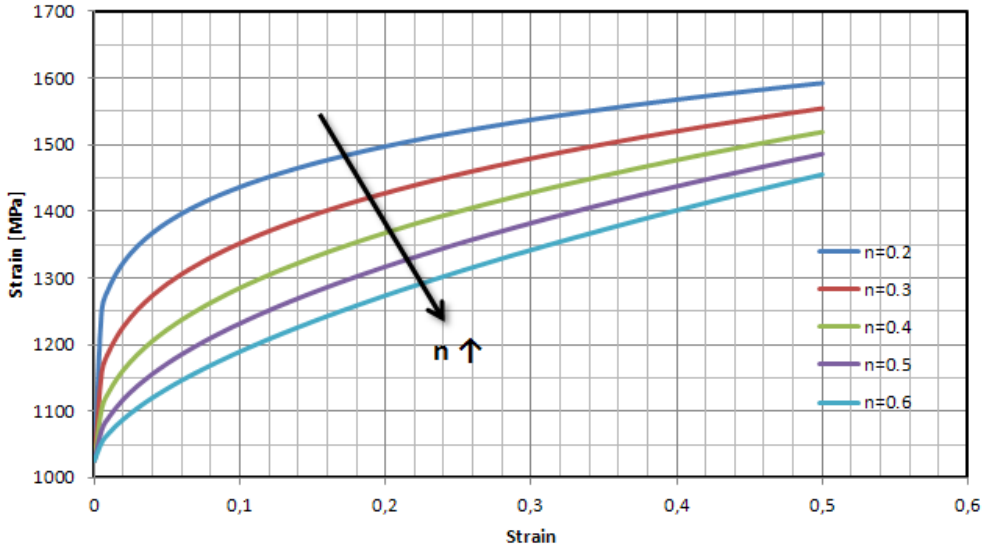

Figure 5.5: Strain hardening curves for the target material for different n values

From the Figure 5.5, it can be deduced that increasing the value of n results in a lower strength of the material. Further it can be said that a lower value of this constant means a fast strengthening of the target material, which means a lower penetration. Subsequent simulations verified this approach.

The second multiplier of the J-C strength model is defined as KC and resulting KC plot for different values of strain rate hardening parameter C are depicted in Figure 5.6.

From Figure 5.6, it can be seen that, increasing the value of C from 0.014 to 0.14 increased the value of KC from 1.1 to 2.0 for a typical value of strain rate for ballistic problems as 1000 s^{-1}. This implies that, changes in C in the order of 1e-3 does not significantly affect the strain

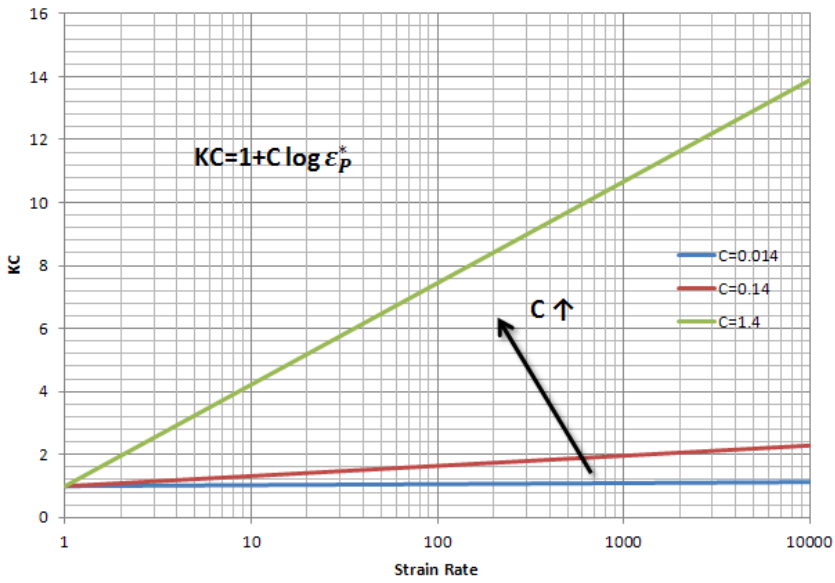

Figure 5.6: KC as a inciting of strain rate for different values of C

rate hardening multiplier.

The third multiplier of the J-C strength model which deals with the temperature softening is denoted by KT. Resulting KT curves for different values of the temperature softening parameter ”m” are plotted in Figure 5.7.

As it can be seen from Figure 5.7, the material possesses a linear softening trend for a unity value of m. As m is increased, the temperature softening decreases. For steel, this value takes values between 0.5 and 1.5 from the experience of the author.

The next step is the sensitivity study for material parameters. These sensitivities are examined as a function of strain, strain rate and temperature. The study is based on the work of Saltelli [85], and was made for the target material at 39.5 HRC.

The sensitivities of the parameters were related to derivative of the J-C strength model with respect to each parameters and the resulting value was multiplied with the corresponding parameter to plot the sensitivities in the same scale. Sensitivities of each parameter with respect to changing strain and homologous temperature were plotted in Figure 5.8 and Figure 5.9 respectively.

As it can be seen from Figure 5.8, which is plotted for strain rate of $1s^{-1}$, the sensitivity of

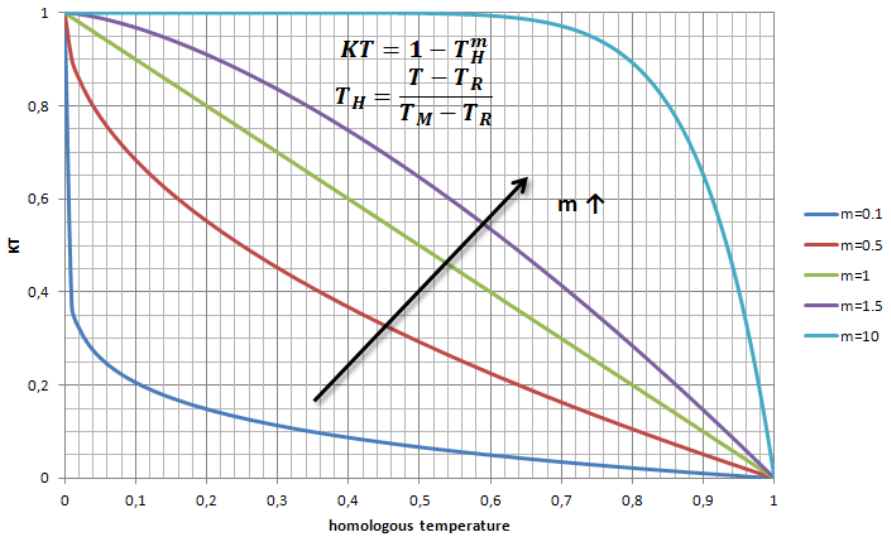

Figure 5.7: KT as a function of homologous temperature for different values of m

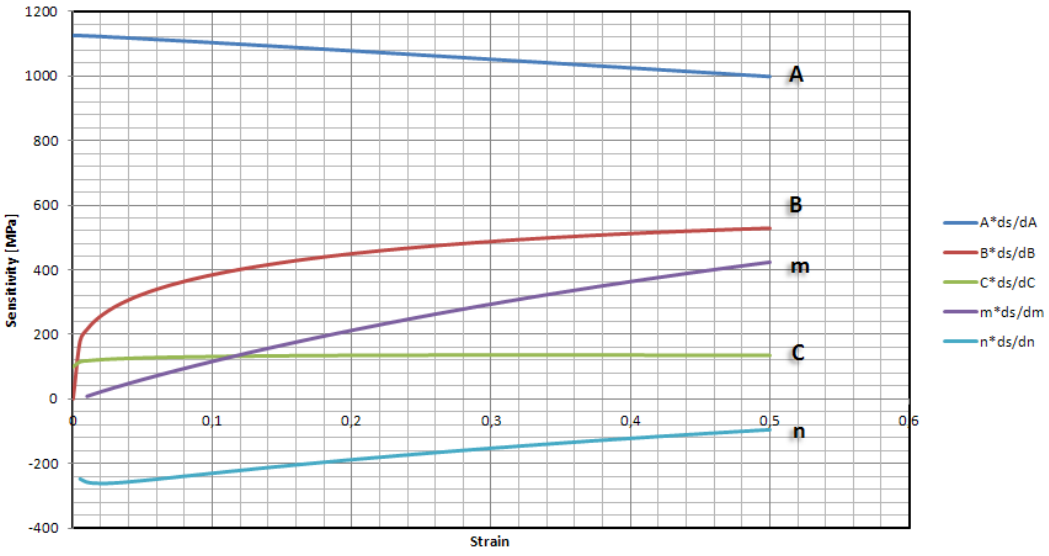

Figure 5.8: Sensitivity of the strength model parameters with respect to strain (for $1s^{-}1$ strain rate)

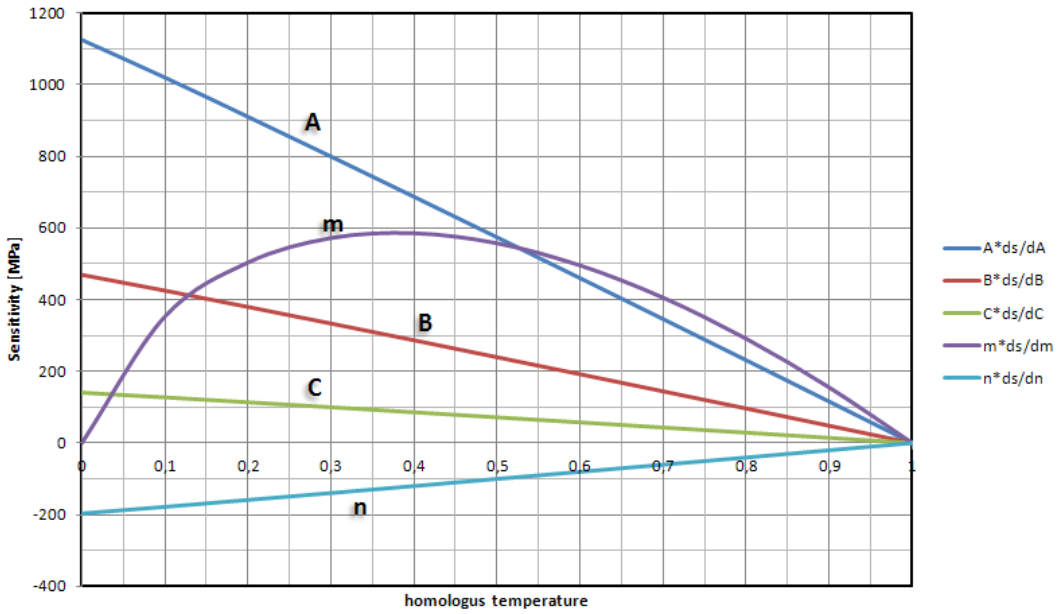

Figure 5.9: Sensitivity of the strength model parameters with respect to homologous temperature (for 1000s⁻1 strain rate and 0.2 strain)

m increasing with increasing strain as a result of adiabatic heating. There is no change in sensitivity of C as there is no change in strain rate. Negative sensitivity of n means that the stress will decrease with an increase in this parameter, as was also depicted in Figure 5.5. With increasing strain, the sensitivity towards the parameters n and A will decrease, whereas m and B will increase.

It was found that there is hardly any change in sensitivities of parameters for changing strain rate.

Figure 5.9 was plotted for 1000 s^{-1} and 0.2 strain. As it can be seen that, all parameters (except m) possess decreasing sensitivity with increasing homologous temperature. Only m possesses low sensitivity for lower temperatures, then and increasing sensitivity up to 0.39 homologous temperature.

5.1.4 Model Selection for Target

This part of the study presents the data about AISI 4340 steel found from the literature for different tempers.

The equation of state model was based on the parameters given by Steinberg [86], and it was assumed that the EOS will be the same for each hardness. The shock EOS constants for the target material are given in Table 5.7.

Table 5.7: EOS for AISI 4340 for all tempers

ρ [g/cm^3]	Γ	C0 [m/s]	S	T_R	C_P
7.83	1.67	4578	1.33	293	477

Banerjee [87] suggested J-C strength model constants for different tempers of the target material. The relation of value of A to the hardness (HRC) of the material was given as A = EXP(A1$*$HRC + A2)(MPa) where A1 = 0.0355 ln(MPa), A2 = 5.5312 ln(MPa). The ratio B/A which is 0.6339 was assumed to be constant for all tempers. The other parameters n, C, ε_0 and m were stated as 0.26, 0.014, 1 s^{-1} and 1.03 respectively. A plot of A and B with respect to varying hardness (HRC) is depicted in Figure 5.10.

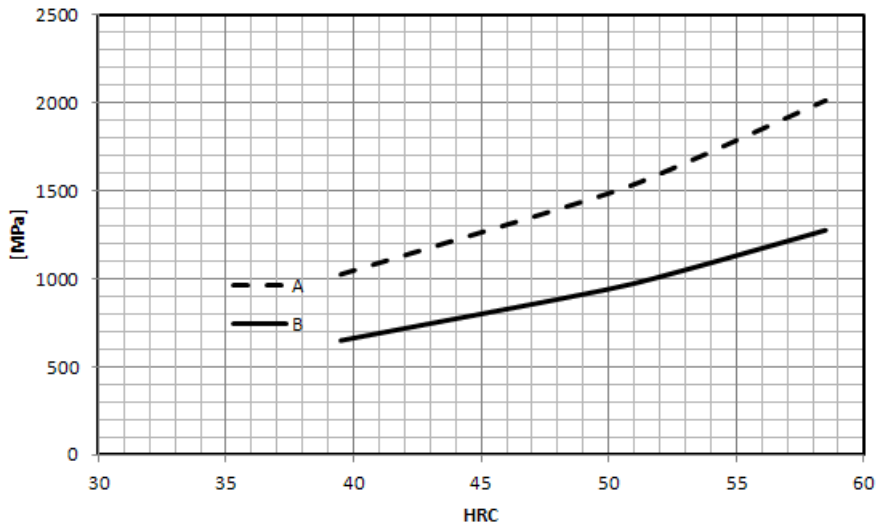

Figure 5.10: Variation A and B with respect to hardness (HRC)

Lee et al [88] presented the variation of strain hardening exponent n and reduction in area for different tempers of the target material. Plots of change in n and failure strain with respect to varying hardness based on his results are given in Figure 5.11 and 5.12.

Tanimura et al [89] worked on the strain rate sensitivity for different hardness of the target material. A plot of changing strain rate sensitivity parameter C with respect to change in

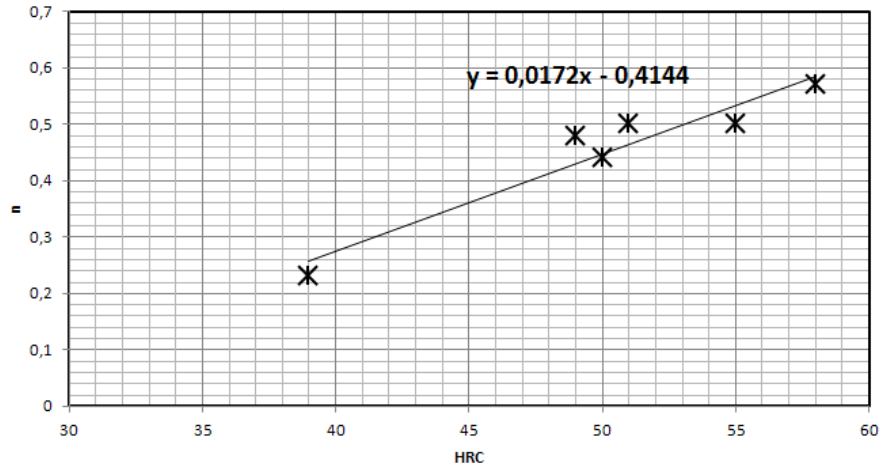

Figure 5.11: Change in n for varying hardness (HRC)

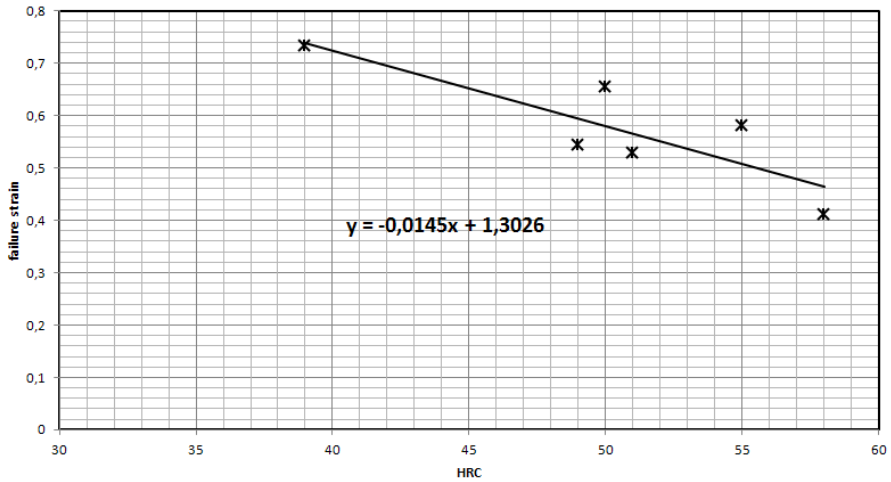

Figure 5.12: Change in failure strain for varying hardness (HRC)

hardness is given in Figure 5.13.

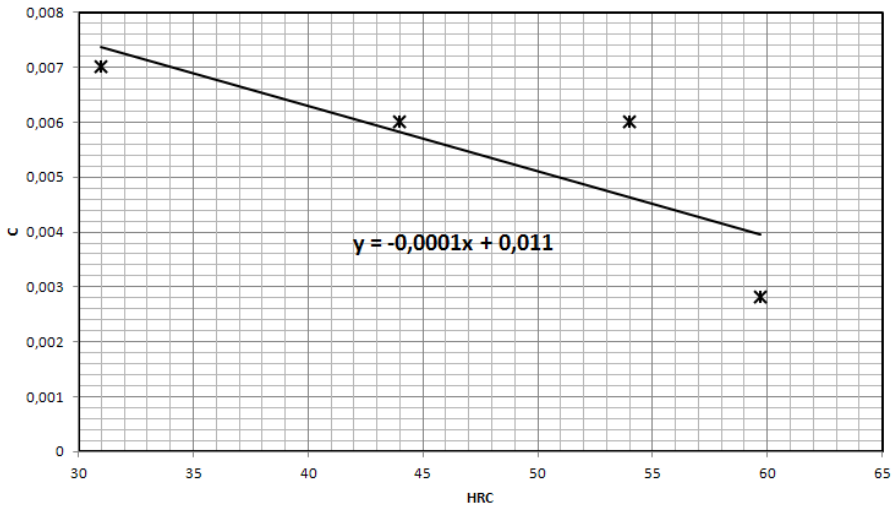

Figure 5.13: Change in C for varying hardness (HRC)

The assumption that the same penetration will be achieved by the full projectile (with lead and cartridge) and only the hard steel core was checked. The residual velocity of full projectile was found 4 % lower than the residual velocity of the hard steel core. This is a minor difference, and thus the later model was selected for further studies.

It was chosen to use 0.250 mm mesh size for projectile and 0.200-r4 for target mesh from the mesh sensitivity studies.

The effect of using failure model was studied. Due to lack of experimental data, J-C failure model was not constructed for the target material. The use of constant plastic strain failure was assessed by two simulations. Figure 5.14 depicts the results of these simulations.

It was seen from Figure 5.14 that using constant plastic failure strain as a failure model resulted in erroneous elements. Therefore it was decided not use a failure model.

Simulations with strength models derived from literature (Figure 5.10- 5.13) were conducted. The matrix of simulations and J-C strength model coefficients used were summarized in Table 5.8 and 5.9. The target thicknesses were 7- 14 mm with 1 mm increments. The projectile model is 100Cr6 and simulations for a rigid projectile are also performed to observe the difference between the results.

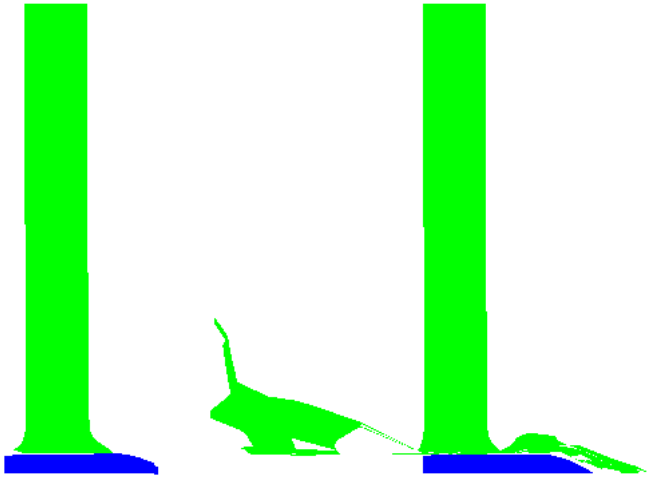

Figure 5.14: Simulation results for no failure and constant plastic failure strain model

Table 5.8: Simulation matrix for the material model selection

Model #	Description of target model	Projectile model	
		100Cr6	Rigid
1	Banerjee	1A-1D	1AR-1DR
2	Banerjee + n	2A-2D	2AR-2DR
3	Banerjee + C	3A-3D	3AR-3DR
4	Banerjee + n +C	4A-4D	4AR-4DR
1-4: Target strength model, A-D: Target hardness (39.5, 49.5, 52.5, 58.5 resp.), R: rigid			

Table 5.9: J-C model parameters for the target material

J-C	A (HRC 39.5)				B (HRC 49.5)				C (HRC 52.5)				D (HRC 58.5)			
	1	2	3	4	1	2	3	4	1	2	3	4	1	2	3	4
A	1026 MPa				1463 MPa				1628 MPa				2014 MPa			
B	650 MPa				928 MPa				1032 MPa				1277 MPa			
n	0.260	0.256	0.260	0.256	0.260	0.428	0.260	0.428	0.260	0.463	0.260	0.463	0.260	0.583	0.260	0.583
C	0.014	0.014	0.007	0.007	0.014	0.014	0.006	0.006	0.014	0.014	0.006	0.006	0.014	0.014	0.005	0.005
m	1.03				1.03				1.03				1.03			

The residual velocity results for the simulations that are depicted in Table 5.8 are plotted in Figure 5.15- 5.22.

From Figure 5.15- 5.22, it is seen that there is a considerable increase between the residual velocity results of 100Cr6 and rigid projectile for an increasing hardness. For HRC 52.5 and

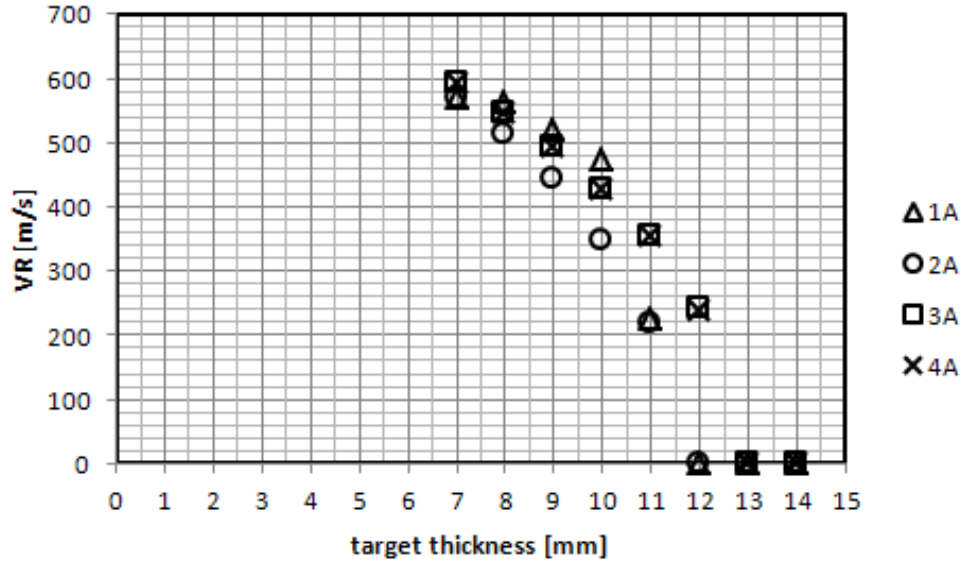

Figure 5.15: Simulation results for HRC 39.5 (100Cr6 projectile)

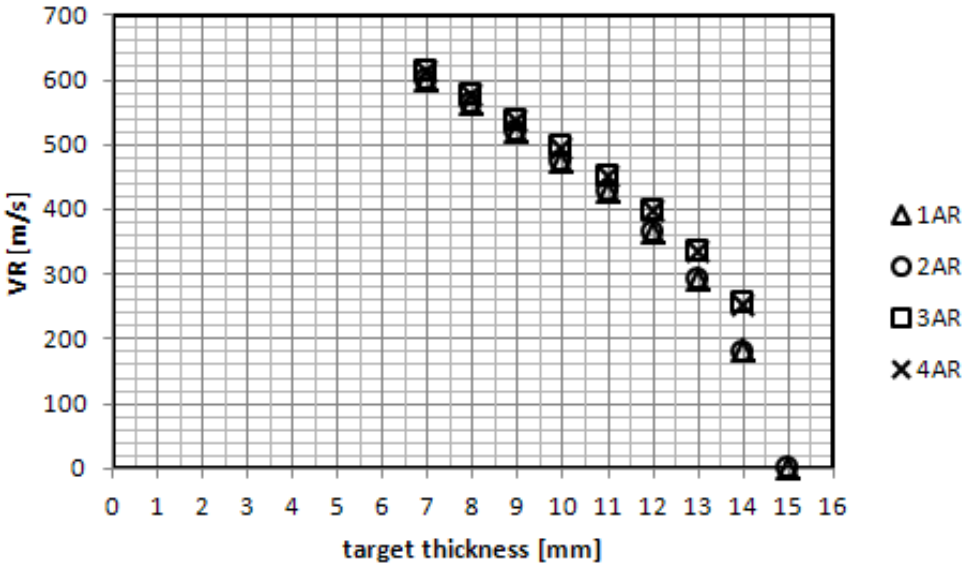

Figure 5.16: Simulation results for HRC 39.5 (rigid projectile)

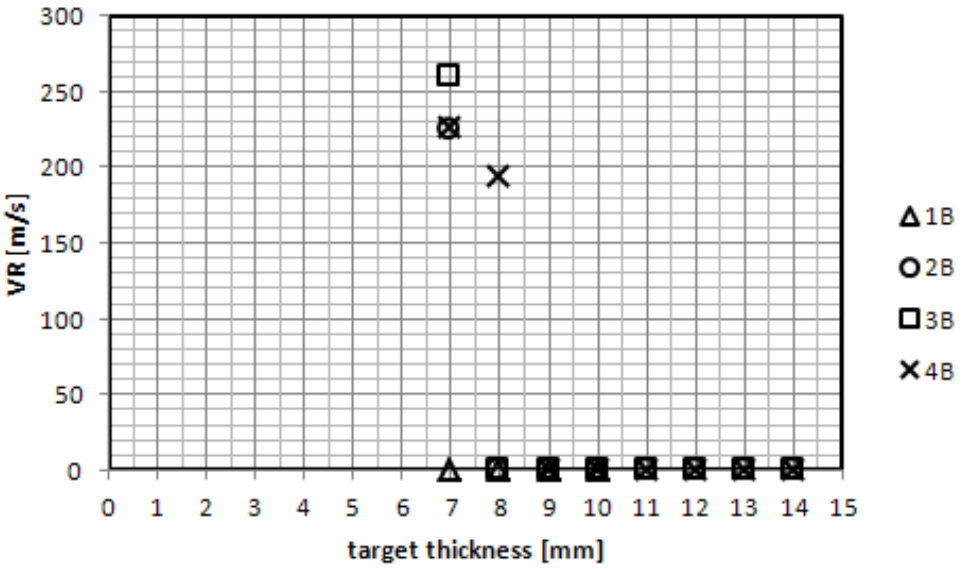

Figure 5.17: Simulation results for HRC 49.5 (100Cr6 projectile)

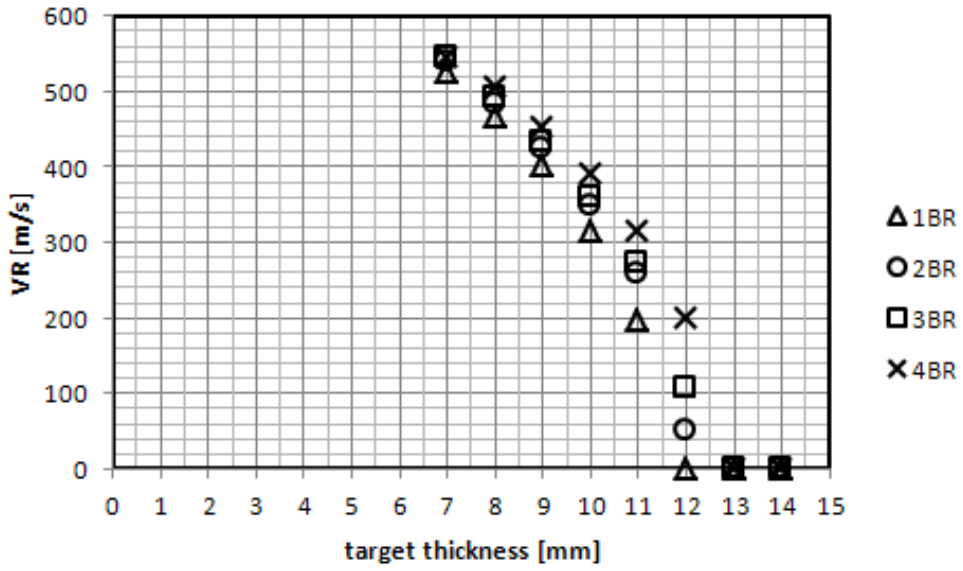

Figure 5.18: Simulation results for HRC 49.5 (rigid projectile)

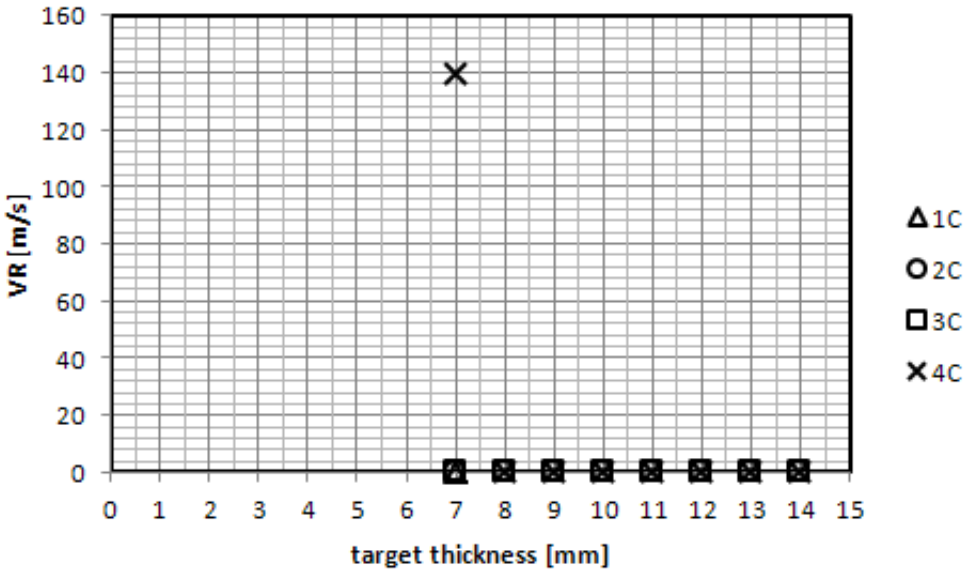

Figure 5.19: Simulation results for HRC 52.5 (100Cr6 projectile)

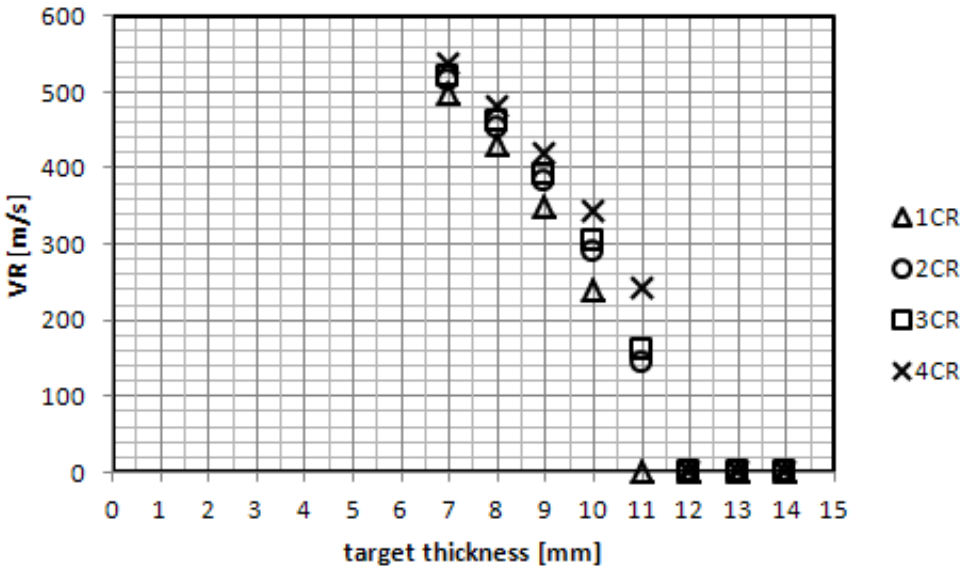

Figure 5.20: Simulation results for HRC 52.5 (rigid projectile)

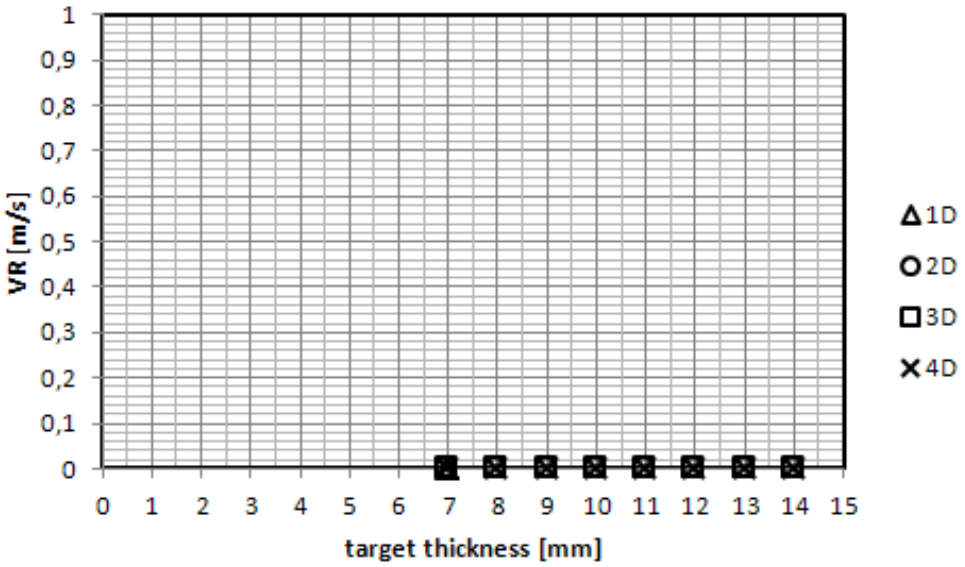

Figure 5.21: Simulation results for HRC 58.5 (100Cr6 projectile)

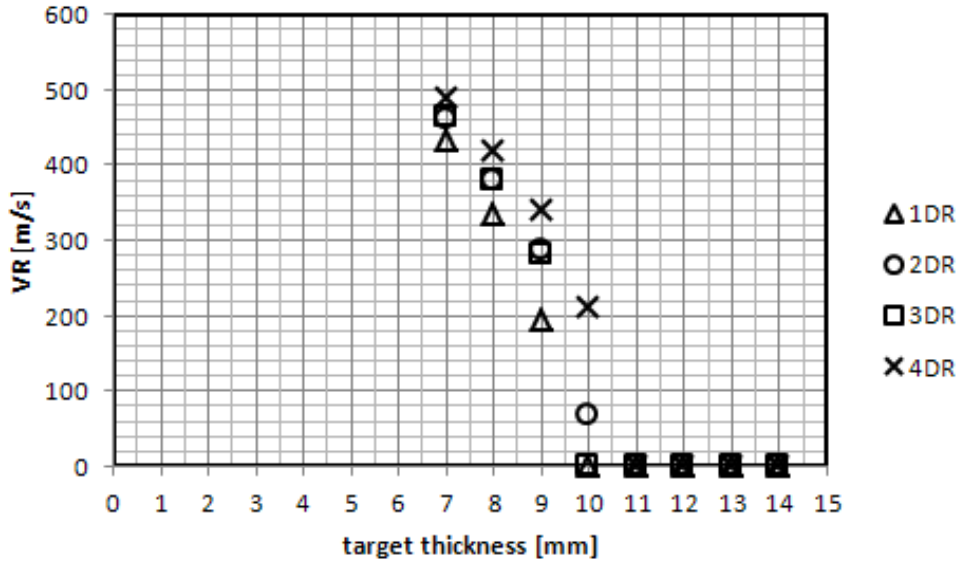

Figure 5.22: Simulation results for HRC 58.5 (rigid projectile)

HRC 58.5, there is no penetration (except 7mm 4C target) for all thicknesses.

When the simulations of material model groups of 1 and 2 are compared; it is seen that the residual velocity increases for 2, which is an expected result as n is increased, taking sensitivity of J-C strength model into consideration. The same situation applies for the comparison of 1 and 3, as C is decreased. A combined effect is seen for material model group 4, which yields the highest residual velocity results.

Auxiliary simulations for a target hardness of HRC 59.7 AISI 4340 steel are also conducted. The J-C strength and failure model is taken from the thesis study of Lee [90]. Corresponding model parameters are given in Table 5.10 and the material model is named as ”E”. From the simulations, it was seen that 100Cr6 penetration could not penetrate any of the target thicknesses. The comparison of simulation results of E against rigid projectile is given in Figure 5.23.

Table 5.10: J-C strength and failure model parameters for HRC 59.7 [95]

A [MPa]	B [MPa]	n	C	m	D1	D2	D3	D4	D5
2100	1750	0.65	0.0028	0.75	-0.8	2.1	-0.5	0.002	0.61

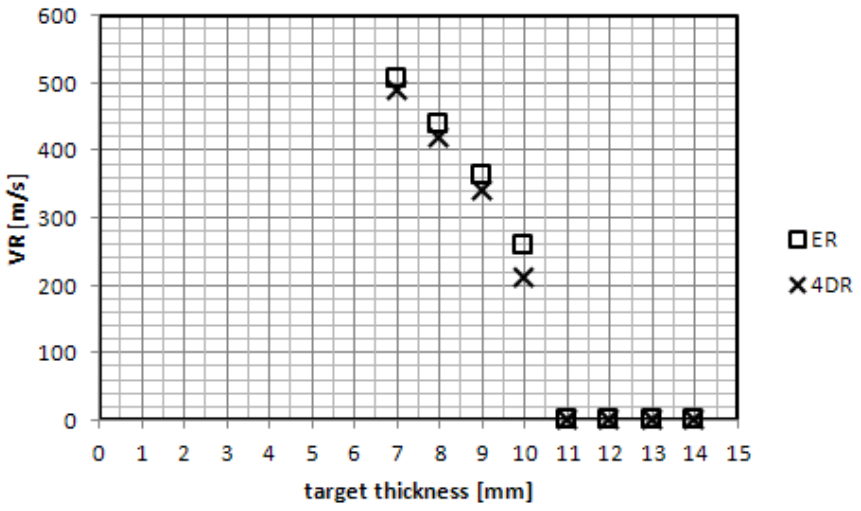

Figure 5.23: Comparison of simulation results for ER and 4DR

From Figure 5.23, it is seen that the simulation results for ER and 4DR are quite in agreement in terms of residual velocities. Assuming that material model of E is calibrated from SHPB tests (there is no justification for the model in the thesis of Lee [90]), it can be deduced that

material model group 4 combined with a rigid projectile gives the closest results to the real case. Therefore target model group 4 is chosen. Residual velocity results for the material group 4 against rigid projectile are plotted in Figure 5.24.

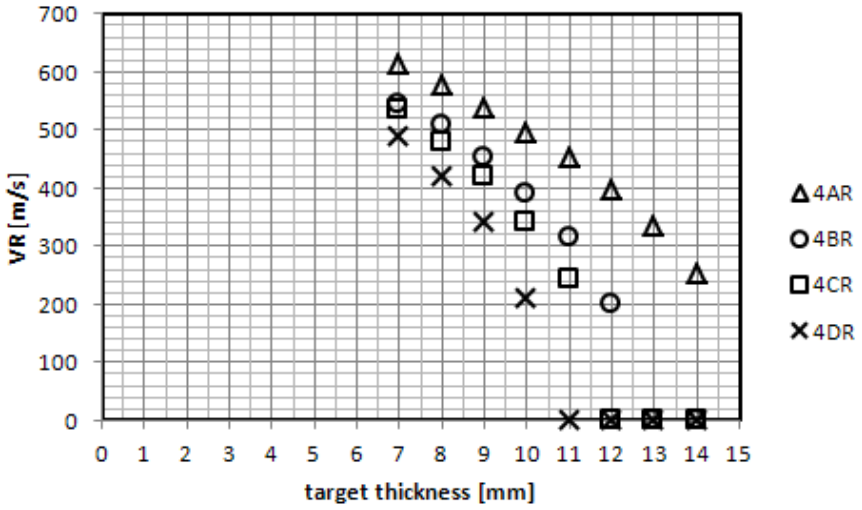

Figure 5.24: Comparison of residual velocities of 4AR-4DR

From Figure 5.24, it can be seen that there is a decrease in ballistic limit thickness for the increase in target hardness. This seems plausible as the target strength is directly proportional to hardness.

5.2 3D Simulation Study

2D simulations gave results in terms of residual velocity and ballistic limit thickness. However, there is a need in 3D modeling to observe the complete physics of the interaction between the projectile and the target. Erosion and mesh convergence studies were conducted to assure that the simulations are in the range where the significance of these parameters is minimal. Then, the simulations of various thicknesses for each temper were performed. A representative mesh model for 3D simulation studies is given in Figure 5.25

5.2.1 Erosion Parameter Study

It was found from 2D simulations that the safe range (where the simulations are not affected by the selected erosion criteria) is not a function of mesh size. Thus, it is plausible to assume

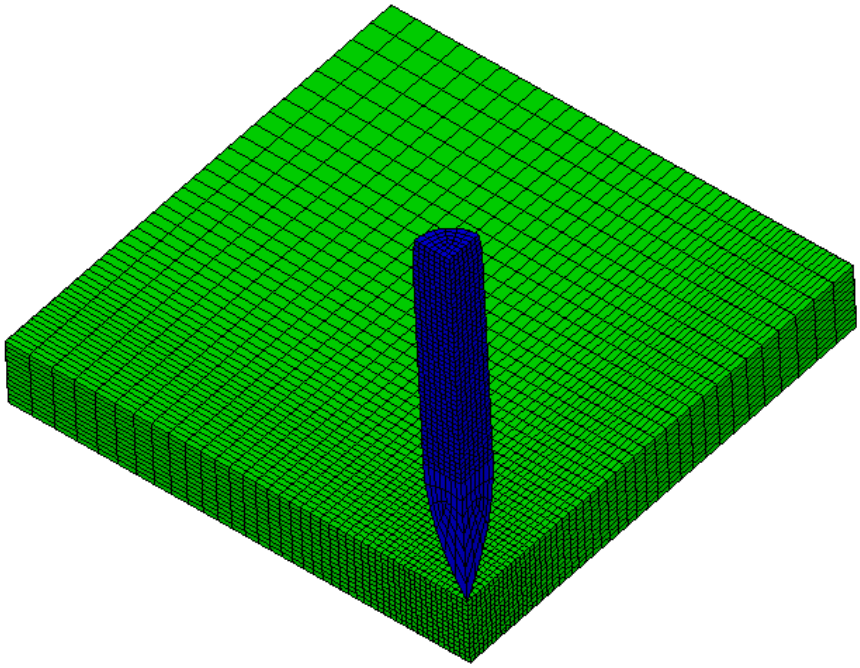

Figure 5.25: A representative 3D mesh model (thickness of the target is 5 mm and mesh size is 0.400 mm, the model is a quarter model with 2 planes of symmetry)

that the same applies to 3D simulations.

The selected mesh size was 0.5 mm both for the target and the projectile, and it was kept uniform around the model. The projectile was modeled as rigid and the target was modeled with AISI 4340 steel from the hydrocode library. The instantaneous geometrical strain was varied between 0.5 and 3.0 by 0.5 increments. The simulation results are given in Table 5.11. It must be noted that the residual velocity was taken as the identifying parameter and all the results are interpreted in m/s.

Table 5.11: 3D erosion matrix

PE\TE	0.5	1.0	1.5	2.0	2.5	3.0
0.5	692					
1.0		673				
1.5			651			
2.0				645		
2.5					645	
3.0						645

Thus, from Table 5.11, it can be seen that adjusting values greater or equal to 2.0 for the

instantaneous geometrical strain will minimize the erosion effects on the simulations.

5.2.2 Mesh Convergence Study

Mesh convergence study was performed to identify the mesh dependence of simulation results. The mesh sizes of the projectile and the target were varied between 0.5 mm and 0.2 mm. The thickness of the target was 5 mm and it was modeled with AISI 4340 from the hydrocode material library. The simulation results in terms of residual velocities and average runtimes per microseconds of simulation are plotted in Figure 5.26- 5.27.

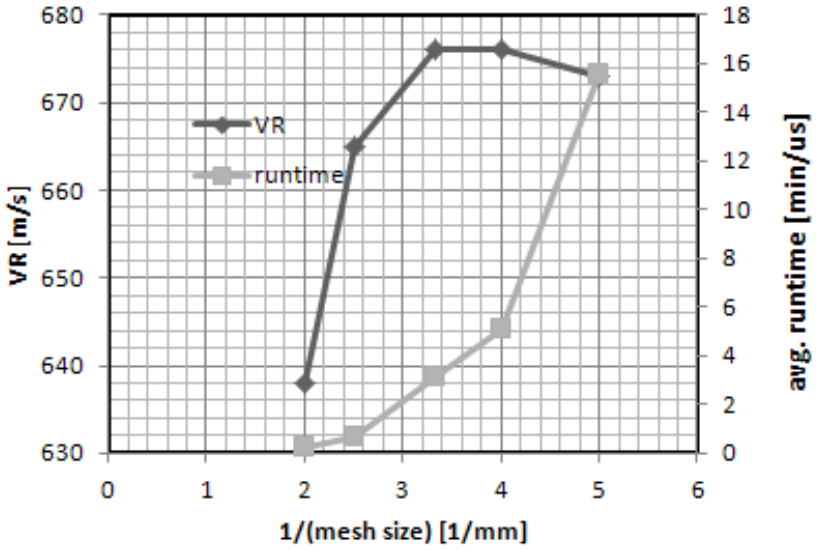

Figure 5.26: Residual velocities and runtimes per microseconds for different mesh sizes for target and projectile

It can be seen from Figure 5.26 that, the residual velocity of the projectile possesses an asymptotic behavior up to 0.3 mm element size. After corresponding mesh size, the residual velocity decreases unexpectedly, which was again attributed to the iterative nature of the explicit simulations (See Section 5.1.2). Thus it is plauseible to assume that 0.300 mm mesh configuration gives closest results to the asymptotic value. Having a minute relative difference with respect to the 0.300 mm mesh size (1.7 %), 0.400 mm mesh was chosen thanks to the considerable savings in runtime.

The results depicted in Figure 5.27 possess no asymptotic behavior. The results are the same for 0.5 and 0.4 mm, however some deviation occurs from the uniform meshing with further

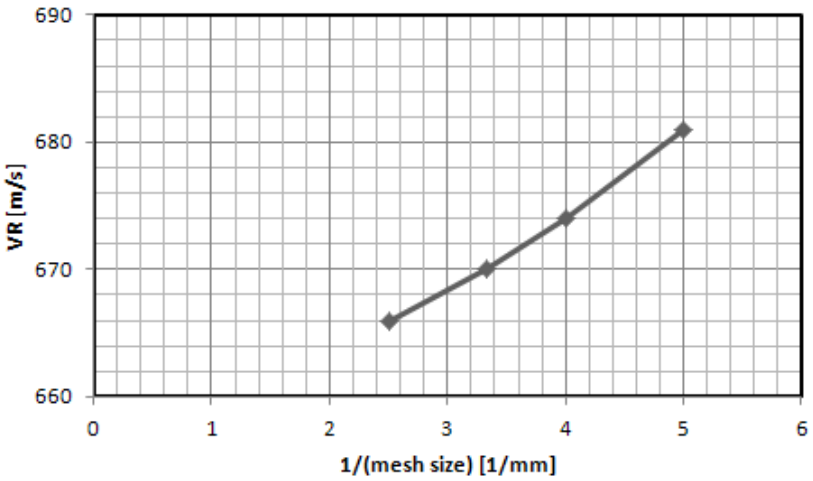

Figure 5.27: Residual velocities for changing target mesh size (projectile mesh size was kept constant as 0.5 mm)

refinements. Thus the selection of 0.4 mm mesh size enables the usage of higher element size for the projectile.

5.2.3 Ballistic Limit Thickness for Each Temper

3D numerical simulations are performed to identify the ballistic limit thickness for each hardness. 2 plane symmetry was used in the simulations. The projectile was modeled as rigid and the target was modeled with the 4th material models (4AR-4DR) as shown in 2D simulations. Target thickness was ranged between 7 and 14 mm. Mesh models are converted to unstructured elements to save run time [79]. Also the contact model was selected as trajectory contact, which saves run time (as the timestep is not effected by contact) and guarantees energy conservation [79]. The inertia of eroded nodes were kept. The results of simulations are depicted in Figure 5.28.

From Figure 5.28, it was seen that the ballistic limit thickness for each temper is 14, 12, 11 and 10 mm, which yields an almost linear decrease of limit thickness with an increase in target hardness. This result is depicted in Figure 5.29. It must be noted that this behavior may not be seen in real case for all tempers as it may be the case that too much hardness may result in a brittle target, which yields a low impact toughness and hence the target may behave as a ceramic.

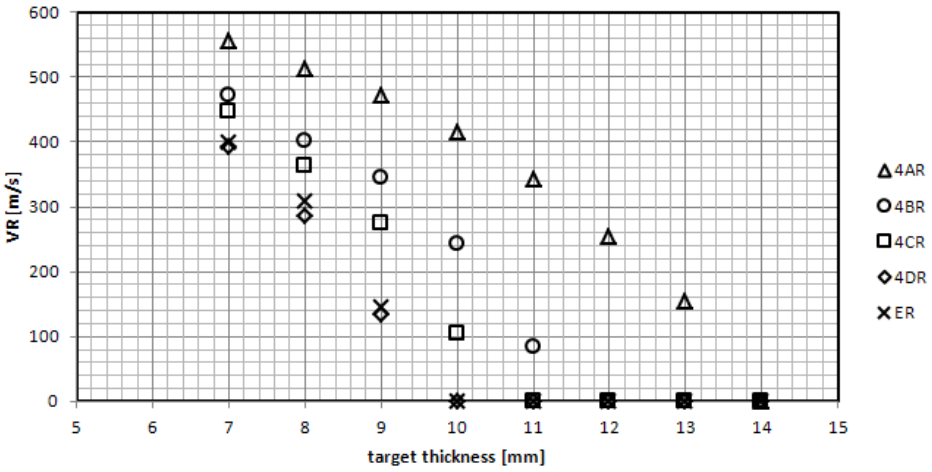

Figure 5.28: Residual velocity results for each temper for varying target thickness

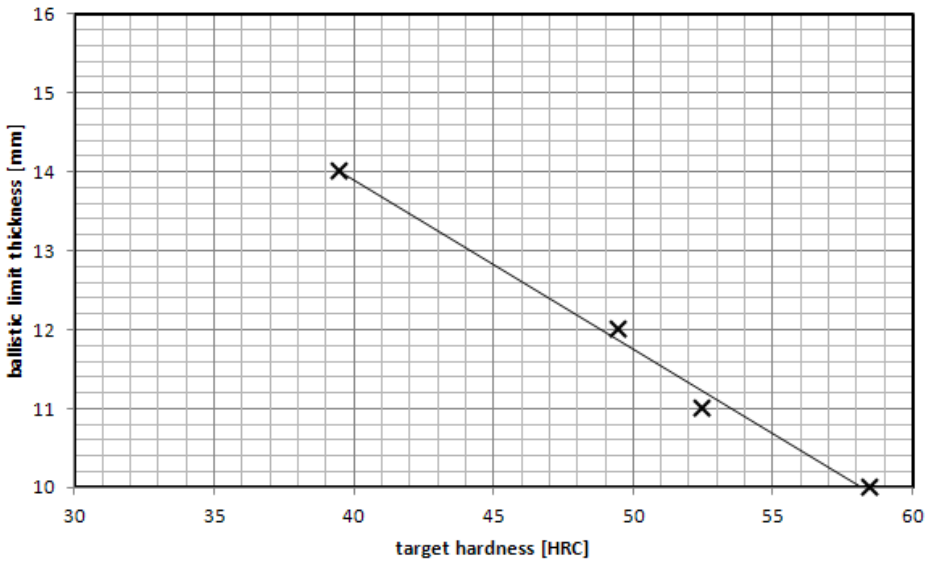

Figure 5.29: Ballistic limit thickness as a function of target hardness

Furthermore, the selection of ”retain the inertia” option in the hydrocode is investigated by performing simulations for the high thicknesses that are not penetrated. The simulation results are given in Table 5.12.

Table 5.12: Comparison of the selection of residual velocities [m/s] for ”retain the inertia” option

Model	4A	4B	4C	4D	E
Thickness [mm]	13	11	10	9	9
Keep inertia	153	84	105	133	144
Delete inertia	109	85	121	182	139

Simulation results given in Table 5.12 suggest that the ballistic limit thickness is not affected by the selection of ”retain the inertia” option. However, there is a difference in terms of residual velocity. For 4A and E, deleting the eroded inertia gave a lesser residual velocity, whereas for 4B, 4C, 4D and E a higher residual velocity is observed. This situation is attributed to the accumulating of eroded nodes into the planes of symmetry, which may attract instabilities. It is evaluated that this situation will not be observed for full model runs (no symmetry).

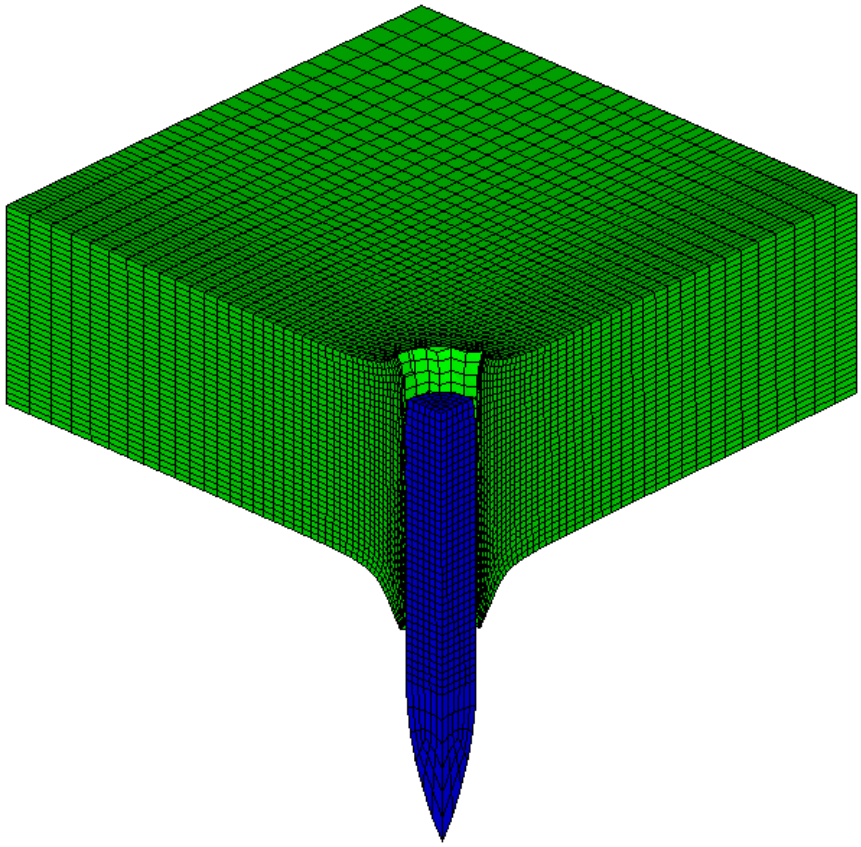

Figure 5.30: A sample simulation result from 3D simulation studies (HRC 39.5 target with 13 mm thickness, plate after perforation)

CHAPTER 6

EXPERIMENTS AND COMPARISON OF RESULTS

This chapter is dedicated to experimental part of the thesis study. In the first part, experimental setup is briefly explained. Then experimental results are given and in the last part, comparison of the experimental results with the numerical and analytical results are provided.

6.1 Experimental Procedure

The AISI 4340 samples were procured from the market and then heat treated to varying hardness (39.5, 49.5, 52.5 and 58.5 HRC). Five different areal densities were selected (as 55, 70, 85, 100 and 115 kg/m^2) which correspond to 7.2, 9, 10.8, 12.7 and 14.4 mm thickness and the samples were machined to those corresponding thicknesses by bandsaw followed by milling. The diameters of the samples were 70 mm.

Ballistic tests were performed at laboratory of Silahsan A.Ş. at Kırıkkale. The test setup is illustrated in Figure 6.1. The target plates were placed 15 m away from the barrel of the riffle. 2 velocity measurement systems were placed in front and behind the target plate fixture to measure the incident and residual projectile velocities.

Regarding the test setup in Figure 6.1, 7.62 AP projectiles were fired onto targets. 5 samples were tested for each thickness, which amounts to 25 shots for each hardness and a total of 100 shots. Incident and residual velocities of the projectile were recorded.

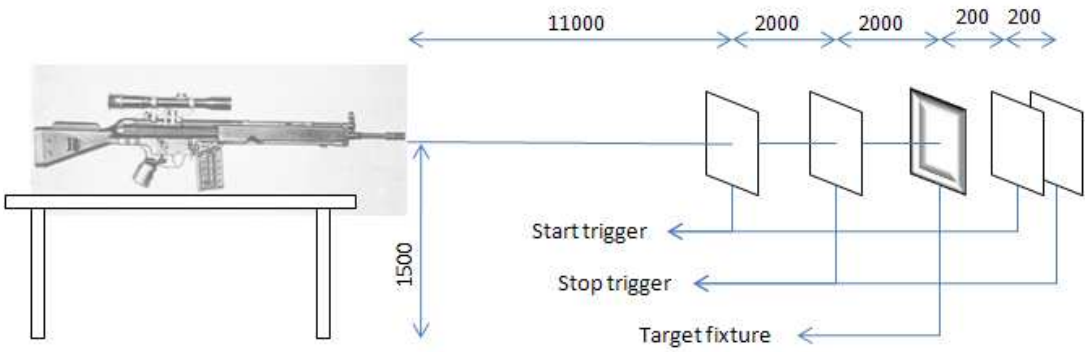

Figure 6.1: Setup for ballistic tests (dimensions in mm)

6.2 Experimental Results

This part of the chapter is dedicated to macro investigation of test samples after each shot. Recorded incident velocity of the projectile was 782 ± 5.4 m/s.

The samples of HRC 39.5 were perforated in all shots except for the case of 4th areal density targets, of which 3 samples were not perforated in 5 samples. Furthermore, the samples of 5th areal density were just perforated by the projectile and the projectile was struck in target or shuttered. Images of the test samples are given in Figure 6.2 for all target thicknesses. Figure 6.3 depicts the corresponding specimens for which the projectile was struck in the target.

For the hardness of HRC 49.5, ductile penetration was seen for all targets at the 1st areal density. None of the targets at the 2nd areal density were perforated, however, deep cracks were observed at the back of the plates. As the thickness of the targets were increased, crack formation and the number of cracks were seen to decrease and for the 5th areal density, no cracks were observed at all. Figure 6.4 and 6.5 illustrates the front and the back faces of each target.

For the hardness of HRC 52.5, all the samples of the 1st and 2nd areal density were perforated. The samples from the 3rd areal density provided ballistic protection (i.e. not perforated). The samples of the first two areal densities were shuttered and the samples of the 3rd areal density possessed several cracks on both front and back faces. No cracks were observed for the 4th and 5th areal density samples. Figure 6.6 depicts the front and back faces of first four areal

Figure 6.2: Post mortem images of HRC 39.5 samples from the 1st to 5th areal density respectively (front faces)

Figure 6.3: Sample image for 4th and 5th areal density targets (back face) in which the projectile was struck in the target and shuttered after impact

Figure 6.4: Post mortem images of the front faces of HRC 49.5 samples from the 1st to 5th areal density respectively

Figure 6.5: Post mortem images of the back faces of HRC 49.5 samples from the 1st to 5th areal density respectively

density targets.

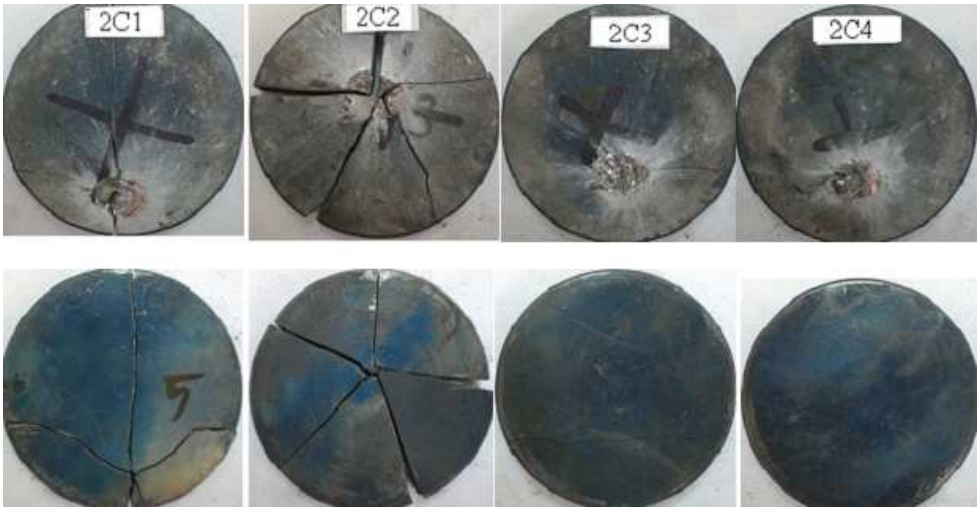

Figure 6.6: Post mortem images of front and back faces of HRC 52.5 samples from the 1st to 4th areal density respectively

The samples of HRC 58.5 provided ballistic protection from the 3rd areal density onwards. The samples of first two areal density were shuttered into several pieces and failed to provide protection. The samples which offer ballistic protection possessed no cracks on both front and back faces. Figure 6.7 illustrates images of samples of the last four areal density. The samples of the first areal density were completely shuttered and it was not possible to take image.

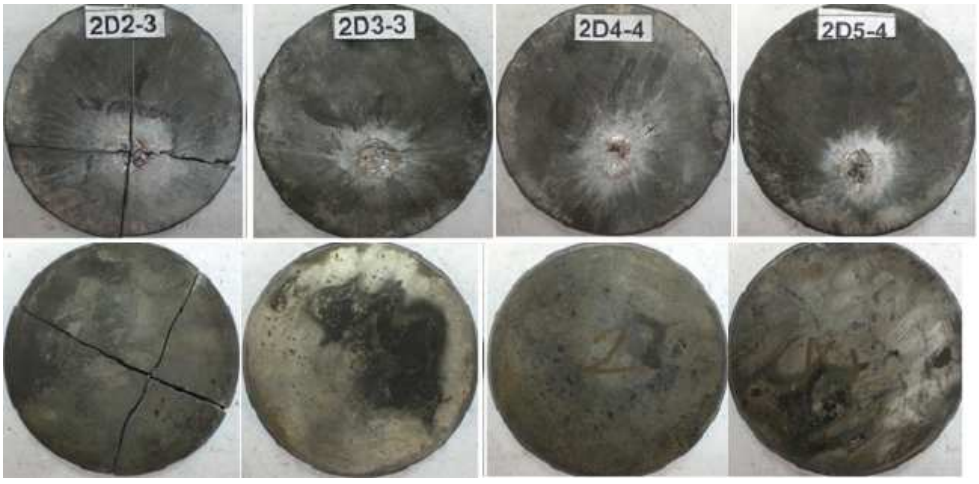

Figure 6.7: Post mortem images of front and back faces of HRC 58.5 samples from the 2nd to 5th areal density respectively

Recorded residual velocities of the projectiles are given in Figure 6.8.

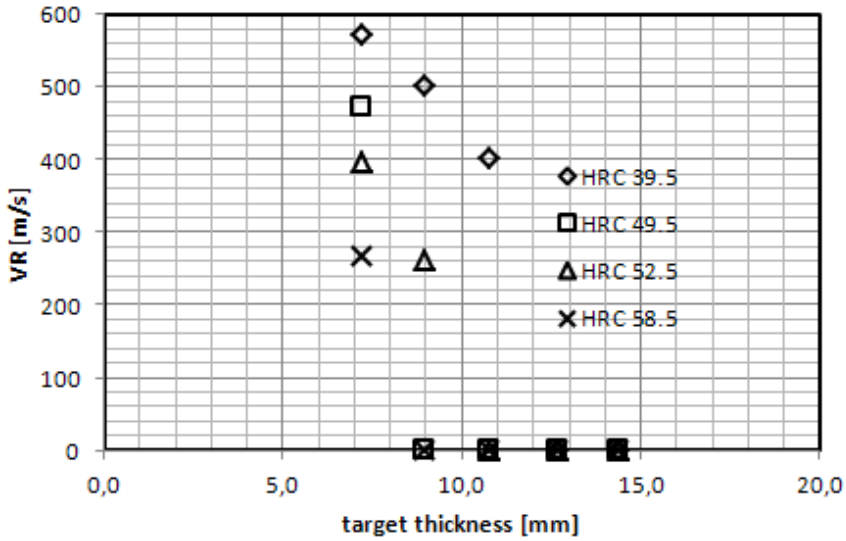

Figure 6.8: Recorded residual velocities of projectiles for each hardness

6.3 Comparison of Numerical, Analytical and Experimental Results

The 2-D and 3-D numerical analysis results were compared with the analytical calculations in Table 6.1. It is seen that there is a discrepancy between the numerical results and the analytical findings. It is evaluated that the analytical models underestimate the ballistic protection provided. Moreover there is a relative difference of 10 % between 2-D and 3-D numerical simulation results. That difference was attributed to the axis-symmetric assumption in 2-D simulations. However 2-D simulations possessed some advantages in being robust and considerable savings in runtime.

In Table 6.1, only Thompson model and THOR equation results were compared because of the fact that only these two models and the Wijk's model enabled the calculation of residual velocities. Wijk's model was found to give high results and thus it was not included into the table.

Table 6.1: Comparison of numerical and analytical results in terms of residual velocity [m/s]

t [mm]	HRC 39.5			HRC 49.5			HRC 52.5			HRC 58.5			THOR
	T.M.	N.A. (2D)	N.A. (3D)	T.M.	N.A. (2D)	N.A. (3D)	T.M.	N.A. (2D)	N.A. (3D)	T.M.	N.A. (2D)	N.A. (3D)	
7	730	611	555	707	544	471	698	535	446	677	488	391	450
8	722	575	513	695	506	401	685	479	363	660	418	286	408
9	715	537	471	684	453	344	672	418	275	643	339	133	367
10	707	494	414	672	389	243	659	341	105	626	211	0	326
11	699	451	341	660	314	84	645	242	0	609	0	0	286
12	691	397	253	648	199	0	631	0	0	590	0	0	246
13	683	334	153	636	0	0	617	0	0	572	0	0	207
14	674	252	0	623	0	0	603	0	0	552	0	0	168
t : thickness, T.M. : Thompson's Model, N.A. : Numerical Analysis													

Numerical results were also compared with the test results (Table 6.2). It is seen that the results are quite in agreement with regard to residual velocity. For HRC 39.5, the difference for the 4th areal density is evaluated as acceptable because only 3 of the 5 samples were not penetrated. For the hardness of HRC 49.5, as far as the residual velocities are concerned the results of the numerical analysis and the test agreed very well for the first areal density corresponding to a target thickness of 7.2 mm. However, for the $2^n d$ and $3^r d$ areal densities, although the test specimens offered ballistic protection, the numerical analysis reveal that th perforation takes place. For the case of HRC 52.5, full agreement was seen. Lastly, in the case of HRC 58.5, ballistic limit thickness was calculated as 10 mm, with a 1 mm difference from the test case.

Table 6.2: Comparison of experimental and 3D numerical results in terms of residual velocity [m/s]

t	HRC 39.5		HRC 49.5		HRC 52.5		HRC 58.5	
[mm]	Test	N.A.	Test	N.A.	Test	N.A.	Test	N.A.
7.2	570	555	470	471	395	446	265	391
9.0	500	471	0	344	260	275	0	133
10.8	400	341	0	84	0	0	0	0
12.7	0	153	0	0	0	0	0	0
14.4	0	0	0	0	0	0	0	0

Ballistic limit calculations for both of the numerical analysis, test results and analytical calculations were compared in Table 6.3.

Table 6.3: Comparison of ballistic limit results of numerical analysis, test and analytical calculations (dimensions in mm)

Hardness	Test	Numerical	THOR	Woodward	Thompson	Pol	Übeyli&Demir
HRC 39.5	12.1	14	18.5	27.5	25.4	9.3	12.8
HRC 49.5	9	12	18.5	25.4	23.8	7.6	12.1
HRC 52.5	10.8	11	18.5	23.5	22.3	7.1	11.6
HRC 58.5	10.8	10	18.5	21.3	20.4	6.3	11.2

From Table 6.3, it is seen that Übeyli&Demir model best matches the test results as it takes into account several facts as impact toughness. The other analytical models (except Pol's model) predicted higher ballistic limits. Calculations with the Pol's model revealed lesser amounts. It was attributed to the fact that this model was constructed for relatively thinner

plates. Numerical analysis were overall in 90 % agreement (approximately 1 mm error) with the test results. It was evaluated that where the numerical simulations revealed 150 m/s residual velocity, the test specimens possessed 50 % protection.

CHAPTER 7

DISCUSSION AND CONCLUSION

7.1 Discussion

The aim of this thesis was to investigate and evaluate the ballistic performance of hardened steel plates as a function of target hardness. ANSYS Autodyn was used as the numerical analysis tool and J-C strength model parameters for the targets were constructed by using the open literature.

It was evaluated that both the 2D and 3D numerical analysis gave plausible results in terms of projectile residual velocities. 10 % relative difference between the 2-D and 3-D simulations was attributed to the assumption of no deformations in the third dimension for the 2-D axis-symmetric case. In Chapter 6, residual velocity results of the 3-D numerical simulations were compared to test results and a good agreement was observed. For the target thicknesses which are 1 or 2 mm lower than the ballistic limit thickness, it was evaluated that the relative error between the residual velocities were generally lower than 10 %, when compared with the test results. It must also be noted that the selected mesh size was 0.4 mm for the 3D simulations, for which, 0.3 mm would be the optimal choice without taking into account the run times. Therefore it can be deduced that this discrepancy would be lower if lower element sizes were used. These good results were attributed to the J-C strength model which is very appropriate for the phenomena at these strain rates of $1000s^{-1}$. Moreover, the model parameters were constructed with regard to actual test results, which evaluate the dynamic behavior of tempered AISI 4340 at high strain rates taking into account the sensitivity to strain and strain rate hardening. No adjustment was made for temperature softening.

It was further evaluated that using a rigid projectile model instead of 100Cr6 model predicted

closer results to the test case. This approach was further supported by the experimental investigation of post shot projectile cores, which showed no evidence of plastic strain. The investigated cores were kept their shapes or shuttered. This kind of brittle behavior would not be supported by a simple model as J-C strength model.

When the post mortem images of the test samples and the numerical simulation results were compared, it was seen that the numerical analysis could not catch the brittle fragmentation behavior of test samples. It was evaluated that, the numerical modeling of this phenomena would be quite difficult and complicated failure models must be used which are constructed by advanced dynamic material tests. It was observed that constant plastic strain failure and J-C failure models could not predict such cracks.

Most of the analytical models under predicted the ballistic protection offered by the plates. This discrepancy was attributed to the fact that those models are highly generalized models and they do not take into account the strain and strain rate hardening properties for tempered target plates.

7.2 Conclusion

To conclude, it was obtained that the ballistic protection performance offered by the AISI 4340 steel plates increases with the increasing hardness. It was seen that shuttering of the target plates becomes an issue for high hardnesses due to adiabatic shear instabilities.

The suggested numerical simulation methodology and materal models were proved to be efficient in modelling the impact response of AISI 4340 plates for the studied hardness range in terms of projectile residual velocities and ballistic limit thicknesses.

7.3 Future Directions

Future directions regarding this study can be itemized as follows:

- Advanced failure models taking into account dynamic phenomena such as adiabatic shear bands fracture toughness can be designed and calibrated for the hardened steel plates to observe the global response of plates such as crack formation.

- Other alternative is that numerical modeling strategies such as the split element method (not available in AUTODYN) can be assessed with conjunction to a failure model to catch the crack formation in target plates.

- Other material modeling strategies (strength and failure model) must be considered for the projectile core. It was seen that J-C strength model could not represent the dynamic behavior of the projectile.

- Shuttering conditions for the projectile can be investigated. It was evaluated that using perforated targets instead of continuous targets would offer better results in terms of areal density because of the increased edge effects for the projectile.

- The impact of obliquity on ballistic performance of hardened steel plates can be investigated.

- Assessment of ballistic performance of dual hardness plates can be performed. It was evaluated that shuttering would be the limiting case for the high hardness plates.

- The effects of edge impact on the ballistic performance of steel plates can be assessed numerically be performing simulations with targets of varying diameters.

REFERENCES

[1] Moss G.M., Leeming D.W., and Farrar C.L. *Military Ballistics A Basic manual*. Brassey's Land Warfare, 1995.

[2] Hazell P.J. *Ceramic Armour: Design and Defeat Mechanisms*. Argos Press, 2006.

[3] Borvik T., Dey S., and Clausen A.H. Perforation resistance of five different high-strength steel plates subjected to small-arms projectiles. *International Journal of Impact Engineering*, 36:948–964, 2009.

[4] Gooch W.A. An overview of ceramic armor applications. *Ceramic Transections*, 134:3–21, 2002.

[5] *Fundamentals of Shaped Charges*. Wiley, New York, 1989.

[6] Held M. Schutzeinrichtung gegen geschosse. Deutsche Patentschrift 2 008 156, 21.02.1970.

[7] DaimlerChrysler Aerospace. Era and other reactive armours. Cranfield University Lecture Notes, April 2007.

[8] Held M. Armour. In *Proceedings of the 14thInternational Symposium on Ballistics*, Quebec, Canada, 26-29 September 1993.

[9] DEF STAN 95-24/3. Defence Procurement Agency, Directorate of Standardization, Kentigern House, 65 Brown Street, Glasgow, G2 8EX, UK., 23 January 2004.

[10] Ogorkiewicz R.M. *Advances in armour materials*, volume 4. International Defence Review, 1991.

[11] Chocron S., Anderson Jr. C.E., Grosch D.J., and Popelar C.H. Impact of the 7.62 mm apm2 projectile against the edge of a metallic target. *International Journal of Impact Engineering*, 25:423–437, 2001.

[12] Rosenberg Z., Ascuach Y., Yeshurun Y., and Dekel E. On the main mechanisms for defeating ap projectiles, long rods and shaped charge jets. *International Journal of Impact Engineering*, 36:588–596, 2009.

[13] Roberson C. Ceramic materials for lightweight armour applications. In *Proceedings of the Combat Vehicle Survivability Symposium*, Cranfield University, RMCS, Shrivenham, UK, 8-10 December 2004.

[14] Edwards M. Land-based military applications. *Comprehensive Composite Materials*, 6:681–699, 2000.

[15] Mil-c-60617a. Military Specification, Cartridge, 7.62 mm: NATO, Armor Piercing, M61, 1991.

[16] Zukas J.A., editor. *High Velocity Impact Dynamics*. John Wiley & Sons, Inc, 1990.

[17] Frechard S., Lichlenberger A., Rondot F., Faderl N., Redjaimia, and Adoum M. A new constitutive model for nitrogen austenitic stainless steel. In *Proceedings of the 4th European LS-Dyna Users Conference*, May 2003.

[18] Zukas J.A. *Introduction to Hydrocodes*. Elsevier, 2004.

[19] Smith P.D. and Hetherington J.G. *Blast and Ballistic Loading of Structures*. Butterworth-Heinemann Ltd, 1994.

[20] Joint technical coordinating group technical report. Technical report, Air Force Flight Dynamics Laboratory, 1976.

[21] Zukas J.A., Nicholas T., Swift H.F., Greszczuk L.B., and Curran D.R. *Impact Dynamics*. John Wiley & Sons, Inc., 1982.

[22] Segwick R.T. Theoretical terminal ballistic investigation and studies of impact at low and very high velocities. Technical Report AFATL-TR-68-61, Air Force Armament Laboratory, May 1968.

[23] Moss G.L. Technical Report ARBRL-TR-02242, Ballistic Research Laboratory, 1980.

[24] Backman M.E. Terminal Ballistics, Naval Weapons Center Technical Publication 5780, China Lake, California, February 1976.

[25] Recht R.F. Catastrophic thermoplastic shear. *Journal of Applied Mechanics*, 31:189, 1964.

[26] Zener C. The micro-mechanisms of fracture. *Fracturing of Metals, ASM*, pages 3–31, 1948.

[27] Meyers M.A. *Dynamic Behavior of Materials*. John Wiley & Sons, Inc.

[28] Deniz T., Kılıç N., and Yıldırım R.O. Balistik delme benzetimlerinde johnson-cook malzeme modeli sabitlerinin etkisinin incelenmes. In *Savtek 2010 Bildirileri*, 2010.

[29] Marchand A. and Duffy J. An experimental study of the formation process of adiabatic shear bands in a structural steel. *Journal of the Mechanics and Physics of Solids*, 36:251–283, 1988.

[30] Raftenberg M.N. A shear banding model for penetration calculations. *International Journal of Impact Engineering*, 25:123–146, 2001.

[31] Daridon L., Oussouaddi O., and Ahzi S. Influence of the material constitutive models on the adiabatic shear band spacing: Mts, power law and johnson-cook models. *International Journal of Solids and Structures*, 41:3109–3124, 2004.

[32] Lindholm U.S. and Johnson G.R. Strain rate effects in metals at large shear strains. In *Proceedings of the 29th Sagamore Army Materials Conference entitled Material Behavior Under High Stress and Ultrahigh Loading Rates*, New York, 1982.

[33] Dikshit S.N., Kutumbarao V.V., and Sundararajan G. The influence of plate hardness on the ballistic penetration of thick steel plates. *International Journal of Impact Engineering*, 16(2):293–320, 1995.

[34] Wingrove A.L. and Wulf G.L. Some aspects of target and projectile properties on penetration behaviour. *Journal of the Australian Institute of Metals*, 18:167–173, 1973.

[35] Manganello J. and Abbott K.H. Metallurgical factors affecting the ballistic behaviour of steel targets. *Journal of Materials, JMLSA*, 7:231–239, 1972.

[36] Dikshit S.N. and Sundararajan G. The penetration of thick steel plates by ogive shaped projectiles - experiment and analysis. *International Journal of Impact Engineering*, 12:373–408, 1992.

[37] An experimental and analytical study on the penetration of rods into ceramic faced armours. den reijer p.c. Technical report, TNO Defence Research, 1993.

[38] Viechnicki D. Armor ceramics. In *Proceedings of the Third TACOM Armor Coordinating Conference*, Monterey, California, 17-19 February 1987.

[39] Rosenberg Z. and Tsaliah J. Applying tate's model for the interaction of long rod projectiles with ceramic targets. *International Journal of Impact Engineering*, 9(2):247–251, 1990.

[40] Jones T.L.J., DeLorme R.D., Burkins M.S., and Gooch W.A. Ballistic evaluation of magnesium alloy az31b. Technical Report ARL-TR-4077, Army Research Laboratory, April 2007.

[41] Borvik T., Langseth M., Hopperstad O.S., and Malo K.A. Ballistic penetration of steel plates. *International Journal of Impact Engineering*, 22:855–886, 1999.

[42] Pickup I.M., Barker A.K., James B.J., Cottenot C., and Orsini H. The effects of stress pulse characteristics on the defeat of armour piercing projectiles. In *Proceedings of the 19th International Symposium on Ballistics*, 7-11 May 2001.

[43] Schwer L.E. Preliminary assessment of non-lagrangian methods for penetration simulation. In *8th International LS-DYNA User Conference*, Detroit, 2004.

[44] Vahedi K. and Khazraiyan N. Numerical modelling of ballistic penetration of long rods into ceramic/metal armors. In *8th International LS-DYNA Users Conference*, Detroit, 2004.

[45] Vignjevic R., Lepage S., and Vuyst T.D. Simulation of high velocity impacts on thin metallic target i (element erosion). *Impact Loading of Lightweight Structures*, 49, 2005.

[46] Vignjevic R., Lepage S., and Vuyst T.D. Simulation of high velocity impacts on thin metallic target ii (discrete elements). *Impact Loading of Lightweight Structures*, 49, 2005.

[47] Vignjevic R., Lepage S., and Vuyst T.D. Simulation of high velocity impacts on thin metallic target ii (sph). *Impact Loading of Lightweight Structures*, 49, 2005.

[48] Vignjevic R., Campbell J., and Lapage S. Numerical simulation of high velocity impacts on thin metallic targets i. In *Dynamics and Control of Systems and Structures in Space (DCSSS) 6th Conference*, Riomaggiore, Italy, June 2004.

[49] Vignjevic R., Campbell J., and Lapage S. Numerical simulation of high velocity impacts on thin metallic targets ii. In *Dynamics and Control of Systems and Structures in Space (DCSSS) 6th Conference*, Riomaggiore, Italy, June 2004.

[50] Banerjee B., Guilkey J.E., Harman T.B., Schmidt J.A., and McMurtry P.A. Simulation of impact and fracture with the material point method. In *11th International Conference on Fracture*, Turin (Italy), March 20-25 2005.

[51] Resnyansky A.D. Dyna-modelling of the high-velocity impact problems with a split-element algorithm. *International Journal of Impact Engineering*, 27:709–727, 2002.

[52] Park M., Yoo J., and Chung D.T. An optimization of a multi-layered plate under ballistic impact. *International Journal of Solids and Structures*, 42:123–137, 2005.

[53] Teng X. and Wierzbicki T. Evaluation of six fracture models in high velocity perforation. *Engineering Fracture Mechanics*, 2006.

[54] Borvik T., Hopperstad O.S., Berstad T., and Langseth M. Numerical simulation of plugging failure in ballistic penetration. *International Journal of Solids and Structures*, 38:6241–6264, 2001.

[55] Dey S., Borvik T., Hopperstad O.S., and Langseth M. On the influence of constitutive relation in projectile impact of steel plates. *International Journal of Impact Engineering*, 34:464–486, 2007.

[56] Dey S., Borvik T., Hopperstad O.S., and Langseth M. On the influence of fracture criterion in projectile impact of steel plates. *Computational Materials Science*, 38:176–191, 2006.

[57] Hopperstad O.S., Borvik T., Langseth M., Labibes K., and Albertini C. On the influence of stress triaxiality and strain rate on the behaviour of a structural steel. part i. experiments. *European Journal of Mechanics A/Solids*, 22:1–13, 2003.

[58] Borvik T., Hopperstad O.S., and Berstad T. On the influence of stress triaxiality and strain rate on the behaviour of a structural steel. part ii. numerical study. *European Journal of Mechanics A/Solids*, 22:15–22, 2003.

[59] Lenselink H. Oblique penetration in ductile plates. In *MSC 1991 World Users' Conference Proceedings*.

[60] Kaufmann C. and Williams K. Optimization of a numerical simulation involving the impact of an ap-t c44 12.7mm projectile on a semi-infinite monolithic 6061-t6 aluminium target. Technical report, Defence Research and Development Canada, 2004.

[61] Borvik T., Hopperstad O.S., Berstad T., and Langseth M. Perforation of 12mm thick steel plates by 20mm diameter projectiles with flat, hemispherical and conical noses part ii: numerical simulations. *International Journal of Impact Engineering*, pages 37–64, 2002.

[62] Schwer L.E., Hacker K., and Poe K. Perforation of metal plates: laboratory experiments and numerical simulations. In *9th International LS-DYNA Users Conference*, Detroit, 2006.

[63] Wisnievski A. and Tomaszewski L. Computer simulation of ap projectile penetration into rha. *Techniczne Wyroby Wlokiennicze*, pages 32–39, 2009.

[64] Nsiampa N., Dyckmans G., and Chabotier A. Impact of 7.62 mm ap ammunition into aluminium 5083 plates. In *Proceedings of the 23rd International Symposium on Ballistics*, Tarragona, Spain, 16-20 April 2007.

[65] Corbett G.G. Impact loading of plates and shells by free-flying projectiles: a review. *International Journal of Impact Engineering*, 18(2):141–230, 1996.

[66] Woodward R.L. A rational basis for the selection of armour materials. *The Journal of Australian Institute of Metals*, 22:167–170, 1977.

[67] Gupta N.K. and Madhu V. An experimental study of normal and oblique impact of hard-core projectile on single and layered plates. *International Journal of Impact Engineering*, 19(5-6):395–414, 1997.

[68] Gupta N.K. and Madhu V. Normal and oblique impact of a kinetic energy projectile on mild steel plates. *International Journal of Impact Engineering*, 12(3):333–343, 1992.

[69] The resistance of various metallic materials to perforation by steel fragments; emprical relationships for fragment residual velocity and residual weight. Project Thor TR No. 47, April 1961.

[70] The resistance of variousnon- metallic materials to perforation by steel fragments; emprical relationships for fragment residual velocity and residual weight. Project Thor TR No. 51, April 1963.

[71] Recht R.F. and Ipson T.W. Ballistic perforation dynamics. *Journal of Applied Mechanics Transections, ASME*, 30:385–391, 1963.

[72] Lambert J.P and Jonas G.H. Towards standardization of in terminal ballistic testing: velocity representation. Technical Report BRL-R-1852, Ballistic Research Laboratory, Aberdeen, MD, 1976.

[73] Lambert J.P. A residual velocity predictive model for long rod peentrators. Technical Report ARBRL-MR-02828, Ballistic Research Laboratory, Aberdeen, MD., 1978.

[74] Stone G.W. Projectile penetration into representative targets. Technical Report SAND94-1490, Sandia National Laboratories, 1994.

[75] Wijk G., Hartman M., and Tryberg A. A model for rigid projectile penetration and perforation of hard steel and metallic targets. Technical Report FOI-R–1617-SE, FOI - Swedish Defence Research agency, April 2005.

[76] Thompson W.T. An approximate theory of armour penetration. *International Journal of Applied Physics*, 26(1):80–82, 1995.

[77] Demir T. Metal ve katmanlı zırh malzemelerinin 7,62 mm'lik zırh delici mermiler karşısında balistik başarımlarının incelenmesi. Master's thesis, TOBB Ekonomi ve Teknoloji Üniversitesi, August 2008.

[78] Pol M.H., Bidi A., and Hoseini A.V. Liaghat G.H. Analysis of normal penetration of ogive-nose projectiles into thin metallic plates. *World Academy of Science, Engineering and Technology*, 2009.

[79] Century Dynamics Inc., San Ramon, California. *Autodyn Theory Manual*, 1998.

[80] Hayhurst C.J., Clegg R.A., Livingstone I.H., and Francis N.J. The application of sph techniques in autodyn-2d^{TM}to ballistic impact problems. In *Proceedings of the 16th International Symposium on Ballistics*, San Francisco, CA, 23-28 September 1996.

[81] Johnson G.R. and Cook W.H. A constitutive model and data for metals subjected to large strains, high strain rates and high temperatures. In *Proceedings of the 7th International Symposium on Ballistics*, April 1983.

[82] Johnson G.R. and Cook W.H. Fracture characteristics of three metals subjected to various strains, strain rates and temperatures. *Engineering Fracture Mechanics*, 21:31–48, 1985.

[83] Westerling L. A note on an erosion criterion in autodyn. Technical report, FOI, 2002.

[84] Bilici M.A. *An investigation on the ballistic behaviour of alumina/aluminium armor structures*. PhD thesis, METU, 2007.

[85] Saltelli A., Tarantola S., Campolongo F., and Ratto M. *Sensitivity analysis in practice. A guide to assessing scientific models*. John-Wiley, Chichester, 2004.

[86] Steinberg D.J. Equation of state and strength properties of selected materials. Technical report, Lawrence Livermore National Laboratory, 1996.

[87] Banerjee B. The mechanical threshold stress model for various tempers of aisi 4340 steel. *International Journal of Solids and Structures*, 44:834–859, 2007.

[88] Lee W-S and Su T-T. Mechanical properties and microstructural features of aisi 4340 high-strength alloy steel under quenched and tempered conditions. *Journal of Materials Processing Technology*, 87:198–206, 1999.

[89] Tanimura S. and Duffy J. Strain rate effects and temperature history effects for three different tempers of 4340 var steel. Technical report, Army Research Office, 1984.

[90] Lee K.E. Analysis of multi-layered materials under high velocity impact using cth. Master's thesis, Air Force Institute of Technology, 2008.